Le design de (nano)composites céramiques dérivés de polymères comme catalyseurs

Roberta Morais Ferreira

Ph.D. Thesis

Université de Limoges

University of Limoges

ED 653 - Sciences et Ingénierie

Institut de Recherche sur les Céramiques (IRCER) - UMR CNRS 7315

A thesis submitted to the University of Limoges in partial fulfillment of the requirements of the degree of Doctor of Philosophy
Matériaux céramiques et traitements de surface

Presented and defended by
Roberta K. MORAIS FERREIRA
On December 5, 2022

DESIGN OF POLYMER-DERIVED CERAMIC (NANO)COMPOSITES AS CATALYSTS

Advisors: **Ricardo MACHADO et Samuel BERNARD**

JURY:
Examiners:
M Assil BOUZID, Charge de recherche CNRS, IRCER Limoges
M Günter MOTZ, Professeur des université, Université de Bayreuth
M Luiz Antonio COELHO, Universidade Estadual de Santa Catarina
M Luiz Fernando RIBEIRO, Professeur des université, Universidade Federal de Santa Catarina
M Ricardo MACHADO, Professeur des université, Universidade Federal de Santa Catarina
M Samuel BERNARD, Directeur de recherche CNRS, IRCER Limoges

Roberta Karoline Morais Ferreira

Design of polymer-derived ceramic (nano)composites as catalysts

Joint Supervision thesis presented to the Graduate Program in Chemical Engineering of the Federal University of Santa Catarina (UFSC) and Materials Science of Limoges University (UL) as a requirement to obtain the PhD title.

Advisors:
Ricardo Antonio Francisco Machado, Dr. (UFSC)
Samuel Bernard, Dr. (UL)

Florianópolis/Limoges

2022

Roberta Karoline Morais Ferreira

Design of polymer-derived ceramic (nano)composites as catalysts

Tese submetida ao Programa de Pós-Graduação em Engenharia Química da Universidade
Federal de Santa Catarina e Ciências de Materiais da Instituição Université de Limoges em regime de cotutela para a obtenção do título de Doutora em Engenharia Química e Ciência de Materiais.

Advisors:
Ricardo Antonio Francisco Machado, Dr. (UFSC)
Samuel Bernard, Dr. (UL)

Florianópolis/Limoges

2022

Ficha de identificação da obra elaborada pelo autor,
através do Programa de Geração Automática da Biblioteca Universitária da UFSC.

Morais Ferreira, Roberta Karoline
DESIGN OF POLYMER-DERIVED CERAMIC (NANO)COMPOSITES AS CATALYSTS / Roberta Karoline Morais Ferreira ; orientador, Ricardo Francisco Antonio Machado, coorientador, Samuel Bernard, 2022.
125 p.

Tese (doutorado) - Universidade Federal de Santa Catarina, Centro Tecnológico, Programa de Pós-Graduação em Engenharia Química, Florianópolis, 2022.

Inclui referências.

1. Engenharia Química. I. Antonio Machado, Ricardo Francisco . II. Bernard, Samuel . III. Universidade Federal de Santa Catarina. Programa de Pós-Graduação em Engenharia Química. IV. Título.

Roberta Karolie Morais Ferreira

Design of polymer-derived ceramic (nano)composites as catalysts

O presente trabalho em nível de doutorado foi avaliado e aprovado por banca examinadora composta pelos seguintes membros:

Dr. Assil Bouzid

Centre Nationel de la Recherche Scientifique

Prof. Günter MOTZ, Dr.

Universidade de Bayreuth

Prof. Luiz Antonio COELHO, Dr.

Universidade Estadual de Santa Catarina

Prof. Luiz Fernando RIBEIRO, Dr.

Universidade Federal de Santa Catarina

Certificamos que esta é a versão original e final do trabalho de conclusão que foi julgado adequado para obtenção do título de doutora em Engenharia Química.

ICP-Edu
Documento assinado digitalmente
Debora de Oliveira
Data: 05/03/2023 16:52:07-0300
CPF: ***.453.929-**
Verifique as assinaturas em https://v.ufsc.br

Profª. Débora de Oliveira, Dra.

Coordenadora do Programa

ICP-Edu
Documento assinado digitalmente
Ricardo Antonio Francisco Machado
Data: 05/03/2023 17:50:33-0300
CPF: ***.377.139-**
Verifique as assinaturas em https://v.ufsc.br

Prof. Ricardo Antonio Francisco Machado, Dr.

Orientador

Florianópolis, 05 de Dezembro de 2022

To my beloved parents for their unconditional love.

“The strain of anti-intellectualism has been a constant thread winding its way through our political and cultural life, nurtured by the false notion that democracy means that 'my ignorance is just as good as your knowledge.”

— Isaac Asimov

ABSTRACT

The chemical modification of a poly (vinylmethyl-co-methyl) silazane with transition metal acetates, acetylacetonates and chlorides complexes was performed by the polymer-derived ceramic (PDC) route, followed by pyrolysis at different temperatures under the same atmosphere for an in-depth investigation of ceramic formation. The obtained materials were characterized by thermal stability, elemental/phase composition evolution, and crystallization behavior. Results show that the Si:Metal molar ratio as well as thermal treatment conditions have a strong influence on the final material structure. SiCN ceramics displaying various metal contents were obtained regardless of the metal precursor chosen. This work highlights the low-temperature *in situ* formation of nickel nanocrystallites embedded within an amorphous SiCN(O) ceramic matrix through careful control of the chemistry behind materials design. Pyrolysis of Ni-modified preceramic polymer obtained in a Si:Metal molar ratio of 2.5, at 500 °C under argon atmosphere revealed a homogeneous dispersion of nickel nanocrystallites in the SiCN(O) matrix. Such newly synthesized material performed outstanding electrocatalytic performances for oxygen reduction in alkaline water electrolysis. This innovative pre-catalyst proved to be a promising candidate for future renewable energy technologies.

Keywords: Hydrogen. Polymer-Derived Ceramics. Alkaline water splitting.

RÉSUME

La modification chimique d'un poly (vinylmethyl-co-methyl) silazane avec des complexes d'acétates, d'acetylacetonates ou de chlorures de métaux de transition a été réalisée via la voie céramique dérivée de polymère (PDC). Celle ci a été suivie d'une pyrolyse à différentes températures sous la même atmosphère, de manière à approfondir l'étude de la formation de la céramique. Le matériau obtenu a été caractérisé en termes de stabilité thermique, de composition élémentaire pour chaque phase, et de cristallinité. Les résultats montrent que le rapport molaire Si:métal ainsi que les conditions de traitement thermique ont une influence élevée sur la structure finale du matériau. Des céramiques SiCN présentant des teneurs en métal différentes ont été obtenues dans chaque cas, et ce quel que soit le précurseur métallique choisi. Ces travaux mettent en avant la formation *in situ* et à basse température de nanocrystallites de nickel intégrées dans une phase amorphe SiCN(O), grâce à un contrôle minutieux de la chimie derrière la conception des matériaux. Un composite de nanoparticules de Ni dispersées dans une matrice de SiCN(O) est obtenu par pyrolise, à 500°C sous argon, de polymères précéramiques chimiquement modifiés au Ni selon un rapport atomique Si/Ni de 2.5. Ce matériau innovant présente des propriétés performantes d'électrocatalyse pour la réduction d'oxygène en milieux alcalins. Ces mêmes propriétés en font un excellent candidat pour des applications dans le futur des énergies renouvelables.

Mots clés : Hydrogène. Céramiques dérivées de polymères. fractionnement de l'eau dans les milieux alcalins.

ACKNOWLEGMENTS

I wish to express my gratitude to those who participate and contributed to the development of this thesis. First of all, I would like to thank my advisors Dr. Ricardo Machado and Dr. Samuel Bernard for their guidance and the opportunity to learn during this interdisciplinary research involving Brazil and France. I sincerely thank the friends and co-workers Kinga, Raghvender, Maxime B., Maxime C, Nilesh, Rafael, Maíra, Nicolas C., and Melanie, for their company, help and the good moments shared during my stay in France.

I also wish to especially thank Eloise, Julie, Marina, Pamela, Pierre and Richard for all their prompt help to guarantee that this work would not be stopped during the pandemic. Furthermore, I would like to acknowledge the chemical engineering department of UFSC for their prompt help whenever it was needed and for all these years of growing and learning. Without their help, everything would be much more difficult.

I want to recognize in particular professors Cintia Marangoni and Ricardo for all their kindness and friendship during all these years. I would like to highlight how grateful I am for the support and expression of pure love my best friend Luiz Filipe gave me during the hardest months of this journey, as well as Analisse, Felipe, Geovanna and Jessyca who were always with me. Your company, support and understanding were indispensable in many moments. Lastly, and yet very important, I want to sincerely express my gratitude to my family. Without their love, support and faith in me, I would never be able to go so far.

List of Acronyms, Abbreviations and Symbols

AC	Alternating current
AEM	Anion exchange membranes
ATR	attenuated transmission reflectance – infrared
AWE	Alkaline water electrolysis
BET	Brunauer-emmett-teller
C_{DL}	Non-faradaic double layer capacitance
CO_2	Carbon dioxide
COP	Conference of parties
DC	Direct current
DMF	Dimethyl formamide
e^-	Electrons
E_{eq}	Equilibrium cell voltage
ECSA	Electrochemically active surface area
EDL	Electric double layer
EIS	Electrochemical impedance spectroscopy
E_{tn}	Thermoneutral voltage
F	Faraday constant
FTIR	Fourier-Transformed Infrared Spectroscopy
GHG	Greenhouse gases
GWP	Global warming potential
H^+	Hydrogen ion
H_2	Dihydrogen
H_2O	Water
HER	Hydrogen evolution reaction
HHV	Hiher heating value
ICP-OES	Elemental analysis & Inductively-Coupled Plasm – Optical Emission Spectroscopy
IHL	Inner Helmholtz layer
IPCC	Intergovernmental Panel on Climate Change
j	Current

KOH	Potassium hydroxide
MS	Mass spectrometry
NaOH	Sodium hidroxide
O_2	Oxygen
O^{2-}	Oxide ion
OER	Oxygen evolution reaction
OH^-	Hydroxyl ion
OHL	Outer Helmholtz layer
PDC	Polymer-derived ceramic
PGM	Platinum Group Metals-based structures
PEM	Proton exchange membrane
PPM	Parts per million
PSZ	Polysilazane
R	Electrical resistance
R_b	Resistance of bubbles
R_c	Resistance of circuits
R_d	Resistance of diaphragm
R_e	Resistance ofthe electrolyte
R_{Ohm}	Sum of Resistances existing in the cell
SOE	Solid Oxide Electrolysis
TGA-MS	Thermogravimetric analysis & mass spectrometry
XRD	X-Ray diffraction
ΔG	Gibbs free energy
ΔH	Entalphy variation
ΔS	Entropy variation
η	Overpotential

LIST OF FIGURES

LIST OF TABLES

CONTENTS

1. GENERAL INTRODUCTION

The greenhouse effect is a natural phenomenon referring to the increased heating of Earth's surface and is a vital component to sustain life. Yet, it causes environmental pollution due to fossil fuels' combustion, producing CO_2. Accompanied by human activities, it strongly affects the atmosphere's chemical composition. These phenomena together result in an excessive greenhouse effect which is responsible for the current climate change (Figure 1.1). Currently, fossil energies represent more than 80% of the world's energy consumption [1] and the global demand is steadily rising as a consequence of the developing economies. For that reason, the Intergovernmental Panel on Climate Change (IPCC, 2021) [8] demonstrated that an energy transition is paramount to stop using depleting resources and reduce climate impacts which are already expected to cause approximately 250.000 additional deaths per year between 2030 and 2050 [2].

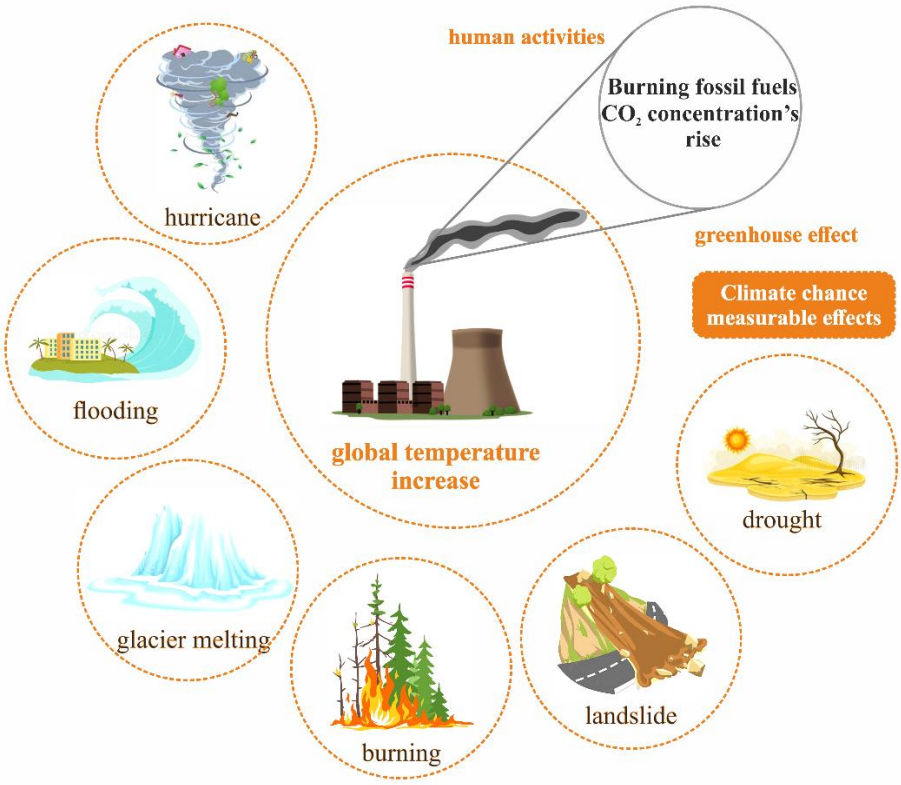

Figure 1.1. Energy demand effects on climate change.

Important climate directives have been taken over the past decades. Most of these measurements are based on innovation and technology development as essential approaches for

a global energy transition resulting in a steady decline of pollutant emissions since 2000, especially in Europe [3]. In particular, research & development in technologies exploiting renewable sources such as solar and wind power have been largely used as the first step toward a CO_2 and nuclear waste-free energy future. Nevertheless, their dependence on geographical position and their variability hamper the possibility of solving the climate challenges on their own. Indeed, a recent publication of the Organisation for Economic Cooperation and Development (OECD) has emphasized that with emissions on the rise again, governments must work seriously on shifting their economies to a low-carbon model and stop investing in carbon-intensive infrastructure to keep warming below 1.5°C [4]. This has been also prioritized by the Intergovernmental Panel on Climate Change [5] and more recently by the OECD Secretary-General who called for stronger action on climate change [6]. Intensive efforts are therefore required to align long-term energy system trends with 2060 decarbonization goals compatible with the 'well-below' 2°C objectives established in the Paris agreement [7]. Within this scenario, the period between 2020 and 2030 is regarded as crucial in the transition to a low-carbon economy.

A possible solution to circumvent this issue is the development of energy storage and conversion devices, as they can address the intermittent nature of the main renewable sources. One of the most promising strategies for that is the conversion of chemical energy into electrical energy via electrochemical conversion, which is the principle behind fuel cells and metal-air batteries. The inverse process of generating valuable chemical compounds (*e.g.*, fuels and raw materials for the industry) using electrolyzers is an appealing way to propel the hydrogen economy.

The so-called water splitting or water electrolysis is a promising pathway to achieve efficient hydrogen production concerning energy conversion and storage with catalysis or electrocatalysis playing a critical role. These materials are used to diminish the kinetic energy barriers of both Oxygen Evolution Reaction (OER) and Hydrogen Evolution Reaction (HER), producing O_2 and H_2 at the anode and cathode, respectively [8]. Up to now, noble-metal electrocatalysts are the most employed in such process, as they own paramount features such as high stability, electrical conductivity and resistances to oxidation and corrosion, low Tafel slope and overpotentials -which are indispensable for an effective water electrolysis process [9].

To achieve the objective of placing regenerative energy storage and conversion systems into a commercial reality, it is therefore of utmost importance to develop stable and efficient oxygen electrodes [10]. Rather than the current state-of-the-art noble-metal electrocatalysts, which are costly and scarce, and also tend to aggregate under working conditions causing activity degradation [11], 3d Transition Metal-based materials like **Ni** and **Co** [12], are regarded as inexpensive, earth-abundant and environmentally friendly materials employable to produce efficient and robust electrocatalysts for the water splitting process. In addition to that, such metals can display catalytic performances comparable to state-of-the-art noble metals counterparts, predominantly in alkaline media [13], hence, having the required features to be employed in such process, being promising candidates for anion exchange membrane electrolyzers and have therefore triggered a rush in the exploration of non-noble TM-based HER and OER electrocatalysts. Although great progress has been made in recent years, it is worth point out that **none of the current electrocatalysts fulfill activity and lifetime requirements for the application of anion exchange membrane electrolyzers**. Consequently, significant directions toward materials design must be taken to rank water electrolysis among the most efficient, environmentally friendly and decarbonized routes for dihydrogen generation.

Considering all these aspects, the present thesis has been built to create new knowledge in the field of functional materials for water oxidation. It targets a new family of **nanocomposites** prepared via the **Polymer-Derived Ceramics (PDCs)** route to design sustainable water-splitting electrodes. Thus, different Co and Ni precursors were investigated in this study for the modification of a polysilazane in DMF, as this preceramic precursor could be highly reactive towards this solvent in presence of a metal catalyst under an inert atmosphere (Ar). Furthermore, considering the simplicity, flexibility, and low cost of the PDC route employed for that purpose, this approach is expected to allow the production of active and stable high superficial surface area nanocomposites possessing accessible non-noble TM, hence, showing promising features for electrocatalysis applications.

After a literature review given in chapter 1, chapter 2 details the experimental part. Following, chapter 3 describes the parts dedicated to materials design and characterization along with the application of our materials for OER as a proof of concept. Although OER activity remains rather moderate in comparison with those reported in the literature, the achieved results

correspond to one of the best performances ever reported for materials containing only nickel as active phase, thus validating our approach and the prospects that will result from it.

2. LITERATURE REVIEW

2.1. Climate context & energy storage technology

Over the last decades, the effects and prospects of the ongoing climate change have modified global actions regarding the increasing energy demand. Since the industrial revolution, natural resources and energy have been used to support overall population growth, industrial activities and economic development, leading to a remarkable increase in greenhouse gas (GHG) emissions, especially CO_2 and NO_x [14].

Studies have demonstrated that energy generation and consumption have been responsible for about 70% of the total GHG emissions, of which, CO_2 represents 57% [15,16]. In the last decade, the average concentration of CO_2 in the atmosphere increased by more than 2 ppm each year due to anthropogenic action [17], exceeding 400 ppm in 2015, as demonstrated in Figure 2.1. This issue is mostly associated with the burning of fossil fuels [5] once it releases enormous quantities of CO_2, affecting the atmosphere's thermal balance absorbing more radiation and, hence, leading to global warming [19]. Such emissions are drastically affecting the global climate causing an augmented probability of extreme weather events like heatwaves, storms, and droughts [14].

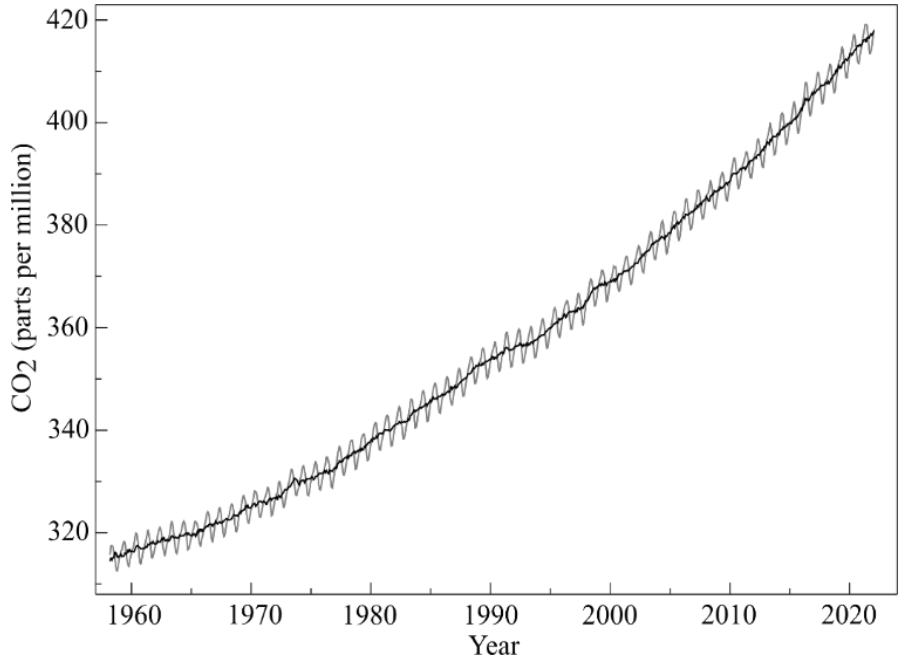

Figure 2.1. Atmospheric CO_2 concentration (ppm) per year, adapted from NOAA Global Monitoring Laboratory (2021).

As demonstrated by the Intergovernmental Panel on Climate Change (IPCC, 2021) [20], there is an urgency to act towards an energy transition to stop using depletable resources and reduce climate impacts on urban areas and natural habitats. Following demonstrations of scientific predictions, it was observed that doubling the atmospheric CO_2 concentration from 280 to 560 ppm would cause average global warming of 2 °C. Due to this, at the Conference of Parties (COP) 21 (Paris, 2015), countries committed to keeping the global temperature increase below 2 °C of pre-industrial levels [21–23]. Two years later, this value was decreased to 1.5 °C (COP 23, 2017), aiming to reach net-zero emissions until 2050 to limit global warming [24]. Nonetheless, a year later it has been detected that the global energy use was 173,340 TWh and still a mix mostly comprised of non-renewable sources, being more than 80% of it derived from fossil fuels [25].

Seeking to reach the Paris Agreement goals, the development of strategies with limited GHG emissions became crucial. For this reason, in the last decades, the first step toward the net-zero CO_2 emission energy future relied especially on the production of energy by renewable resources [26]. Solar energy and wind power were the most utilized, followed by widely consolidated sources like biopower, geothermal, and ocean power [27,28].

Solar energy is the foremost energy-generating technology due to advantages like its ability to directly convert sunlight to electricity, its minimal impacts on ecosystems, easy industrial- or local-scale applicability and abundance in the tropics and temperature regions of the planet [29,30]. On the other hand, it has an intermittent nature, and relatively low efficiency (mostly 10-20%), besides requiring great areas of land for a large-scale installation [21,31]. Yet, it is one of the less expensive electricity generation energy sources.

Regarding wind power, it has significant potential of avoiding the use of considerable amounts of Earth's fossil fuels, however, cost-efficient wind turbines depend on rare-earth elements such as neodymium and praseodymium as the permanent-magnet synchronous generator for power conversion. These elements are limited and, consequently, can easily entail a demand outpacing the supply. Moreover, only a fraction of wind passing through the turbine is converted into electrical energy due to losses in the system [32].

Even though these renewable energy sources are sustainable alternatives to conventional fossil fuels, their availability varies depending on weather, climate, geographical location and time of the day [27,33]. This variability creates periods of supply higher than demand, enabling the use of excess energy in other processes to obtain clean energy. To this end, hydrogen (H_2) appears as an outstanding energy carrier. Regardless of its explosive nature, H_2 is non-toxic, non-polluting, renewable and relatively abundant in nature as it is a constituent of water molecules. In addition, H_2 has a gravimetric energy density three times higher than that of liquid hydrocarbon-based fuels. Thereby, it can store more energy per unit weight or volume [34]. This energy carrier is largely used in industrial processes such as refining petroleum, ammonia production for fertilizers, annealing, heat-treating metals, coolant in power plant generators and aircraft [35,36].

Hydrogen can be generated by varied technologies employing either non-renewable sources such as coal, natural gas and oil or renewable sources like biomass, solar, water and wind power. Nevertheless, its production is still majorly based on non-renewable sources [37]. For instance, in 2015, it was reported that more than 44.5 million tons of industry-obtained hydrogen were produced by steam-methane reforming and coal gasification, corresponding to more than 95% of the total production [35]. Five years later (2020), its global use was stated to be of approximately 120 million tons, being 76% produced from natural gas and 23% from coal, resulting in low purity ("grey") hydrogen along with 830 million tons of CO_2 emission [38].

The color-based nomenclature is used to differentiate the manufacturing process, required feedstock and energy source, as well as the GHG emission correlated to the type of hydrogen generated. Accordingly, “grey”, “blue”, “turquoise” and “green” hydrogen, classify the conventional, low-CO_2, CO_2-free and carbon-free routes, respectively, as demonstrated in examples of each class shown in Figure 2.2.

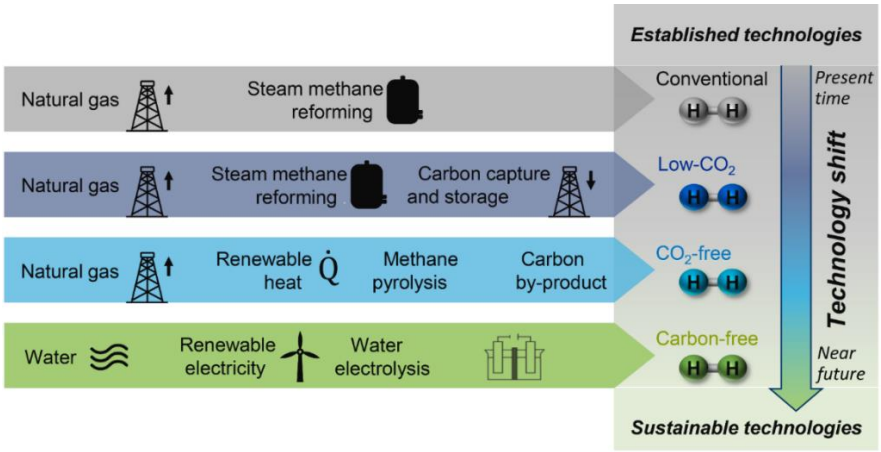

Figure 2.2. Hydrogen production pathways and product-associated colors [38].

Fundamentally, conventional or grey hydrogen is based on fossil resources and results in considerable emissions of CO_2. Low-CO_2 or blue hydrogen differs from the previous case solely by the fact that most of the CO_2 emitted is captured and stored. CO_2-free or turquoise hydrogen is obtained by processes that do not release CO_2, instead, carbon is the by-product. In this case, it can be generated, for example, through bond cleavage as happens in methane pyrolysis. Carbon-free or green hydrogen relies on renewable energy sources and does not generate CO_2 [38], being, therefore, the most promising technology for the net-zero emission goal.

Within the context of the described scenario, it is expected that the demand for green hydrogen will soar in the next years. As such, researches toward thoroughly sustainable hydrogen generation and net-zero CO_2 emissions by 2050 are ongoing [39]. Unlike non-renewable-based strategies, water electrolysis is an environmentally pleasant pathway for hydrogen production if driven by renewable sources-derived electricity [8,35,40]. This condition is grounded on the fact that this process requires an external power supply to promote oxidation and reduction reactions, causing an economically inefficient energy application that can only be overcome through the use of renewable sources to either decrease or end the need for external power supply [40].

2.2. Water electrolysis

Although industrially used only in small-scale production with a global supply of solely 4% [41], water electrolysis is classified as a feasible way of producing H_2 on large scale [42] and is also regarded as one of the long-term market hydrogen generations for the next years [37].

Electrolysis has numerous benefits since it absorbs a greater amount of energy per unit of H_2 produced in comparison to hydrocarbon-based H_2 production [42]. According to Baykara (2018), it has a low Global Warming Potential (GWP) of less than 5 kg CO_{2eq}/kg H_2 against 30 CO_{2eq}/kg H_2 when grid electricity is employed. Thereby, the excess electricity generated, for example, from solar energy or wind power, can be stored in the form of chemical bonds by electrochemically splitting water, forming hydrogen and oxygen gases. Their subsequent recombination is a clean way of providing electrical energy once it releases only water during energy conversion [43], as illustrated in Figure 2.3.

This approach is interesting for remote areas with abundant solar or wind electricity resources, not only to produce hydrogen but also to meet energy needs for households, powering telecommunication stations and small-scale light manufacturing industry applications [44]. Additionally, it is an alternative for highly pure H_2 large-scale generation in a short time with less environmental impact [45].

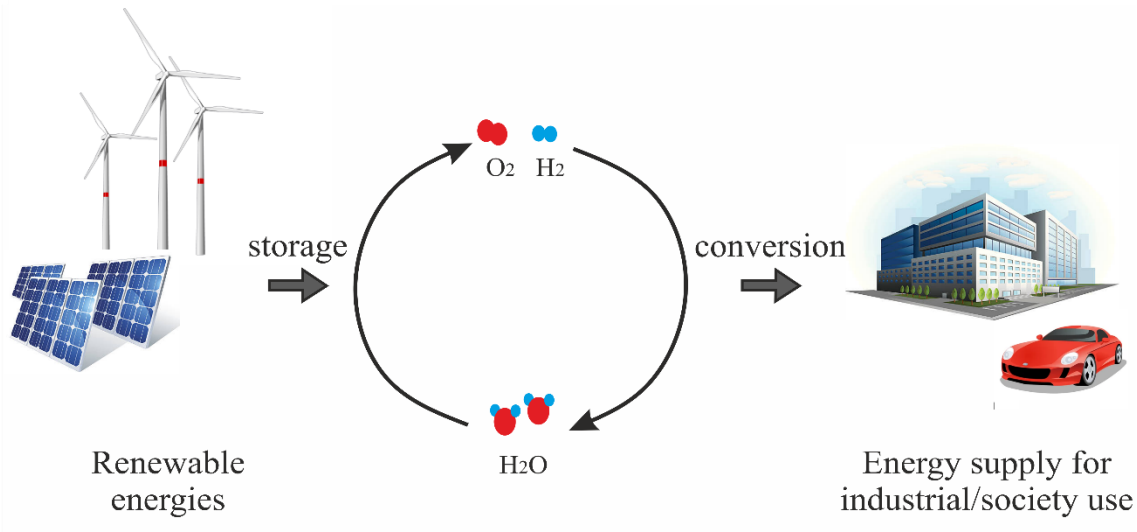

Figure 2.3. Process of energy storage and conversion through water splitting.

The water electrolysis process occurs within electrochemical cells having a common setup containing two counter-charge electrodes connected to a direct current power supply immersed in a reaction medium [46]. The electrical current flows through the electrodes generating voltage and decomposing water molecules into hydrogen and oxygen gases through two half-reactions. The reduction reaction takes place on the cathode and is known as hydrogen evolution reaction (HER), whilst the oxidation reaction happens on the anode and is named oxygen evolution reaction (OER) [21]. These half-reactions present some particularities according mainly to the development stage of technology, electrolyte, charge carrier (H^+, O^{2-}, OH^-) employed, and operational conditions.

Currently, both the application and research scales are mainly concentrated on three devices: Polymer Electrolyte Membrane (PEM) electrolysis, Solid Oxide Electrolysis (SOE) and Alkaline Water Electrolysis (AWE) [38].

The PEM water electrolysis (Figure 2.4 (a)) is very similar to the PEM fuel cell technology. In both cases, a solid polysulfonated membrane is used as the electrolyte and gas separator. The membrane is the core part of the process because it provides high proton conductivity and operation pressure (40 MPa), low gas crossover, compact design, as well as enables direct splitting of water molecules generating highly pure hydrogen and releasing oxygen [48]. For that, water is pumped to the anode side, where it is oxidized producing oxygen (O_2), protons H^+ and electrons e^- (Equation (2.1)).

The charge carrier (protons H^+) passes through the proton exchange membrane reaching the cathode side and simultaneously preventing the transport of other gases. Thus, two H^+ ions are reduced forming H_2 molecules, as shown in Equation (2.2), whilst electrons on the anode side exit the system thanks to an external power circuit that provides the driving force for reactions [49].

$$2H_2O \rightarrow 4H^+ + O_2 + 4e^- \text{ (anode)} \quad (2.1)$$

$$2H^+ + 2e^- \rightarrow H_2 \text{ (cathode)} \quad (2.2)$$

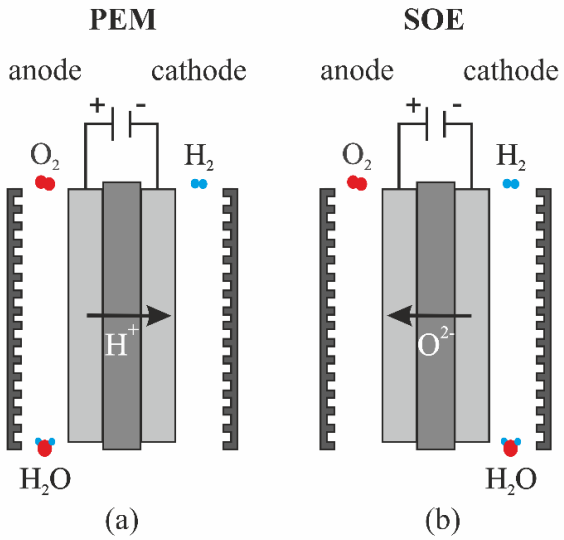

Figure 2.4. Schematic illustration of PEM (a) and SOE technique (b).

The advantages of this process are mainly attributed to the membrane's low thickness, which ranges from ~20 to 300 µm. On the other hand, the capacity to operate under high pressures must be carefully evaluated as it brings associated problems. The increase in operational pressure results in a cross-permeation issue, which, above 10 MPa, turns necessary employing thicker membranes and internal gas recombiners to keep the critical H_2 and O_2 concentrations under a safety threshold of 4vol% H_2 in O_2 [32].

In contrast with the previous case, in Solid Oxide Electrolysis (SOE) (Figure 2.4 (b)), water molecules are reduced at the cathode side producing two molecules of H_2 and two O^{2-} ions, as demonstrated in Equation (2.3). These O^{2-} ions are then oxidized at the anode forming a molecule of O_2 (Equation (2.4)). Usually, SOE systems work at temperatures around 500 to 1000 °C. Due to this relatively high temperature, the process requires both heat and electric input [49].

$$2H_2O_{(g)} + e^- \rightarrow 2H_{2(g)} + O_2^- \text{ (cathode)} \quad (2.3)$$

$$O_2^- \rightarrow O_{2\,(g)} + e^- \text{ (anode)} \quad (2.4)$$

The possibility to operate at high temperatures is considered an advantage of SOE as it has potential to increase water electrolysis efficiency. Nonetheless, it provokes harsh and fast degradation of cell components, hindering its transition from R&D to the commercial stage [48,51].

The most mature water electrolysis technology is AWE, which is conducted in liquid alkaline electrolytes. In AWE devices, an alkaline aqueous solution such as NaOH or KOH is used as the electrolyte. The KOH solution is preferred because it has a higher ionic conductivity, which is around 40 to 50% greater than that of NaOH at optimal weight percentage [52].

In this setup, the electrodes are immersed in the electrolyte and separated by a hydroxide and water-permeable gas-tight diaphragm to maintain the gases separated as well as guarantee process efficiency and safety [53]. A direct current (DC) is applied to keep the electricity balance and allow electrons to flow from the negative terminal of the DC source to the cathode where water reduction produces highly pure hydrogen (99.5 to 99.99%) and hydroxide anions. These anions diffuse through the diaphragm reaching the anode side where oxidation occurs releasing electrons that return to the positive terminal of the DC source (Figure 2.5) [54]. The half-reactions involved in this system can be observed in equations (2.5) and (2.6), respectively.

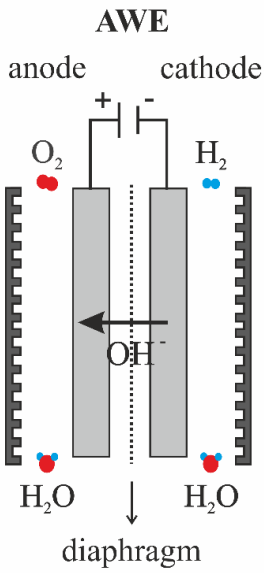

Figure 2.5. Schematic illustration of Alkaline Water Electrolysis setup.

$$2H_2O_{(g)} + 2e^- \rightarrow H_{2\,(g)} + 2OH^- \text{ (cathode)} \quad (2.5)$$

$$4OH^- \rightarrow 2H_2O + O_2 + 4e^- \text{ (anode)} \quad (2.6)$$

The AWE has several advantages over PEM electrolysis, among which its low cost, commercial applicability and mature technology can be highlighted. The kinetics of redox reactions is hampered in PEM electrolyzers' because of the acidic environment. More than that, such a system requires costly noble metal catalysts and materials for the bipolar plates. Additionally, AWE is the most developed and commercialized for operations at temperatures below 150 °C [55]. Similarly, SOE setup is much less convenient than AWE because its operation needs highly specialized and costly materials, and it owns issues related to electrodes' mechanical stability [26,51].

The water electrolysis under alkaline media augments the range of utilizable electrocatalysts to earth-abundant materials, which does not happen if the process is carried out under acidic media [8]. However, AWE presents some drawbacks like its low efficiency of around 60 to 70% compared to PEM and SOE, high ohmic losses in the electrolyte, and low current densities (0.2-0.4 $A.cm^{-2}$) caused by bubbles formed during reaction which decrease the electrodes' effective areas as well as increase the resistance of electrolytes. Likewise, the sluggish kinetics of HER and OER because of high overpotentials is a substantial issue to be overcome to achieve effective electrocatalytic reactions [40,56].

In light of these aspects, herein the fundamentals of AWE will be addressed from a scientific standpoint for a better comprehension of this process's characteristics and improvements required for the energy future. As already stated, numerous factors must be cautiously considered to achieve an efficient water electrolysis process. Given these demands, the process must be evaluated from both the thermodynamics and kinetics perspective, as will be done in the following subsection.

2.2.1. Thermodynamic and kinetic considerations

Water molecules are thermodynamically stable, consequently, the production of hydrogen and oxygen by electrolysis can only occur if the minimum potential, i.e. equilibrium or reversible cell voltage E_{eq} necessary for dissociation is overcome [57]. The electrolyzer cell potential and operating temperature of a water-splitting system have a relationship delimited by the equilibrium and thermoneutral voltage lines, as depicted in Figure 2.6. Below the equilibrium voltage, H_2 cannot be generated because the splitting process is slow due to phenomena like activation energy barrier, low reaction rate and bubbles formation [8,58].

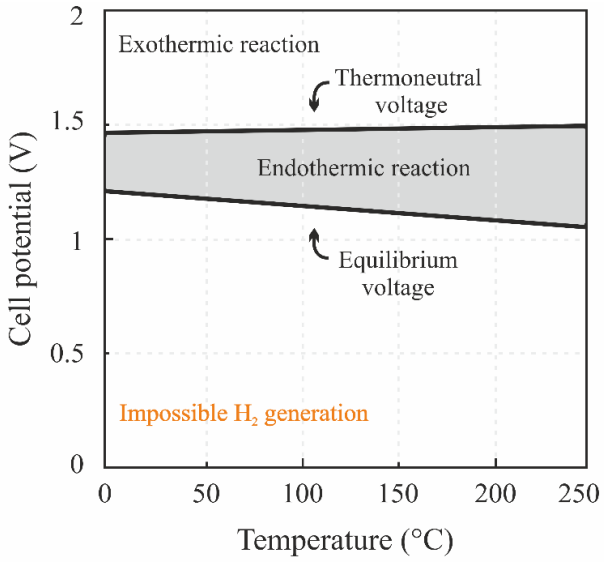

Figure 2.6. Cell potential for ideal hydrogen production by water electrolysis as a function of temperature, adapted from [45].

The minimum energy necessary to generate hydrogen as a function of temperature and pressure is provided to the electrodes by the Gibbs free energy (ΔG) and is equal to 237 $kJ.mol^{-1}$ [49]. The equilibrium voltage is the theoretical minimum thermodynamic potential (E_{eq}) whereby the dissociation of water molecules can occur at standard conditions (T° = 298.15 K

and P° = 1 bar). Knowing this minimum energy zF necessary for such a reaction, the E_{eq} of 1.23 V is determined according to equation (2.7) [54].

$$E_{eq(T,P)} = -\frac{\Delta G_{(T,P)}}{zF} \tag{2.7}$$

Where z is the number of electrons transferred, and F is the Faraday constant, which corresponds to the electric charge of 1 mole of electrons (96,485 $C.mol^{-1}$).

The positive Gibbs free energy value indicates that, at room temperature, water splitting is an endothermic reaction. Hence, the system demands an overpotential (η) at the electrodes to drive the reaction from its equilibrium voltage producing significant current densities and accelerating the dissociation start. The overpotential is determined based on both the existence of accessible ions close to the electrodes' surface and the activation energy to outpace kinetic restrictions [59].

In other words, electrical energy must be provided to allow this non-spontaneous reaction to happen. This extra energy requirement causes an Ohmic voltage drop associated with the current (j) passing through the cell, as well as the sum of resistances existing in the cell (R_{ohm}). The latter is a function of electrolyte features, the form of electrodes and cell design [8]. Accordingly, equation (2.7) can be rewritten as presented in equation (2.8) for a more robust assessment.

$$E_{cell} = E_{eq} + \sum\eta + i\sum R_{ohm} \tag{2.8}$$

The thermoneutral voltage (Etn) is the real minimum voltage that must be provided to the cell to promote water dissociation. At this point, the process is neither endothermic nor exothermic, and electrical losses are equal to the heat necessary for dissociation. That is, the reaction net heat production is zero, meaning that it happens without generating or absorbing heat. The thermoneutral voltage (equation (2.9)) is dependent on the enthalpy of reaction (ΔH), which is given by the Gibbs free energy variation and the product of the process temperature (T) and entropy change (ΔS) [52], as shown in equation (2.10).

$$E_{tn(T,P)} = -\frac{\Delta H_{(T,P)}}{zF} \quad (2.9)$$

$$\Delta H = \Delta G + T\Delta S \quad (2.10)$$

In agreement with that and the first principle of thermodynamics, the enthalpy (ΔH) and entropy (ΔS) for a water-splitting Gibbs free energy of 237.22 kJ.mol^{-1} at standard conditions are, respectively, 285.84 kJmol^{-1} and 0.16 kJmol^{-1}.

Following, Figure 2.7 shows that the total energy demand (ΔH) is slightly affected by the temperature, whilst the entropic contribution (T.ΔS) rises significantly when the temperature increases. Under this condition, water molecules' splitting becomes easier as their particles can occupy different microstates and the entropy of the system also increases [58]. For that reason, the electric energy (ΔG) input required turns appreciably lower reducing H_2 production cost [26].

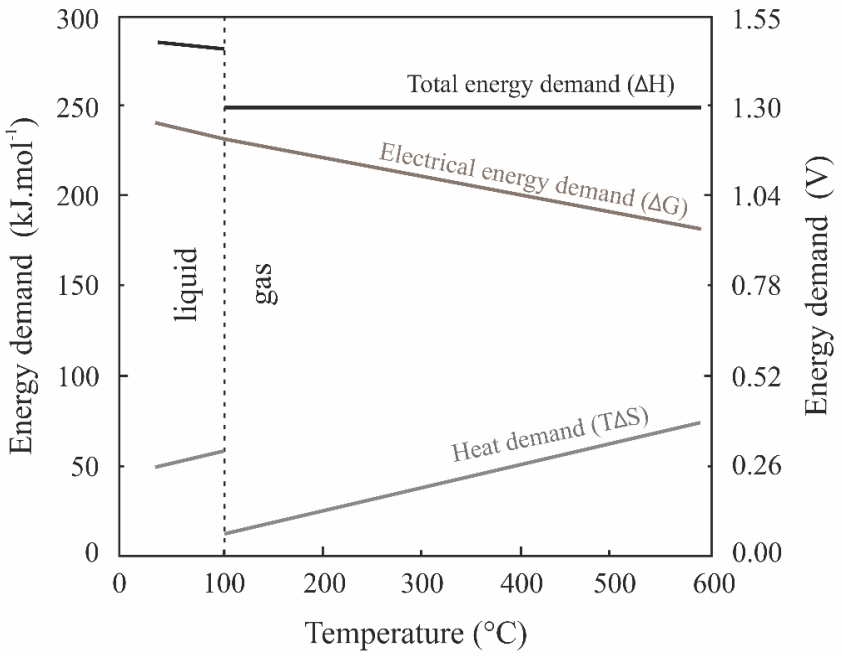

Figure 2.7. Thermodynamics of H_2O electrolysis at atmospheric pressure, adapted from [26].

On the other hand, the electrical, transport and electrochemical reaction resistances must be taken into account, as they can significantly affect the process's effectivity. The electrical resistance is related to the external electrical circuit resistance and can be calculated by Ohm's law, as follows in equation (2.11).

$$R = E/j \tag{2.11}$$

Where *j* is the current passing through the conductor when the voltage E is applied solely at the circuit.

As previously discussed for equation (2.8) description, R_{ohm} is related to resistances existing within the cell. Thus, it is a sum of the resistances of the electrolyte (R_e), diaphragm (R_d), bubbles (R_b), and circuit (R_c), as presented in equation (2.12).

$$\sum R_{ohm} = R_e + R_d + R_b + R_c \tag{2.12}$$

The R_e is associated with two factors: solution composition and the distance of electrodes. Regarding the solution, the more conductive the salt employed, the more conductive the electrolyte and, consequently, the smaller R_e. However, it is imperative to point out that this condition is valid until a limit of around 20 to 30% of salt, once greater concentrations would cause cell corrosion and destruction of the diaphragm [60].

The transport resistances comprise physical effects such as resistances to ionic transfer and transport of split species through the diaphragm, as well as the presence of bubbles on the surface of electrodes and in the electrolyte solution. Although the diaphragm is necessary to separate produced gases, its presence can restrain OH^- transfer, causing low current densities, besides reducing the free volume of liquid, leading to a reduction in conductivity and an increase in ohmic losses [26]. Furthermore, there is a need to keep the diaphragm and electrodes at defined distances from each other to avoid interferences between oxidation and reduction half-reactions. Such a condition also leads to bubbles formation, reducing the electrodes' active area and free volume of electrolyte. Moreover, bubbles dispersion during water electrolysis causes poor conductivity and increases R_e.

The heat generated by electrical and transport resistances is an ohmic loss described according to Joule's law and transport phenomena, respectively. Reaction resistances arise from the requirement of overpotentials to surpass the activation energies of hydrogen and oxygen formation, hence, provoking an increase in the overall cell potential. Both overpotential and ohmic losses increase with the current density and, then, may cause inefficiencies in the

electrolysis. These reaction energy barriers own implications on the kinetics rate and can be expressed by Arrhenius law [54].

The total energy demand can be determined according to the reaction enthalpy of liquid water formed along with the whole process. Thus, the energy efficiency is defined based on the higher heating value (HHV) of H_2 generation, which evaluates the production of hydrogen per unit of electrical energy input. For ΔH of 285.8 $kJmol^{-1}$, the HHV corresponds to the thermoneutral cell voltage (E_{tn}) of 1.48 V/cell.

It implies that, at standard conditions and under this voltage, H_2 and O_2 would be generated with a thermal efficiency of 100%. Nevertheless, a practical cell requires a voltage higher than that to attain the splitting reaction and also produces excess heat. Normally, a real water electrolysis setup operates at a constant cell voltage varying from 1.6 to 2.0 V or at a constant current density of 1.0 to 2.0 Acm^{-2}, depending on the electrocatalytic material employed for HER and OER as well as on the pH of the electrolyte [45]. In this perspective, the energy efficiency can be more reasonably calculated by the voltage efficiency as shown in equation (2.13).

$$voltage\ efficiency = \frac{E_{tn}}{Cell\ operating\ voltage} \tag{2.13}$$

As for the thermal efficiency, it is based on the enthalpy change (total cell voltage) as energy input and can reach values higher than 1 due to heat absorption from the surroundings [44].

Besides these effects, the electrocatalytic material has a strong influence in the process. The performances of OER and HER electrocatalysts depend on the entanglement between their intrinsic properties (composition, crystal structure, exposed facets, active surface area, partial charge of surface atoms, charge delocalization) and the ones of the overall electrode (electronic conductivity, porosity, durability) [61,62]. To evaluate the performance of an electrocatalytic process, certain parameters associated with experimental conditions and properties of the catalyst employed must be taken into account, as summarized in Figure 2.8. For instance, the catalyst activity is typically characterized by overpotential, exchange current density and Tafel slope, which can be assessed from polarization curves. The surface area of a catalyst is widely investigated by the electrochemically active surface area (ECSA) measurement, to determine

its specific activity, also called surface-area-normalized activity. It is commonly examined on metal surfaces since they possess the capacity to adsorb various species facilitating the determination via characteristic reactions like H adsorption/desorption [63]. Concerning stability, overpotential or current changes over time, they are investigated by chronoamperometry, chronopotentiometry, or cyclic- and linear sweep-voltammetry (LSV) curves.

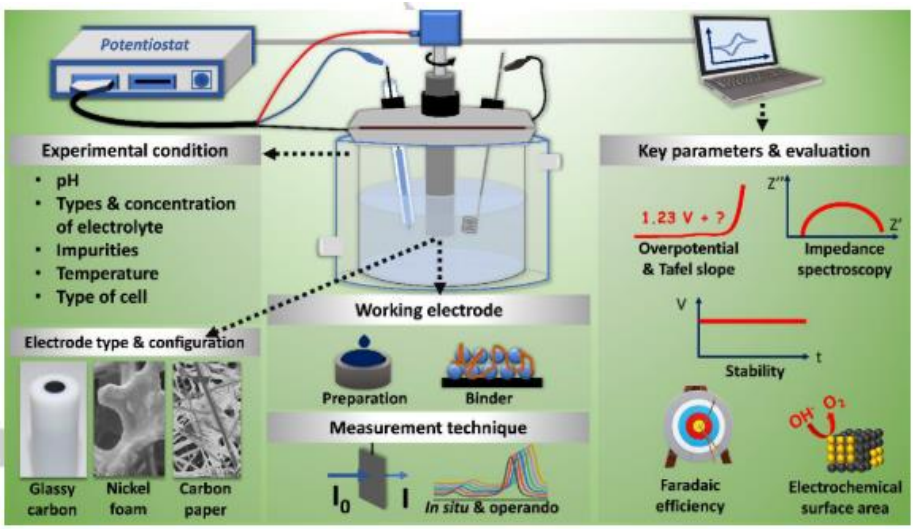

Figure 2.8. Summary of important parameters to evaluate activity during a water electrolysis process.

2.2.2. Hydrogen Evolution Reaction (HER) mechanism

Besides all phenomena described above that could affect AWE efficiency, the sluggish kinetics of HER and OER is another substantial problem. Even though the water electrolysis under alkaline media is preferable to acidic media due to the greater options of electrocatalysts, the HER activity is 2-3 orders of magnitude lower in this case, due to its poor water dissociation capacity [8].

HER is favored in acidic mediums whilst OER is better performed in alkaline environments [64]. Under alkaline conditions, HER happens through two electron-transfer processes (Figure 2.9): (i) the proton discharge step (Volmer reaction) and (ii) the generation of H_2 gas. The latter occurs either by electrochemical (Heyrovsky step) or chemical desorption

(Tafel step) or both [49,65]. These possibilities are also named Volmer/Heyrovsky and Volmer/Tafel reactions.

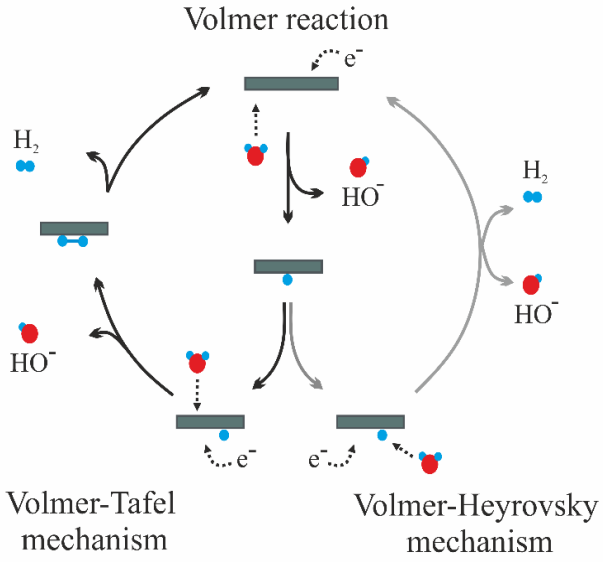

Figure 2.9. HER mechanism on the electrode surface in AWE, adapted from [49].

In the Volmer reaction (equation (2.14)), deposited/adsorbed hydrogen intermediates (H^*) are formed on the electrode surface (M) via protons (H_2O) reduction.

$$H_2O + M + e^- \rightarrow H^* + OH^- \qquad (2.14)$$

Then, the adsorbed H* passes through removal/desorption by two paths to generate H_2 gas. By the Heyrovsky reaction, due to the low surface coverage of H*, the adsorbed H* intermediates react with both proton and electron to produce H_2 [49,65]. This reaction is represented in equation (2.15). The Tafel reaction arises when the surface coverage of H* is high, allowing the combination of two adjacent H* to form H_2 (equation (2.16)).

$$H_2O + e^- + H^* \rightarrow H_2 + OH^- \qquad (2.15)$$

$$H^* + H^* \rightarrow H_2 \qquad (2.16)$$

According to the current state of knowledge, the cause of HER slow kinetics is still controversial, however, the kinetic barrier for the formation or desorption of adsorbed H* is considered an important factor [66]. Other authors mention that the HER activity has water

adsorption and dissociation, hydrogen binding energy and OH^- adsorption as the four factors of major influence [67].

2.2.3. Oxygen Evolution Reaction (OER) mechanism

With regards to the anode side half-reaction (OER), it has sluggish kinetics and requires an overpotential greater than that of HER to assist the adsorption and desorption of intermediates generated during its four-proton electron-transfer process [68]. This requirement results in the consumption of excess energy and causes a decrease in conversion efficiency [69]. In consequence of that, OER is the key part of the overall efficiency of electrochemical water splitting [34].

This multi-electron transfer reaction is carried out in several steps (Figure 2.10), initiating with the oxidation of hydroxide ions, as expressed in equation (2.17). Thus, a proton and electron removal occur transforming MOH* into MO* (equation (2.18)). Thereafter, there are two reaction pathways for producing oxygen. One is by reacting two MO*, as demonstrated in equation (2.19). This step demands a large thermodynamic energy barrier though [65].

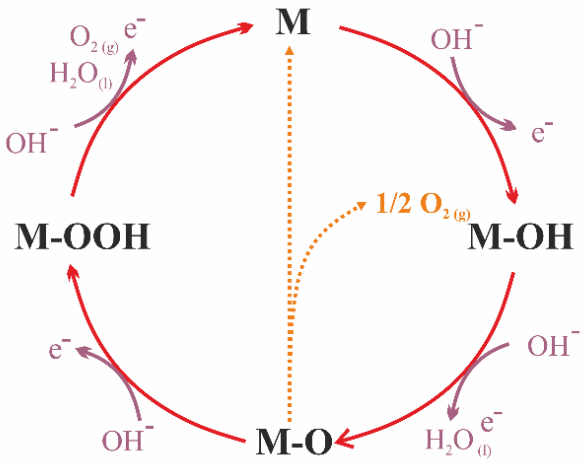

Figure 2.10. OER mechanism for AWE: formation of peroxide (M-OOH) intermediate (red lines) and the direct reaction of two adjacent oxo (M-O) intermediates forming oxygen (orange line), adapted from [67].

$$M + OH^- \rightarrow MOH^* + e^- \quad (2.17)$$

Where M is the active site of the catalytic surface and * denotes surface-adsorbed species.

$$MOH^* + OH^- \rightarrow MO^* + H_2O + e^- \quad (2.18)$$

$$2MO^* \rightarrow 2M + O_2 \quad (2.19)$$

The other way consists of a nucleophilic attack of OH^- on MO* coupled with a one-electron oxidation reaction to generate MOOH*, according to equation (2.20). Sequentially, it goes through another one-electron transfer process finally evolving the O_2 molecule and the free active site (M) (equation (2.21) [65].

$$MO^* + OH^- \rightarrow MOOH^* + e^- \quad (2.20)$$

$$MOOH^* + OH^- \rightarrow M + O_2 + H_2O + e^- \quad (2.21)$$

It can be seen from this conventional OER mechanism that all intermediates formed along the process interact with the catalytic surface (M) through an oxygen atom (MO, MOH, MOOH) [70]. In a pioneering study published by Rüetschi and Delahay (1955) [71], it was found that the overvoltage decreases linearly with an increase in M-OH bond energy on metal surfaces (Ag, Au, Cd, Co, Cu, Fe, Ni, Pb, Pd and Pt), owing paramount effect on the overall OER activity. Therefore, interactions between the catalyst surface and intermediates have a direct impact on the process efficiency [67]. Based on this, developing highly efficient and cost-effective electrocatalysts is highly necessary to place alkaline water electrolysis on a commercial scale. Nonetheless, the currently used materials pose a challenge for that purpose due to some of their specific features.

2.3. Electrocatalysts currently used for HER & OER in alkaline media

Classically, platinum and Platinum Group Metal (PGM)-based structures are widely employed as electrocatalysts for electrochemical power sources. Pt is the state-of-the-art catalyst for HER reactions, being normally supported on carbon electrodes [72,73]. This vast use is particularly due to its higher activity and stability compared to other metal catalysts. For OER the benchmark catalysts are IrO_2/RuO_2-based materials [74], as they own high stability, small overpotential at practical current densities and small Tafel slope [75]. Other examples of

catalytic materials for this half-reaction are Pt and Pd, however, they exhibit lower performance, according to this sequence: Ru>Ir>Pt>Pd [68].

Electrocatalysts based on non-noble transition metals (TM) are inexpensive, abundant and environmentally friendly. They can display catalytic performances comparable to state-of-the-art noble metals, particularly in alkaline media [13]. This makes them good candidates for AWE, and has therefore triggered a rush in the exploration of non-noble TM-based HER and OER electrocatalysts. Apart from supported 3d TM such as Mo, Fe, Co, Ni [76], 3d TM-containing advanced ceramics including TM borides [77–79], carbides [80,81], nitrides [82,83], phosphides [84,85], and oxides [86,87] are extensively studied for their attractive HER and/or OER performances, which are mainly attributed to electron transfer between the 3d (or 4d) orbitals of TM and the 2p/3p orbitals of electronegative B, C, N, Si and P. Further, in alkaline media, the surface of these materials is oxidized in OER conditions providing oxy(hydr-)oxides surface layers, which are active toward OER and benefit from charge transfer with the conductive TMX cores.[11] However, the development of such electrocatalysts suffers from conventional preparation methods at high temperatures, yielding uncontrolled particle size, morphology and low surface area, hence, restricting the density of active sites. Thus, the current lack of specific surface associated with the limited intrinsic electronic conductivity of these compounds hinders performance improvements. Both high specific surface area and high electronic conductivity are essential for electrocatalysis and can be addressed by materials design as proposed in the present thesis via the Polymer-Derived Ceramic (PDC) route.

2.4. Polymer-Derived Ceramics (PDCs) route as an *in-situ* non-noble metal growth approach

Designing matter from atomistic to macroscopic scale is a unique attribute of chemical materials technologies, such as those based on well-defined molecular and polymeric precursors, to solve problems arising from ceramic manufacturing with traditional powder-based technologies.

The Polymer-Derived Ceramics (PDCs) route represents an outstanding chemical approach for that purpose. This emerging chemical process was first reported in the 1960s and started to be recognized in the 1970s due to its potential for materials science when the first practical application was reported by Veerbeck, Winter, and Yajima [88–91].

Fundamentally, the PDC route consists of generating advanced ceramics by the thermolysis of organosilicon polymers' that contain silicon atoms in the backbone and are denoted as preceramic polymers. Under a controlled atmosphere and appropriate thermal treatment, these precursors provide ceramics possessing both tailored chemical composition and a closely defined nanostructure organization. In addition, such a route enables various possibilities for designing more or less complex shapes that cannot be generated via conventional processes. These advanced ceramics are highlighted by the fact that they are additive-free materials obtained at low pyrolysis temperatures, generally between 800 and 1200 °C, which is lower than the required in conventional ceramics processing [92,93]. These conditions provide excellent corrosion and creep resistance to the final product, besides reducing structural damage, as the low thermal treatment regime allows the consolidation of all elements within the polymeric structure to the ceramic [94,95].

The molecular structure of the preceramic polymer has a direct influence on the composition, phase distribution, as well as microstructure of the final ceramic. Thereby, PDCs' physicochemical properties can be adjusted by designing molecular precursors [93,96]. A general representation of the molecular structure of a preceramic polymer is shown in Figure 2.11.

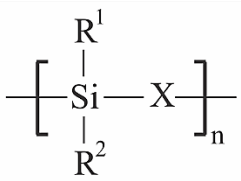

Figure 2.11. Simplified structure of preceramic polymers.

Their classification is established according to the X group bounded to the Si atom of the polymer backbone. As such, X denotes, for example, polysilanes (Si), polycarbosilanes (C), polysiloxanes (O), polysilazanes (N), polyborosilanes (B), or the combination of two of these classes, as depicted in Figure 2.12. The functional groups represented by R^1 and R^2 are commonly hydrogen, methyl, vinyl and/or phenyl, and are responsible for properties like solubility, thermal stability and viscosity of the polymer [93]. Consequently, by adjusting the preceramic polymer used, both micro- and macroscopic features of the final ceramic can be controlled.

In this context, the use of adequate precursors is indispensable to determine the final features, meaning that, the polymer should have a molecular mass sufficiently high to prevent

the volatilization of low molecular components, rheological properties suitable for processability and reactivity for the crosslinking step to grant high ceramic yield [97]. Under a controlled atmosphere and appropriated thermal treatment, these precursors provide Si-containing ceramics possessing both tailored chemical composition (SiOC, SiCN, Si_3N_4 or SiC) and a closely defined nanostructure organization [92,93].

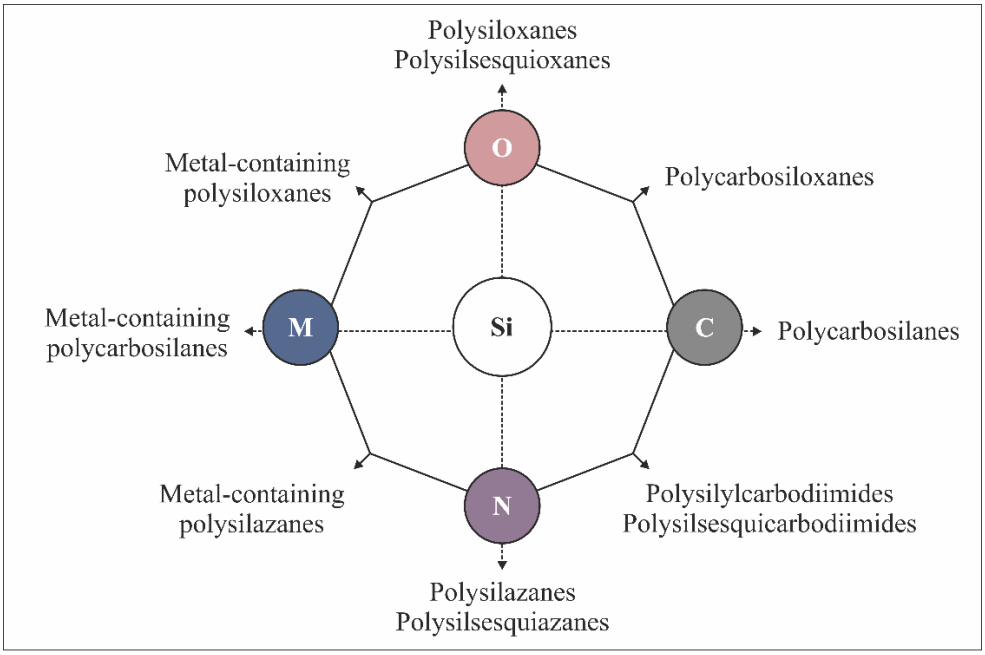

Figure 2.12. Distinct classes of Si-based preceramic polymers, adapted from [99].

A flow diagram of the single steps involved in the design of advanced ceramics from molecular precursors and preceramic polymers is shown in Figure 2.13. Processing ceramics *via* preceramic polymers involves the synthesis (from molecular precursors as monomers), crosslinking (to form an infusible network) and transformation, *i.e.*, ceramization, *via* pyrolysis of these precursors into amorphous covalently bound ceramics. Subsequently, an optional heat treatment at a higher temperature will achieve the crystallization of the amorphous ceramics.

Because of the possibility of controlling the cross-linking degree, the type of bonds linking monomeric units and the nature of functional groups or substituents attached to the polymer network, preceramic polymers with tailored rheological properties can be synthesized. Thus, the chemistry behind the synthesis of preceramic polymers can be well tailored in order to form, in the next step, as-synthesized preceramic polymers (that can contain active or passive fillers) into the desired shape. This is accomplished by a shape-forming process [93,97,98].

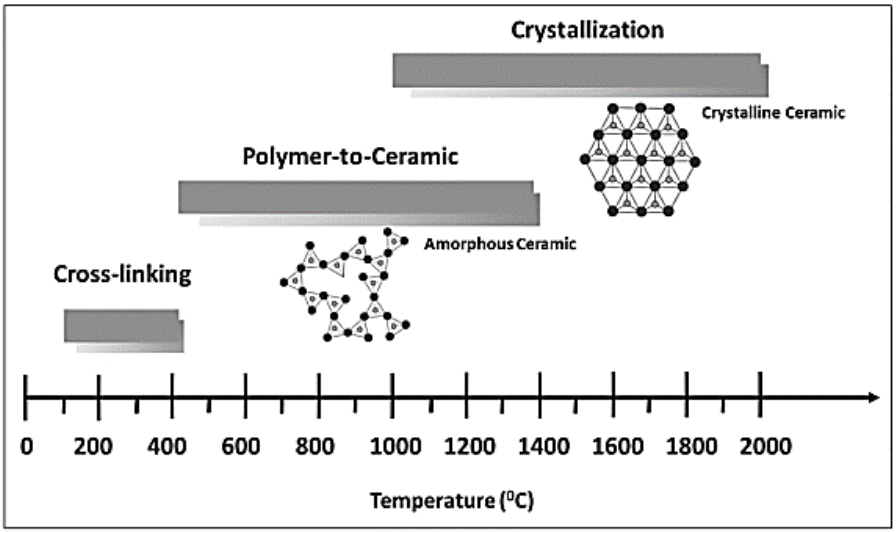

Figure 2.13. Polymer-to-ceramic transformation and microstructure evolution according to pyrolysis temperature, adapted from [93].

As-obtained PDCs can display functional properties of great interest in many fields such as catalysis, gas separation, hydrogen storage and fuel cells [99].

The design of pure TM borides, carbides, nitrides, phosphides, and oxides as required to activate OER is complex via the PDCs route and usually yields mixed phases. An alternative strategy is based on the reaction of organosilicon precursors with TM-based species [96] to form organometallosilicon precursors and then, after pyrolysis, TM-containing PDCs made of i) TM (= Co [100–102], Ni [103–107], Fe [108]) nanoparticles embedded in amorphous Si-based PDCs such as silicon carbonitride ($Si_xC_yN_z$ (x+y+z = 1)), oxycarbide ($Si_xC_yO_z$ (x+y+z = 1)) or nitride (Si_3N_4), ii) TMSi (Pd_2Si) nanoparticles dispersed in $Si_xC_yN_z$ [109], iii) TMN (TiN) nanoparticles dispersed in Si_3N_4 [110] and iv) TMC (TiC) nanoparticles dispersed in silicon carbide (SiC). These nanocomposites are robust and reusable catalysts because a certain portion of TM-based nanoparticles migrates to the surface of the matrix upon pyrolysis [107].

To the best of our knowledge, there is only one paper dealing with PDCs as electrocatalysts for OER [111]. The silica-based PDCs decorated by intermetallic nickel silicides (Ni_2Si, Ni_3Si) exhibited a 50 mV decrease of the OER onset potential compared to its Co analog with OER kinetics almost similar to RuO_2. However, oxidation of the PDCs occurred during processing and a temperature as high as 1200 °C was required to display this OER performance, which is too high to keep a suitable specific surface area (SSA). There is also little attention paid to HER electrocatalysts based on TM-containing PDCs [112].[70] In a first

report [113] on the *in situ* formation of nanosized $Mo_{4.8}Si_3C_{0.6}$ embedded in a SiC matrix; a nanocomposite that exhibited electrocatalytic activity and excellent durability in acidic HER (low overpotential of 138 mV at 10 $mA.cm^{-2}$ and 90% of the performance retained after 35h) was obtained. Subsequently, a $Mo_{4.8}Si_3C_{0.6}$@SiC nanocomposite demonstrated superior HER performances (low overpotential of 119 mV at 10 $mA.cm^{-2}$). However, such materials were prepared above 1400 °C, which is detrimental to the surface area [112].

Therefore, the PDC route nano-structuring started to be regarded as an interesting precursor approach to synthesizing highly conductive and high surface area ceramics that can act as substrates containing *in situ* generated crystalline, small and dispersive earth-abundant 3d block transition metal nanoparticles. Such conductivity is associated with the presence of sp^2 carbon, whereas, the high surface area is linked to the evolution of gaseous species taking place during the low-temperature thermolysis regime. Hence, the PDC design strategy can open the way for the use of advanced ceramics for water oxidation in alkaline medium. As-obtained TM/PDCs are expected to: (i) display long-term stability due to the strong nanocrystal-matrix interaction and due to its expected corrosion resistance; (ii) reduce interface resistance; (iii) expose more active sites; (iv) avoid active sites aggregation during the electrochemical process leading thereby to a constant catalytic activity; and (v) have practical applicability.

2.5.Conclusions

This literature review summarizes the advantages provided by AWE to split water producing produce dioxygen (O_2) and dihydrogen (H_2) at the anode and cathode of an electrolyzer. The AWE is considered an environmentally friendly energy production process especially because it can generate highly pure H_2 whilst releasing only dioxygen into the air. Even though, catalysts currently used to promote such electrochemical reactions are based on costly and scarce noble metals, posing a barrier to large-scale energy production. To circumvent these issues, it is indispensable to employ inexpensive and earth-abundant materials as well as increase catalysts' conductivity, and thermal and chemical stabilities.

For that purpose, several studies on transition metals have been realized by different ceramic processing, however, little attention has been given to the PDC route, which enables the generation of robust ceramics with features easily adjustable by designing according to the application requirements. In light of the current state-of-technology development, this thesis

reports the chemical modification of a polysilazane with different cobalt and nickel complexes aiming to achieve high specific surface area for the alkaline water electrolysis and improve the OER kinetics.

3. MATERIAL AND METHODS

In this chapter, the experimental part of this study is described. It is split into four main sections: 1) materials including reagents, precursors and solvent, 2) synthesis procedures of transition metal (TM)-modified polysilazanes with specific metal complexes, 3) heat-treatment procedures to prepare the nanocomposites and 4) characterization techniques including multi-scale analysis and electrochemical tests.

Courses of materials science and chemical engineering were performed at *Universidade Federal de Santa Catarina* (UFSC), in Brazil from 2017 to 2019. The experimental part dedicated to materials synthesis and their characterization was executed in France, as part of a cotutelle agreement with *Université de Limoges* (UNILIM). This part was developed from 2019 to 2021 at the *Institut de Recherche sur les Céramiques* (IRCER) an institute belonging to CNRS and UNILIM, France. Electrocatalysis tests and ICP characterization were carried out at *Institut de Chimie des Milieux et Matériaux de Poitiers (IC2MP)*, University of Poitiers, France.

3.1. Materials

All chemical products necessary for synthesis were handled in an argon-filled glove box (Jacomex JP, Campus-type, with O_2 and H_2O concentrations kept below 0.1 and 0.8 ppm, respectively. The commercially available compounds used are listed in Table 3.1.

Table 3.1. Chemical products employed in the experimental part.

Compound class	Chemical	Mw (g.mol^{-1})	Manufacturer
Organosilicon polymer	Durazane® 1800, vinyl polysilazane	64.365*	DurXtreme GmbH
Metal acetates	Co(II) acetate tetrahydrate ≥98% Nickel(II) acetate tetrahydrate ≥99%	249.08 248.84	Merck life science
Metal acetylacetonates	Cobalt(II) acetylacetonate ≥99% Nickel(II) acetylacetonate, 95%	257.15 256.91	Sigma-Aldrich
Metal chlorides	Cobalt(II) chloride, anhydrous Nickel(II) chloride, 98%	129.84 129.60	Merck life science
Solvent	N,N-Dimethylformamide, 99.8%	73.09	Fischer Scientific

* Theoretical monomeric unit of the polymer.

As indicated in Table 3.1, metal complexes employed can be divided into three main groups, which are depicted in Figure 3.1. The first one is composed of metal acetate

tetrahydrates, followed by the second group which involves metal acetylacetonate compounds. The third group is related to metal chlorides.

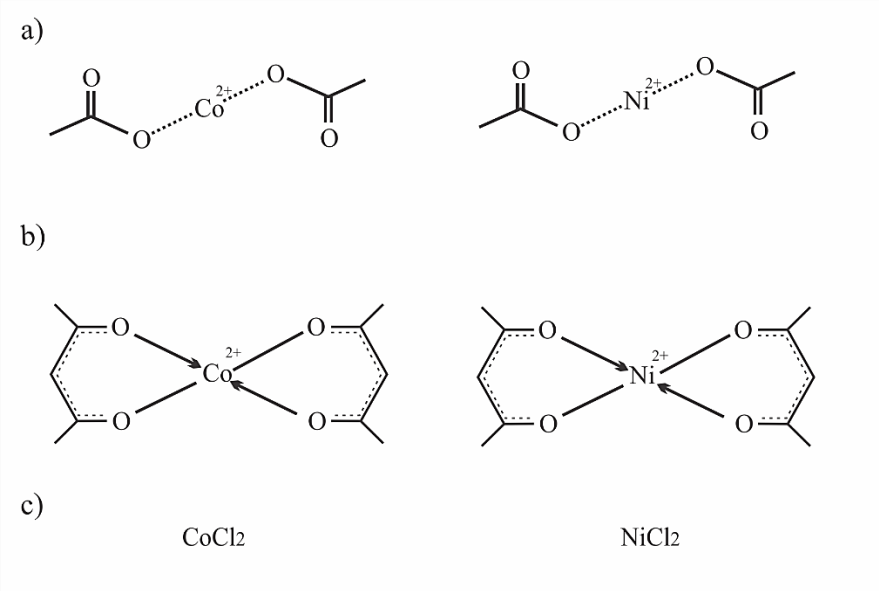

Figure 3.1. Chemical structures of metal acetates (a) acetylacetonates (b), chloride (c) and amine chloride complexes.

The organosilicon polymer used in all syntheses was a vinyl polysilazane (Durazane® 1800), a commercially available polysilazane from durXtreme GmbH, Ulm (Germany) whose simplified chemical structure is shown in Figure 3.2.

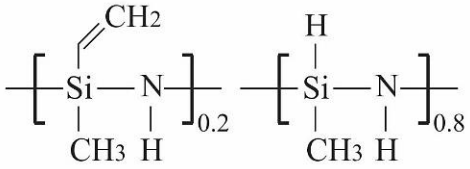

Figure 3.2. Simplified chemical structure of Durazane® 1800.

In the manuscript, this polymer is labeled PSZ. Its physical properties given by the Merck company are presented in Table 3.2.

Table 3.2. Physical properties of polycarbosilazane HTT1800.

Solubility	Hexane, toluene, DMF
Viscosity (mPa.s)	20-50
Density (g.cm^{-3})	1.0
Crosslinking temperature (°C)	175-200
Appearance	Pale yellow liquid

3.2. Synthesis procedure

All syntheses were carried out in a purified argon atmosphere successively passing through a column of phosphorus pentoxide and then a vacuum/argon line employing standard Schlenk techniques (Figure 3.3). Previous to the introduction of reactants, the cleaned glassware was stored in an oven at 95 °C overnight before being connected to the vacuum/argon line, assembled and pumped under vacuum for 30 min and then filled with argon.

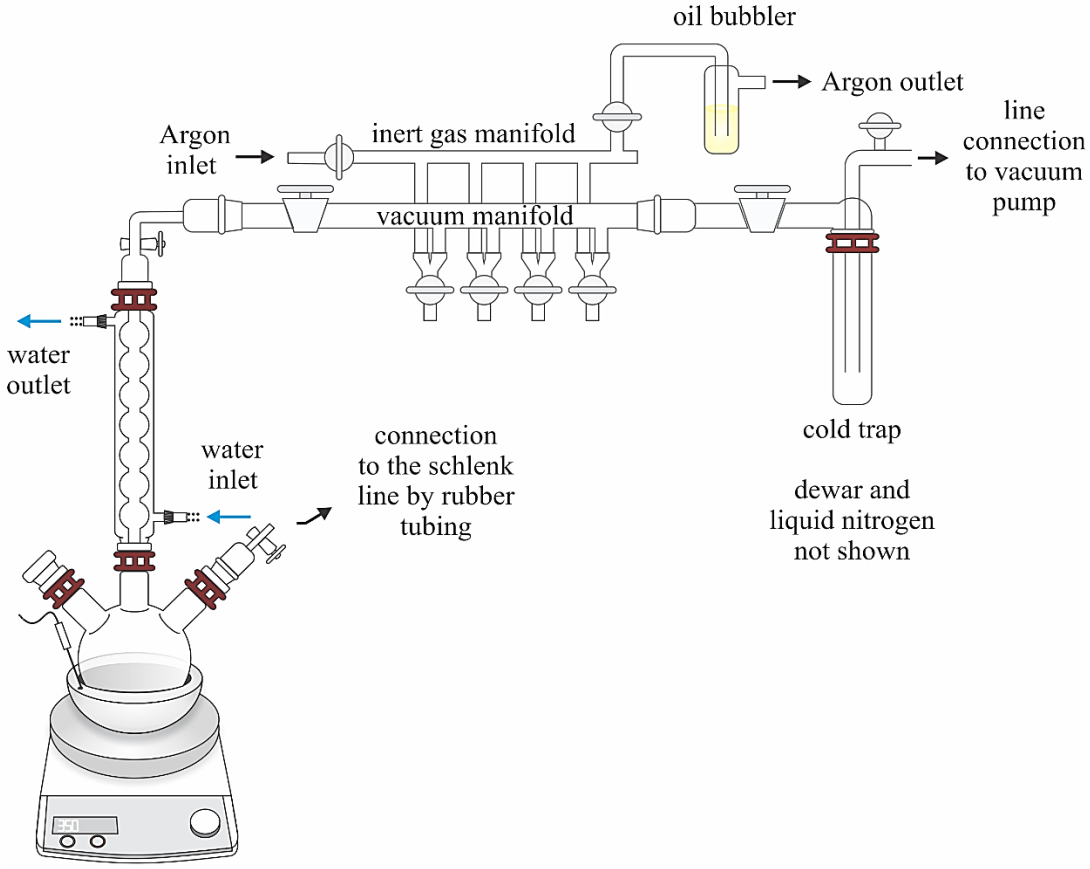

Figure 3.3. Schematic representation of a Schlenk line.

Reactions were performed in a system prepared as shown in Figure 3.4 (a). It was composed of a 3-neck round-bottom flask placed in a magnetic stirrer equipped with a heating

plate. This flask was coupled to a condenser and connected to an oil bubbler for the byproduct's outlet. One of the other two inlets was used for inserting reagents whereas the other was connected to the Schlenk-line (argon/vacuum valve) to assure the inert atmosphere, as well as for the solvent extraction under reduced pressure at the end of the synthesis.

The precursors and the 3-neck round-bottom flask were placed inside the glovebox. After being weighed, the selected metal (M) complex was introduced to the flask. Once it was removed from the glove box and connected to the Schlenk line, the solvent (DMF) was added to the system. This suspension was stirred at room temperature for 30 minutes to guarantee homogeneity. Then, the last reagent, the PSZ, was added dropwise to ensure a satisfactory mix as it is a viscous compound. The whole solution was kept under stirring at room temperature for 3 hours. Consequently, the temperature was increased up to solvent reflux (~155 °C) under static argon and vigorous stirring overnight. After cooling down, the solvent was extracted via an ether bridge (100 °C/$1.5 \cdot 10^{-1}$ mbar) (Figure 3.4 (b)) to release the precursor which was collected and stored inside the glove box for storage and further manipulation. A metal (M)-modified PSZ is therefore delivered.

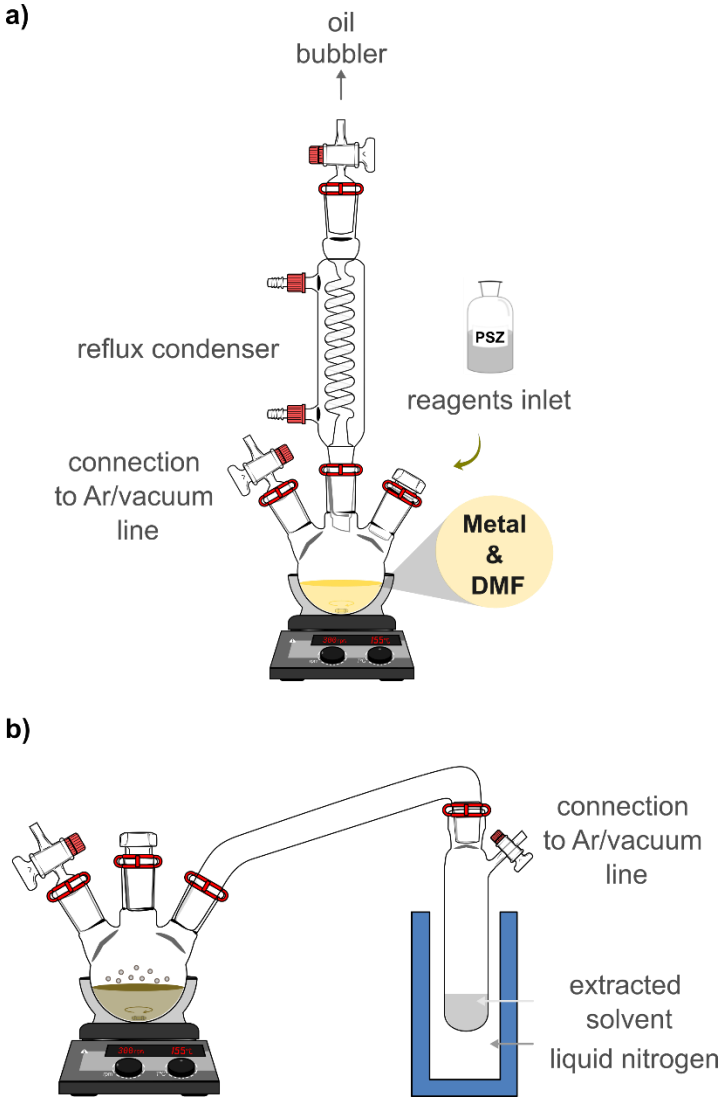

Figure 3.4. Synthesis reaction (a) and solvent extraction setup (b)

The above-described general synthesis and solvent extraction procedures were employed in all experiments of this work with adaptations depending on the metal precursor used and will be detailed in the next subsections.

3.2.1. Synthesis of M-modified PSZ using metal acetate & acetylacetonate

In this part, the description of the synthesis of metal (M)-modified PSZ using metal acetate- & acetylacetonate is provided. For reactions of PSZ with these metal precursors, a fixed molar ratio of 2.5 was evaluated. The definition of the necessary amount of a metal precursor to react with the desired quantity of PSZ in each molar ratio investigated was determined as shown in Equation (3.1):

$$\frac{n(\mathrm{PSZ})}{n\,(metal\ precursor)} = \ molar\ ratio \qquad (3.1)$$

Cobalt and nickel acetates (labeled Coac or Niac) and acetylacetonates (labeled Coacac or Niacac) were employed to react with PSZ through a molar ratio of 2.5, producing the samples labeled as PSZMacx and PSZMacacx, where, M is Co and Ni, and x is the molar ratio, as shown in Table 3.3. Prior to the synthesis, metal acetates and acetylacetonates have been dried overnight at 96 °C and kept under vacuum for one hour before being placed inside the glove box to extract water.

Table 3.3. Preceramic polymers nomenclature according to metal acetate or acetylacetonate and Si:Metal molar ratio investigated.

Metal precursor	Si:Metal ratio	Polymer nomenclature
Niac	2.5	PSZNiac2.5
Coac		PSZCoac2.5
Coacac		PSZ Coacac2.5
Niacac		PSZNiacac2.5

For all systems, the PSZ amount used was fixed at 2.0 g (30.52 mmol referred to the theoretical monomeric unit of the polymer (64.365 mol)). Therefore, taking a reaction between PSZ and Niac in a ratio of 2.5 as an example, the synthesis procedure was conducted as follows: a suspension composed of 50 mL of DMF and 3.09 g of Niac (12.42 mmol) was kept under vigorous stirring (350 rpm) for 30 minutes to promote homogenization before adding 2.0 g of PSZ dropwise under argon flow and keeping the mixture under stirring for 3h at RT. Further, the temperature was increased up to DMF reflux, for an overnight reaction. The system was then cooled down and the solvent extraction was performed via an ether bridge (100 °C/1.5·10^{-1} mbar), releasing the solid precursor named PSZNiac2.5.

3.2.2. Synthesis of metal chloride-modified PSZ polymers

For reactions between the PSZ and $NiCl_2$ and $CoCl_2$ different Si:Metal molar ratios were assessed as reported in Table 3.4. The products synthesized were labeled PSZMx where M is the metal (Ni or Co) and x is the molar ratio between precursors. The mixing of both metal chlorides with PSZ was also investigated. Thus, a molar ratio of metal to PSZ was fixed at 5,

that is, PSZ:$CoCl_2$ = 5 and PSZ:$NiCl_2$ = 5. Additionally, the ratio of PSZ:Co = 1.3 and PSZ:Ni = 0.7 was also performed to evaluate the impact of different molar ratios in the final product. For these syntheses, both $CoCl_2$ and $NiCl_2$ were simultaneously added to the flask inside the glovebox to avoid further opening of the system. These samples were named PSZNi5Co5 and PSZCo1.3Ni0.7, respectively. All these conditions were studied to determine the most appropriate molar ratio and metal precursor to obtain a material with satisfactory catalytic activities for the water electrolysis process.

Table 3.4. Preceramic polymers nomenclature according to metal chloride and Si:Metal molar ratio investigated.

Metal precursor	Si:Metal ratio	Polymer nomenclature
$NiCl_2$	10	PSZNi10
	5	PSZNi5
	2.5	PSZNi2.5
	1	PSZNi1
$CoCl_2$	5	PSZCo5
	2.5	PSZCo2.5
	1	PSZCo1
$CoCl_2$ +$NiCl_2$	5	PSZ Co5Ni5
	2	PSZ Co1.3Ni0.7

To illustrate, the synthesis of a preceramic polymer following the reaction between PSZ and $NiCl_2$ in the ratio of 2.5 is described. Thus, 2.0 g of PSZ (30.52 mmol referred to the theoretical monomeric unit of the polymer (64.365 mol)) were added dropwise under flowing argon to a suspension made of 1.61 g of $NiCl_2$ (12.42 mmol) in 50 mL of DMF at RT under vigorous stirring (350 rpm). Then, the temperature was increased up to DMF reflux under static argon and vigorous stirring overnight. After cooling down, the solvent is extracted via an ether bridge (100 °C/$1.5 \cdot 10^{-1}$ mbar) to release a solid precursor labeled PSZNi2.5 (2.5 being the Si:Ni ratio).

The polymers described in sections 3.2.2 (page 53) and 3.2.1 (page 52) were thermally treated to investigate their polymer-to-ceramic conversion as well as ceramic properties to determine the most promising for the water electrolysis essays. Details of each case will be discussed below.

3.3. Pyrolysis of preceramic polymers

The as-synthesized precursors which have been previously described have been directly pyrolyzed in the temperature range from 300 to 1000 °C in flowing argon to follow their conversion into inorganic compounds. The procedure consists of handling the sample in the glove box to introduce a controlled quantity in an alumina boat to be put in a sealed tube preventing any oxygen contamination of the sample during the transfer from the glove box to the furnace. The sealed tube is introduced and then open into a silica tube from a horizontal furnace (Carbolite BGHA12/450B) under argon and the alumina boat containing the precursors is pushed to the heat zone of the furnace. The tube is then evacuated (0.1 mbar) for 30 min and refilled with argon (99.99 %) to atmospheric pressure. Subsequently, the sample is subjected to a thermal using a heating rate of 5 °C·min^{-1} up to the desired temperature (with a dwelling time of 2 h). During this thermolysis cycle, a constant flow (120 mL·min^{-1}) of argon is passed through the furnace tube. After cooling, also under argon atmosphere, the derived inorganic compound is transferred to the glove box for further characterization. For all samples, thermolysis temperatures ranging from 700 to 1000 °C were assessed. In the case of samples PSZNi2.5 and PSZCo2.5, they were also pyrolyzed at lower temperatures (300 and 500 °C), to investigate the polymer-to-ceramic transformation, keeping the same procedure described above. All other samples were treated only at higher temperatures.

3.4. Characterization techniques

A description of the methods and conditions employed for characterizing materials produced, both in the polymeric and ceramic states is presented in this section.

3.4.1. Fourier-transformed infrared (FT-IR) Spectroscopy

The chemical bonds present in the different precursors are investigated using FTIR in transmission mode over a spectral range of 400 to 4000 cm^{-1} (Thermo Scientific Nicolet 6700). Thus, FTIR spectroscopy was used to analyze the reaction between the PSZ anr metal(s) complex(es). Moreover, as samples PSZNi2.5 and PSZCo2.5 were pyrolyzed at relatively low temperatures (300 and 500 °C), the as-obtained powders were also subjected to FTIR to evaluate their chemical changes during conversion to ceramic. To avoid air and moisture contamination, all samples were prepared inside the glove box.

Solid samples, including the above-mentioned pyrolyzed intermediates, were embedded (5 wt%) in a KBr matrix and then pressed under 5 T to have a pellet shape. For liquid samples, such as the PSZ, a drop was placed between two dried KBr commercial windows. In both cases, after this distinct preparation, the pellets were directly transferred to the spectrometer, to record the spectra in the 4000 to 400 cm^{-1} frequency range. All analyses were performed at room temperature and data was logged by OMNIC32™ Software. The obtained spectra were normalized based on the intensity of the peak related to Si-CH_3 bonds around 1250 cm^{-1}, as it is a characteristic bond within the PSZ molecule and is not affected even if submitted to reaction conditions.

3.4.2. Thermogravimetric Analysis & mass spectrometry (TGA-MS)

TGA coupled with mass spectroscopy was utilized to provide the weight variation profile and identification of gaseous species released during the polymer-to-ceramic conversion of the synthesized preceramic polymers. The utilized apparatus was a Netzsch STA 449 and an OmniStar mass spectrometer. All tests were conducted under argon atmosphere, with a heating rate of 10 °$Cmin^{-1}$ ranging from room temperature to 1000°C.

3.4.3. X-ray diffraction analysis

The crystalline phases of the pyrolyzed sample - ground as fine powders – were analyzed from XRD data obtained with a Bruker D8 Advance diffractometer. The scan was performed using the CuKα1/2 radiations, from 10 to 90° □□ with a step size of 0.02° and acquisition time of 0.9 s per step. The diffraction patterns were analyzed using the Diffrac + EVA software with the JCPDS-ICDD database and the program Fullprof [114] for the Rietveld refinements when required. Scale factor, cell parameters, Ni isotropic displacement parameter and line width parameters were refined for each phase. The profile shapes were modeled with the pseudo-Voigt function within the Thompson-Cox-Hastings formulation. After phase identification, the crystallite sizes were determined by the Scherrer equation (K = 0.94, λ = 0.15406 nm Cu K_α), in which the Full Width at Half Maximum values (FWHM, β) were calculated by peak fitting in the software Fityk [115] using the PseudoVoigt method.

$$L = K\lambda/\beta cos\theta$$

Where L is the crystallite size (nm).

3.4.4. Elemental analysis

C, as well as N, O and H contents of the thermolyzed powders, are measured by hot gas extraction techniques using a Horiba Emia-321V for carbon content and using a Horiba EMGA-830 for oxygen, nitrogen and hydrogen contents. The Si and Ni contents of the materials are determined by Inductively Coupled Plasma-Optical Emission Spectrometry (ICP-OES) using a PerkinElmer Optima 2000DV instrument.

3.4.5. Electron Microscopy

Surface morphology analyses of ceramics treated from 700 to 1000 °C were performed via Scanning Electron Microscopy (SEM) measurements at 10 kV and secondary electron topography. Their compositions were determined by Energy-Dispersive X-ray spectroscopy (EDS) employing a lower resolution SEM JEOL JSM-IT-300LV. Further observations of the nanoparticle microstructure and morphology as well as element distribution could be done using a field emission gun scanning electron microscope (FEG-SEM) 7900F from JEOL and by transmission electron microscopy (TEM) with a JEOL JEM 2100F. This microscope was also equipped with EDS from Brücker (with Esprit software) allowing the element mapping

3.4.6. Brunauer-Emmett-Teller (BET)

The Brunauer–Emmett–Teller (BET) method has been used to calculate the specific surface area of the thermolyzed sample. The pore-size distribution is derived from the desorption branches of the isotherms using the Barrett–Joyner–Halenda (BJH) method whereas the total pore volume is estimated from the amount of N_2 adsorbed at a relative pressure (P/P0) of 0.97. The data are collected using a Micrometrics ASAP 2020 apparatus by N_2 adsorption-desorption. Before adsorption measurements, samples were outgassed overnight at 150 °C in the degas port of the adsorption analyzer.

3.4.7. Electrochemical measurements

Electrochemical measurements have been carried out at room temperature using a homemade three-electrode Teflon cell connected to a potentiostat (Biologic SP-300). An

schematic representation of this setup is given in Figure 3.5. A reference hydrogen electrode (RHE) (Hydroflex purchased by Gaskatel) and a counter electrode made of glassy carbon (GC) slab is used. The working electrode ias a 5 mm GC disk. A catalytic ink is prepared by dispersing 10 mg of catalytic powder into a solution composed of 500 µL ultra-pure water (Milipore), 500 µL of isopropanol (Sigma Aldrich, 99.5%) and 100 µL Nafion (Sigma Aldrich, 5 wt.% in lower aliphatic alcohols).

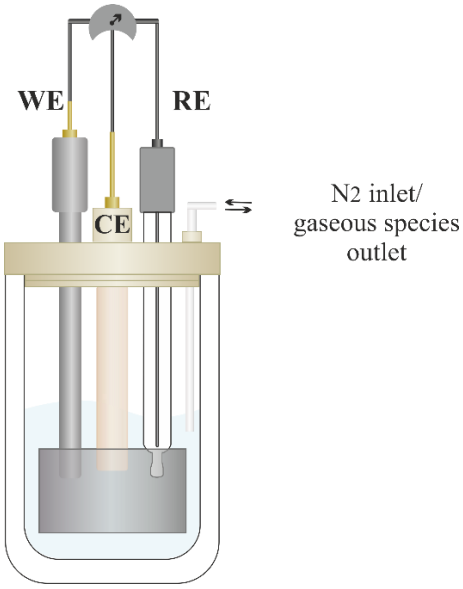

Figure 3.5. Schematic representation of the electrochemical setup utilized for AWE application essays.

The ink is homogenized by ultrasonication for 10 min. 8 µL of catalytic ink is then deposited onto the glassy carbon disc and then allowed to dry under N_2 (Air liquid, U) atmosphere at room temperature. The catalyst loading was 0.15 $mg \cdot cm^{-2}$ for all experiments. All measurements are performed in a nitrogen saturated 1 $mol \cdot L^{-1}$ KOH electrolyte (flakes, 90%, Merck to prevent iron contamination). Cyclic voltammograms and polarization curves are respectively recorded between 0.8 and 1.55 V vs. RHE and between 0.8 and 1.65 V vs. RHE. Polarization curves are recorded by applying a rotating rate of 1600 rpm to the rotating disc electrode. IR drop correction of polarization curves has been performed. For each measurement, cell resistance is determined using electrochemical impedance spectroscopy in the capacitive region and then further used for IR drop correction. For all measurements, a 10 mV amplitude was applied. Impedance spectra are acquired between 100 kHz and 10 Hz region using a potentiostat (Biologic SP-300). Acquired spectra were fitted using Biologic software (Zfit).

Stability tests are performed using the previously described mounting except for the working electrode. This latter was a nickel foam (Goodfellow) connected to the potentiostat using a gold wire. Stability tests are performed in a 1 M nitrogen-saturated KOH electrolyte. Chronopotentiometric measurements are performed by applying a constant current density of 10 $mA \cdot cm^{-2}$.

4. RESULTS AND DISCUSSION

In this chapter, the design of transition metal-modified PSZ is discussed. It was performed by the polymer-derived ceramic route aiming to obtain catalysts applicable to OER in alkaline media that requires compounds possessing high conductivity and surface area and long-life span. The focus of this approach was to generate powerful substitutes for the existing noble transition metal (TM)-based catalysts, such as RuO_2 or Pt/C. Compounds based on non-noble 3d TM are regarded as a potential alternative for this purpose due to their suitable features such as low cost, vast availability, conductivity and the stability of their oxyhydroxides - compared to their noble metal counterparts- formed during OER in alkaline media.

The use of metal nanoparticles embedded in ceramic supports is an approach of great importance to overcome problems like aggregation and removal of TM particles from the support. For these reasons, in recent years the PDC route has been regarded as a great alternative to immobilize TM nanoparticles in a ceramic matrix for catalysis. Taking that into account, distinct cobalt and nickel compounds were evaluated in this study to investigate the possibility to design the final product properties as well as determine the most promising candidate for the intended application.

Within this context, this chapter provides a fundamental approach related to the generation of engineered TM-immobilized SiCON with tailored porosity. The solvent effect was investigated to have more information of the system and the results are discussed in the first section. As different TM were employed for this goal, the second section is directed to the modification of the polysilazane Durazane 1800® (named here as PSZ) by transition metal acetates and acetylacetonates. Sequentially, a section devoted to PSZ modification by nickel and/or cobalt chlorides is provided. Finally, the last section exhibits the application results of the sample that possessed the most promising properties to be employed in AWE.

4.1. Solvent effect's in PSZ structure

The PSZ was the only silicon source employed in this study, as it is a relatively cheap and commercially available copolymer containing 20% of methyl/vinyl and 80% of methyl/hydride-substituted silazane units, which is employable for preparing SiCN ceramics whether pyrolyzed under argon or nitrogen atmosphere or to generate Si_3N_4 ceramics if treated under ammonia.

The choice of solvent was done based on several essays performed using DMF, THF and toluene. Only in DMF chemical reactions between silicon and metal precursors were achieved, which was visually observed by a fast color change in the systems as well as by characterization tools. For that reason, DMF was chosen to be the solvent for all reactions reported in this work. To isolate the solvent effects, and better compare the pure PSZ and PSZ-metal modified samples, an overnight reaction of pure PSZ in DMF was carried out.

For this procedure, PSZ was added to a 3-neck round-bottom flask inside the glovebox, further connected to the Schlenk line and then, the solvent was slowly added to it under magnetic stirring and argon flow at room temperature. This system was kept in this condition for 3 hours, heated up to 155 °C, kept overnight under this condition, cooled down and submitted to solvent extraction under reduced pressure, as discussed in the standard synthesis protocol utilized in reactions containing metal precursors described in subsection 3.2.

Regarding their visual aspect, it can be seen that at room temperature the pure PSZ is a pale yellow liquid (Figure 4.1 (left)) whilst after the overnight reaction in DMF, a dark red viscous liquid is generated (Figure 4.1 (right)), indicating the occurrence of chemical reactions between the preceramic precursor and solvent.

Figure 4.1. The physical aspect of PSZ (left) and PSZ_DMF (right).

To have a better understanding of the chemical bonds formed, pure PSZ and PSZ_DMF samples were subjected to FTIR analysis. IR spectra of these materials were normalized to the band of methyl group present in PSZ's structure, once no chemical reaction is expected to take place at this group during the synthesis. As can be seen in Figure 4.2, the PSZ studied here exhibits the expected absorption bands reported for polysilazanes [116]: 3380 cm^{-1} (νSi-NH)

coupled to 1160 cm^{-1} (δN-H), 2960 cm^{-1} and 2850 cm^{-1} (νCH_3), 2916 cm^{-1} (νCH_2), 2898 cm^{-1} (νCH), 2140 cm^{-1} (νSi-H), 3050 cm^{-1} (νC=C), 1590 cm^{-1} (δC=C), 1400 cm^{-1} (νC-H), 1250 cm^{-1} ($\delta Si\text{-}CH_3$). From 1000 to 500 cm^{-1}, absorption bands of Si-C, Si-N, C-H, and C-C bonds are observed, however, they cannot be easily assigned due to overlapping.

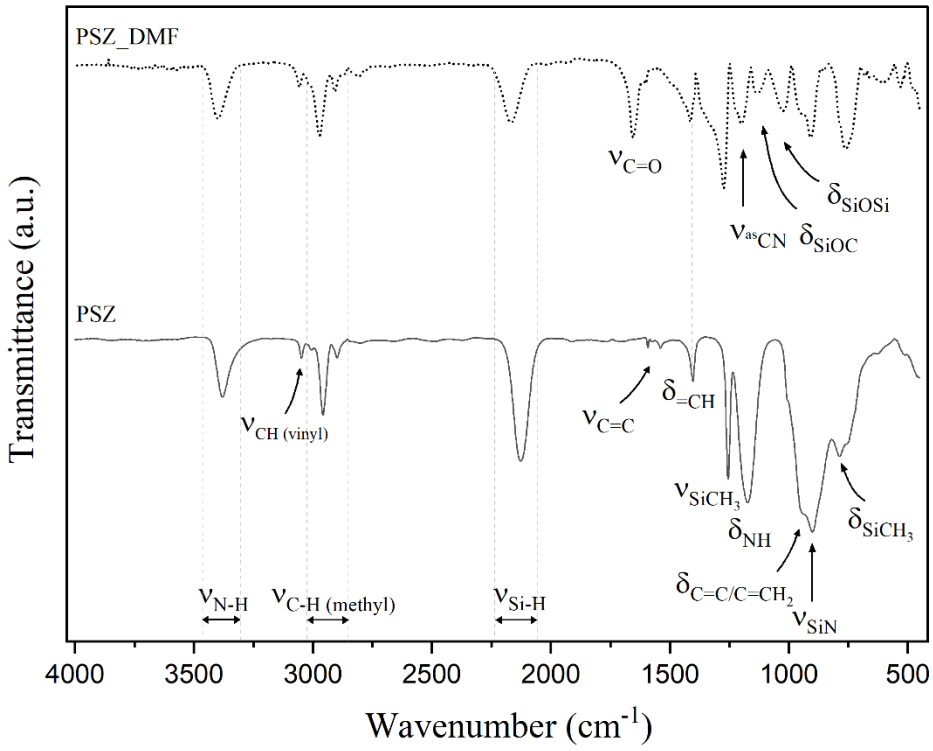

Figure 4.2. FT-IR spectra of pure PSZ compared to PSZ_DMF sample.

As for PSZ in DMF, it can be noticed that the obtained polymer, named PSZ_DMF, kept a very similar chemical structure to pure PSZ, as evidenced by νNH, $\nu CH_{(vinyl)}$, $\nu C\text{-}H_{(methyl)}$, and νSi-H. There is a great reduction in νSi-H (2140 cm^{-1}), whilst νNH (3380 cm^{-1}) seems to have slightly decreased in comparison to pure PSZ. Additionally, bands of νC=O (1658 cm^{-1}), δCH_3 (1385 cm^{-1}) and νC-N (1122 cm^{-1}) assigned to DMF are observed. Besides, it seems that Si-O-C (1110 cm^{-1} - 1085 cm^{-1}) and/or Si-O-Si (1095-1075/1055-1020 cm^{-1}) have been formed, being, therefore, an indication that DMF's oxygen could interact with PSZ. The fact that νSiH has significantly reduced suggests that dehydrogenation reactions mainly happen at this site in presence of this solvent. These new bands observed in PSZ_DMF sample confirm that the color change seen in Figure 4.1 is indeed related to the occurrence of chemical bonds after the overnight reaction.

These samples were subjected to thermogravimetric analysis coupled with a mass-spectrometer, from room temperature to 1000 °C, to have a more precise understanding of their composition changes during pyrolysis. It is well-known that the polymer-to-ceramic transformation of preceramic polymers happens through several composition changes during heat treatment under a specific atmosphere generating an inorganic and non-volatile product [117].

Three main weight losses occur in the thermogravimetric curve of PSZ as observed by three variations displayed in the chart presented in Figure 4.3. The first one starts below 200 °C due to the volatilization of low-molecular compounds and dehydrocoupling reactions of SiH/SiH and SiH/NH groups (Equations (4.1) and (4.2)), releasing dihydrogen as a byproduct. Sequentially, PSZ's crosslinking via transamination (Equations (4.3) and (4.4)) and hydrosilylation reactions (Equation (4.5)), are responsible for the mass loss starting around 220 °C.

$$\equiv SiH + HSi \equiv \rightarrow \equiv Si_2 \equiv + H_2 \quad (4.1)$$

$$\equiv SiH + \equiv SiNHSi \equiv \rightarrow Si_3N + H_2 \quad (4.2)$$

$$2 \equiv SiNHSi \equiv \rightarrow \equiv SiNH_2 + (Si)_3N \quad (4.3)$$

$$\equiv SiNH_2 + \equiv SiNHSi \equiv \rightarrow (Si)_3N + NH_3 \quad (4.4)$$

$$\equiv SiCH = CH_2 + \equiv SiH \rightarrow \equiv SiCH_2CH_2Si \equiv \& \equiv SiCH(CH_3)Si \equiv \quad (4.5)$$

From 250 °C to 500 °C, PSZ's thermal degradation is mainly promoted by radical reactions, and then, the third and last weight variation occurs from 500 to 700 °C due to radical recombination reactions. Beyond this temperature, PSZ is fully converted into ceramic and no further weight variation is observed, as also observed by Lale (2017). The gaseous species released are consistent with the expected for these reactions: dihydrogen (H_2, m/z = 2), carbon (C, m/z = 12 and 13), methane (CH_3 m/z = 15), ammonia (NH_3, m/z= 17), ammonium (NH_4, m/z = 18), CN (m/z = 26), ethene (C_2H_3, m/z = 27), ethane (C_2H_5, m/z = 29), methylamine (CH_3NH_2, m/z = 30) (depicted in Figure 4.4).

From the knowledge of this thermal behavior and PSZ_DMF's thermal degradation, it can be noticed that the overnight reaction in this solvent led to an overall diminishment in final weight loss (Figure 4.3, red lines).

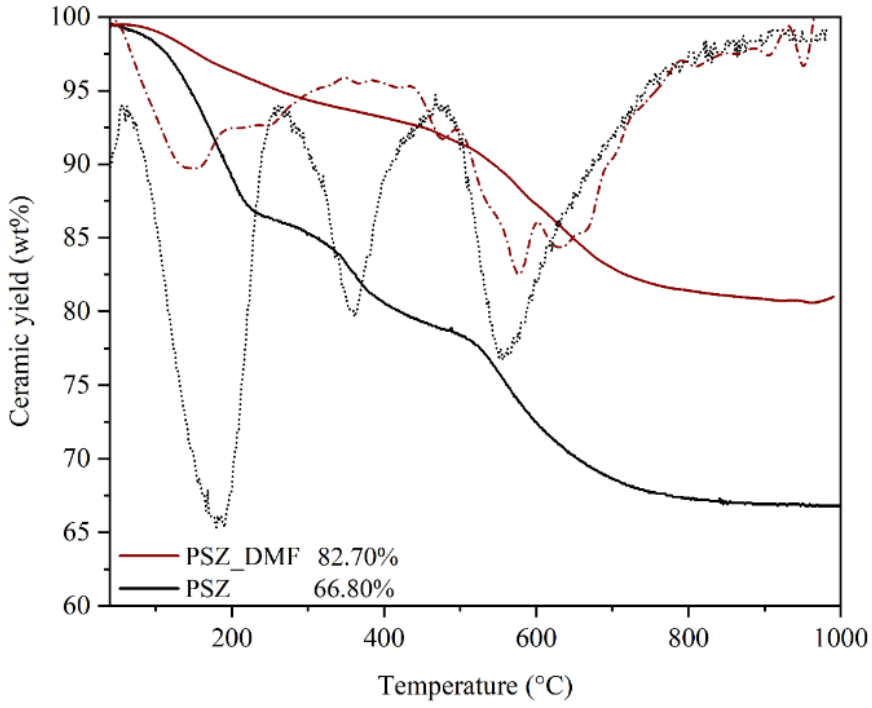

is

Figure 4.3. TG curves of the PSZ and PSZ_DMF (lines) under Argon atmosphere and their DTG (dotted lines).

From room temperature to 155 °C PSZ_DMF's weight loss should be more pronounced once the synthesis procedure employed involves a solvent extraction step, however, its complete removal was not achieved. Moreover, from 150 to 250 °C, the weight loss is not as pronounced as expected considering that PSZ normally has great volatilization of oligomers in this range. This diminishment, therefore, allows for suggesting that the higher degree of crosslinking of the PSZ_DMF sample limits the weight loss. It most probably happens due to the establishment of Si-O-Si and/or Si-O-C bridges in the structure of PSZ, as observed by their characteristic bands in IR spectra. It can thus be suggested that these bridges are formed via reduction of the amido group of DMF by Si-H groups bearing by PSZ, and that such pathway might have been facilitated as the temperature increased.

From 250 to 500 °C, an almost complete disappearance of the second weight loss due to transamination and dehydrocoupling reactions occurred and from 500 to 750 °C methane and hydrocarbon elimination are the main responsible for the weight loss seen by PSZ_DMF's DTG.

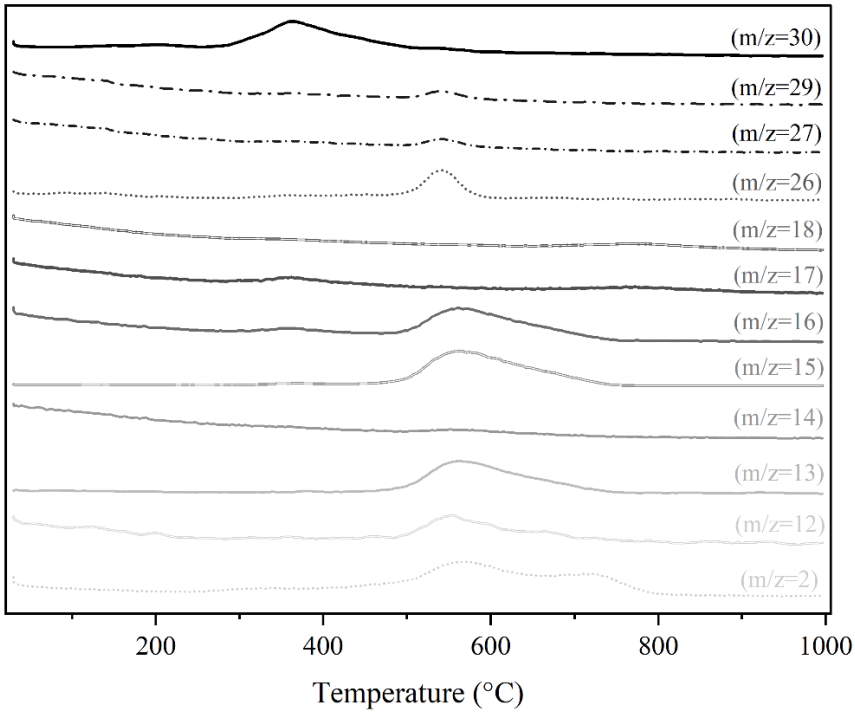

Figure 4.4. Gaseous species released during PSZ's thermal degradation.

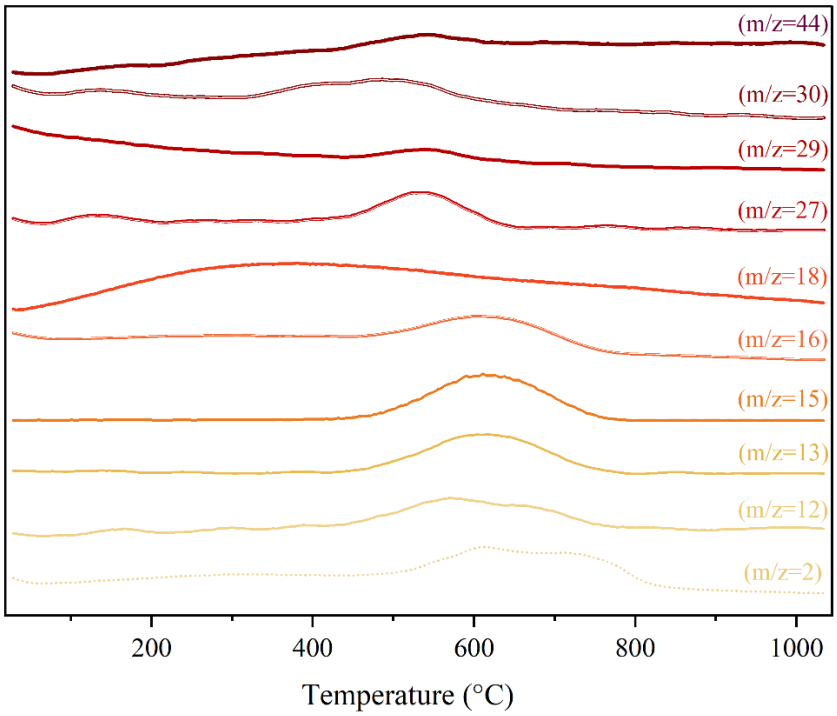

Figure 4.5. Gaseous species released during PSZ_DMF's thermal degradation.

4.2. Modification of PSZ with metal acetates and acetylacetonates

The approach presented in this subsection was focused on evaluating the effect of using different metal precursors containing sp^2 carbon, which is known for increasing materials' conductivity. For that, cobalt and nickel acetates and acetylacetonates were investigated as metal precursors.

Regarding reactions with metal precursors, before the synthesis, both TM acetates (Mac) and acetylacetonates (Macac) were dried overnight at 96 °C. Further, these metal precursors were kept under vacuum for one hour before being placed inside the glove box to extract water before each reaction. Overnight reactions between PSZ and Coac or Niac as well as PSZ with Coacac or Niacac discussed here were performed in a Si:TM ratio of 2.5. This ratio was chosen to reach a sufficiently high amount of TM nanoparticles above 35 wt%. As depicted in Figure 4.6, reactions with these metals resulted in dark viscous products noticeably containing residual solvent trapped due to the difficulty of complete solvent removal.

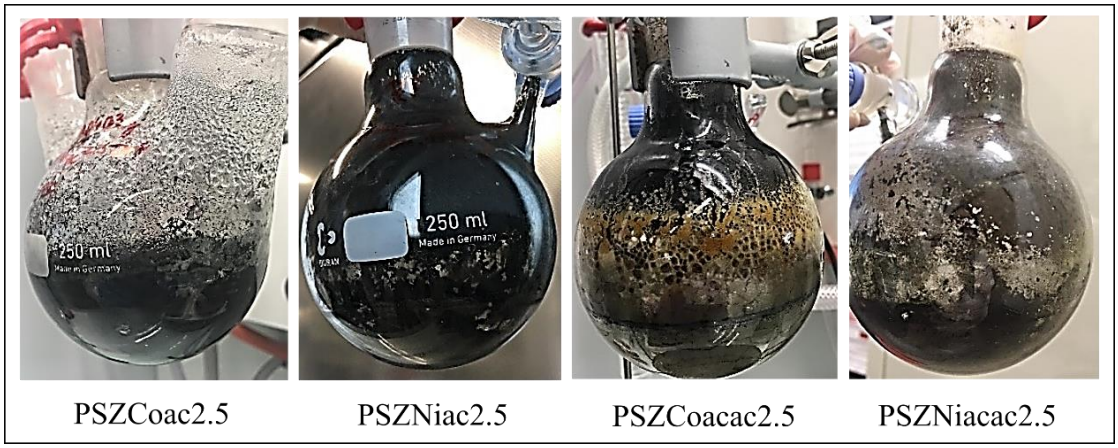

Figure 4.6. As-obtained PSZ modified with Co and Ni acetates and acetylacetonates.

As-obtained PSZCoac2.5 and PSZNiac2.5 as well as their corresponding pure metal precursors IR spectra are given in Figure 4.7 and Figure 4.8, respectively, in comparison to PSZ_DMF sample. Both PSZCoac2.5 and PSZNiac2.5 exhibit absorption bands related to νNH and νCH of vinyl from the PSZ structure, as well as bands observed in PSZ_DMF, such as C=O (1650 cm^{-1}), Si-O-C (1110 cm^{-1} - 1085 cm^{-1}) and/or Si-O-Si (1095-1075/1055-1020 cm^{-1}). The absorption bands corresponding to C=O vibration can be attributed to both the presence of DMF

and the formed Si–$OOCCH_3$ in the precursors suggesting a successful chemical reaction between the TM acetate tetrahydrate in both polymers via the silicon centers [118].

The absorption band of νSiH almost disappeared in PSZCoac2.5 and completely vanished in PSZNiac2.5. Moreover, the vibration band of vinyl groups at 3042 cm^{-1} is equally absent in both polymers, indicating hydrosilylation reactions occurrence. Concerning metal precursors', both polymers show absorption bands of the acetate group at 1560, 1415 and 1368 cm^{-1}. The broadband seen at 3500 cm^{-1} indicates the presence of hydroxyl groups, hence, confirming that hydration water molecules from Coac and Niac were not completely removed even after drying and being kept under vacuum, therefore, agreeing with the visible aspect observed during synthesis and shown in Figure 4.6.

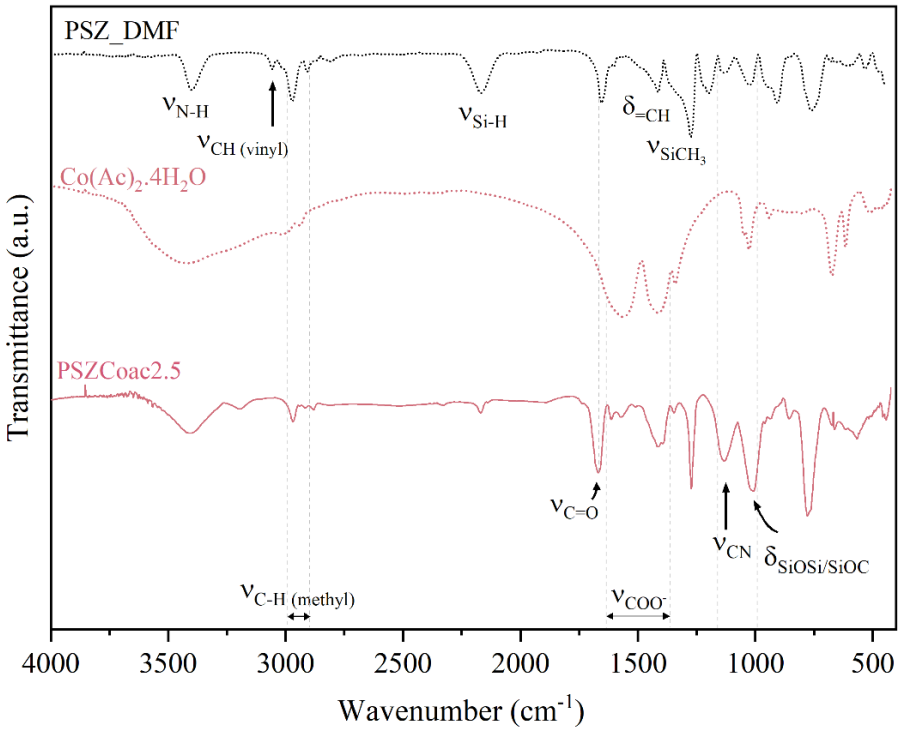

Figure 4.7. FT-IR spectra of pure Coac and PSZCoac2.5 sample in comparison to PSZ_DMF sample.

Notably, the diminishment or disappearance of the absorption band of SiH from PSZ along with the disappearance of vibration of $\nu CH_{(vinyl)}$ at 3040 cm^{-1} are effects that together indicate hydrosilylation reactions between the groups νSiH and δSi-$CH=CH_2$ occurred, most probably because Ni or Co acted as catalysts [118]. It is not evident to observe a decrease in the intensity of bands related to NH groups. Additionally, hydrolysis reactions of νSiH and νNH

should be mentioned, as it can be the reason for the formation of silanol groups (SiOH) that could condensate forming Si-O-Si. On the other hand, the presence of DMF should also be considered regarding Si-O-C and Si-O-Si formation. By employing NMR analysis it would be possible to better evaluate and conclude which compound promotes these bond formations, nevertheless, the sample reactivity did not allow a proper investigation by this technique.

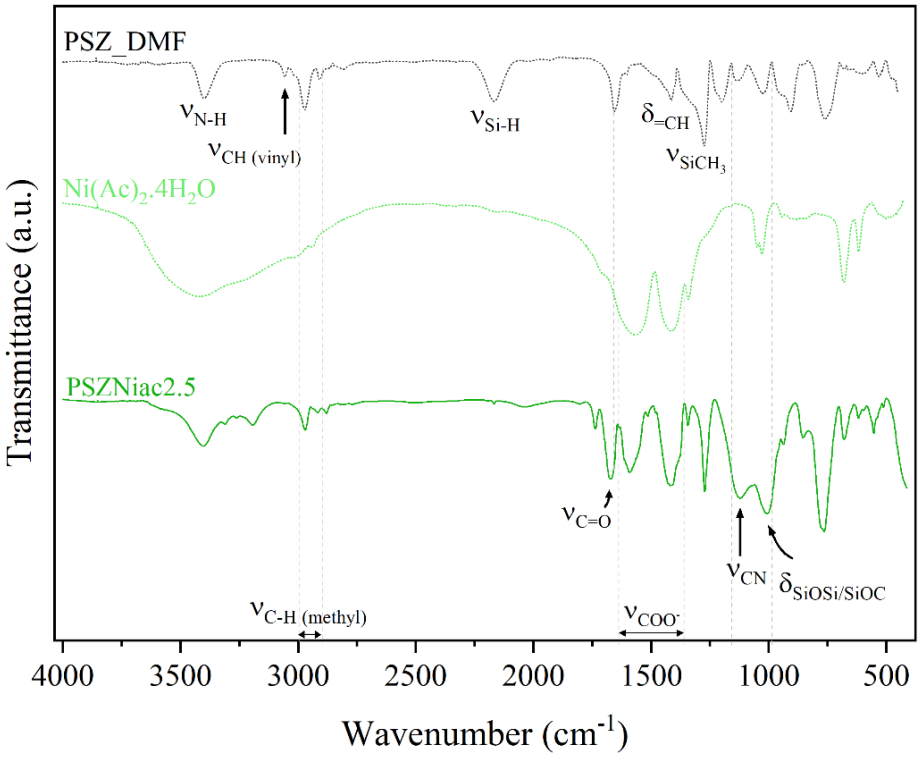

Figure 4.8. FT-IR spectra of the pure Niac and PSZNiac2.5 sample in comparison to PSZ_DMF sample.

These results are in good agreement with the findings of Wang *et al.*, (2020). The authors investigated reactions of PSZ with several metal acetates in THF, including anhydrous $Co(ac)_2$ and $Co(ac)_2.4H_2O$. According to what they reported, hydrosilylation reactions led to carbosilane bonds (-Si-C-C-Si-) formation, as demonstrated in equation (4.6), as well as an associated evolution of H_2 (equation (4.7)) and NH_3 (equation (4.8)). Furthermore, crosslinked Si-O-Si bonds were also generated, according to the reaction exposed in equation (4.9).

$$\equiv SiH + CH_2 = CH - Si \equiv \rightarrow \equiv Si - CH_2 - CH_2 - Si \equiv \quad (4.6)$$

$$\equiv Si - H + H_2O \rightarrow \equiv Si - OH + H_2 \quad (4.7)$$

$$-SiH_2 - NH - + H_2O \rightarrow -SiH_2 - OH + NH_3 \quad (4.8)$$

$$\equiv SiH_2 - OH + \equiv SiH_2 - OH \rightarrow -SiH_2 - O - SiH_2 \equiv + H_2O \quad (4.9)$$

More recently, Wang *et al.*, (2021) published a study in which Niac was used to react with PSZ and PHPS in THF to generate silicon oxycarbonitride ceramics. The authors also observed a similar decrease in νSiH band and pointed out that absorption bands of C=O vibration can be attributed to the formation of Si-$OOCCH_3$ in both precursors evaluated. Although in the present thesis, the appearance of C=O vibration cannot be ascribed solely to the formation of Si-$OOCCH_3$, as DMF also possesses this group on its structure, it is probably one of the bonds formed after PSZ's dehydrocoupling reactions at the SiH site. A possible reaction mechanism of PSZ and Niac leading to the formation of Ni nanoparticles at the polymer level was even proposed (Figure 4.9).

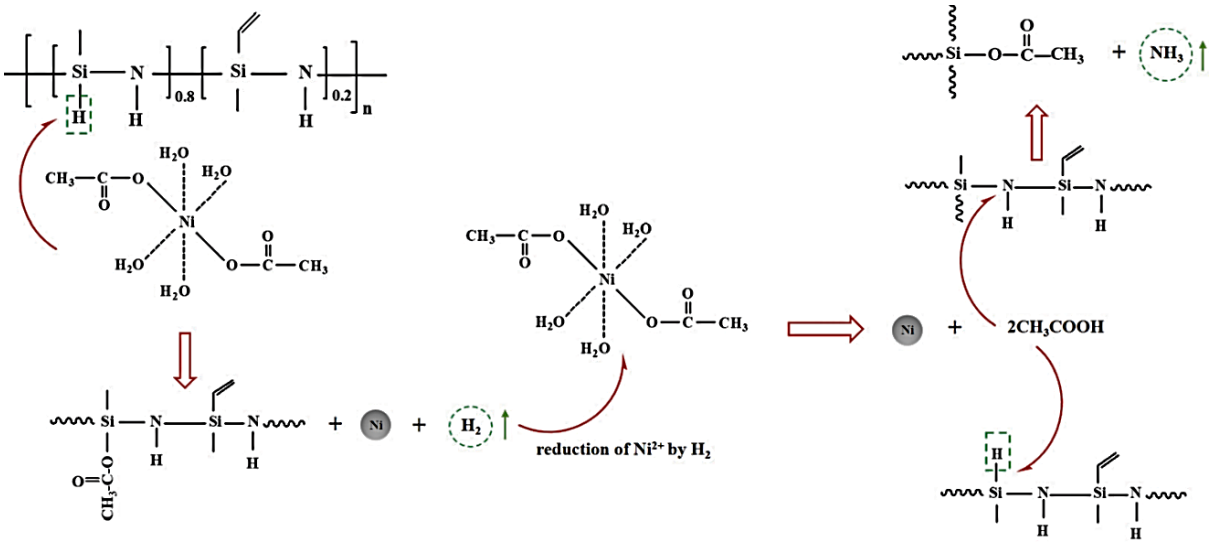

Figure 4.9. Possible mechanisms of reaction between PSZ and $Ni(Ac)_2.4H_2O$ forming metallic nickel nanoparticles [119].

With regards to PSZCoacac2.5 (Figure 4.11) and PSZNiacac2.5 (Figure 4.12), the first observation that can be mentioned is the disappearance of the band attributed to Si-H bonds suggesting that there is at least a reaction between Macac and PSZ. As with regards to the reaction mechanism between PSZ and Macac, it should involve the condensation reaction of the Si–H groups from PSZ and the M–O groups from Macac (Figure 4.10), also previously reported in a research article on PSZ modification with metal acetylacetonates [120].

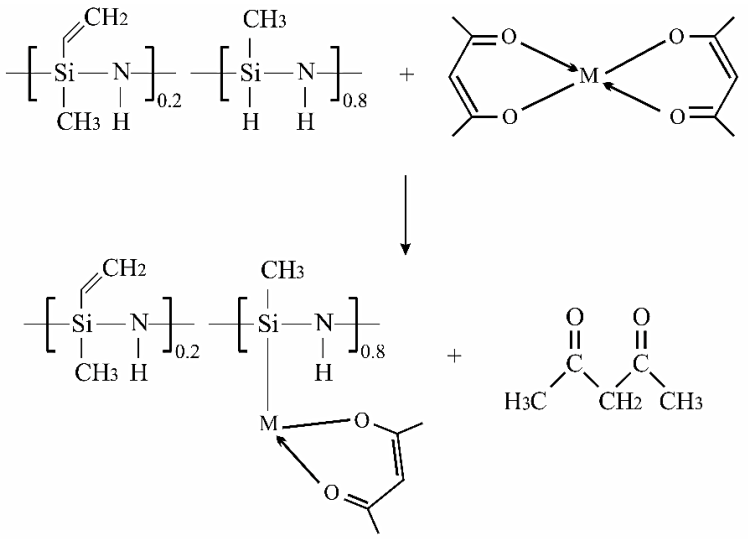

Figure 4.10. Scheme of possible reaction between PSZ and $M(acac)_2$, adapted from [120].

This suggestion was based on a study reporting the reaction of polycarbosilane (PCS) with $Zracac_4$. It proceeds by the condensation reaction of the Si-H bonds in PCS and the ligands of $Zracac_4$ accompanied by the evolution of acetylacetone resulting in a molecular weight increase based on the formation of Si-Zr bonds [120]. However, the steric hindrance was found to be a difficulty for all Macac ligands to execute the condensation reaction. This effect is observed here by the finding that characteristic absorption peaks at 1520 cm^{-1} (C=C stretching) and 1575 cm^{-1} (C=O stretching) derived from ligands of Macac remaining in the spectra of PSZCoacac2.5 (Figure 4.11) and PSZNiacac2.5 (Figure 4.12). The signature of DMF is observed through the bands of νC=O (1658 cm^{-1}), δCH_3 (1385 cm^{-1}) and νC-N (1122 cm^{-1}). Bands related to SiOC (1110 cm^{-1} - 1085 cm^{-1}) and/or Si-O-Si (1095-1075/1055-1020 cm^{-1}) units are also identified.

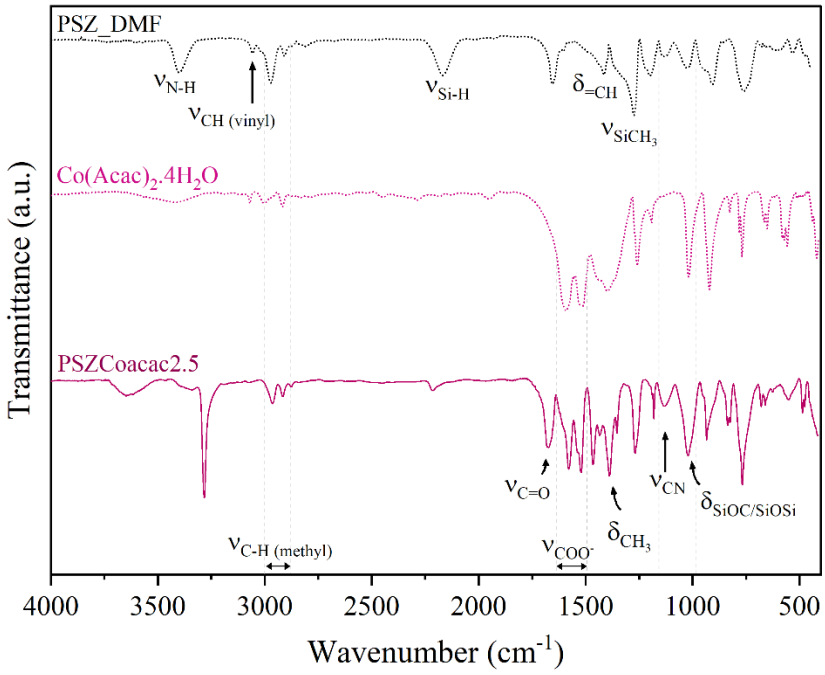

Figure 4.11. FT-IR spectra of pure Coacac and PSZCoacac2.5 sample in comparison to PSZ_DMF sample.

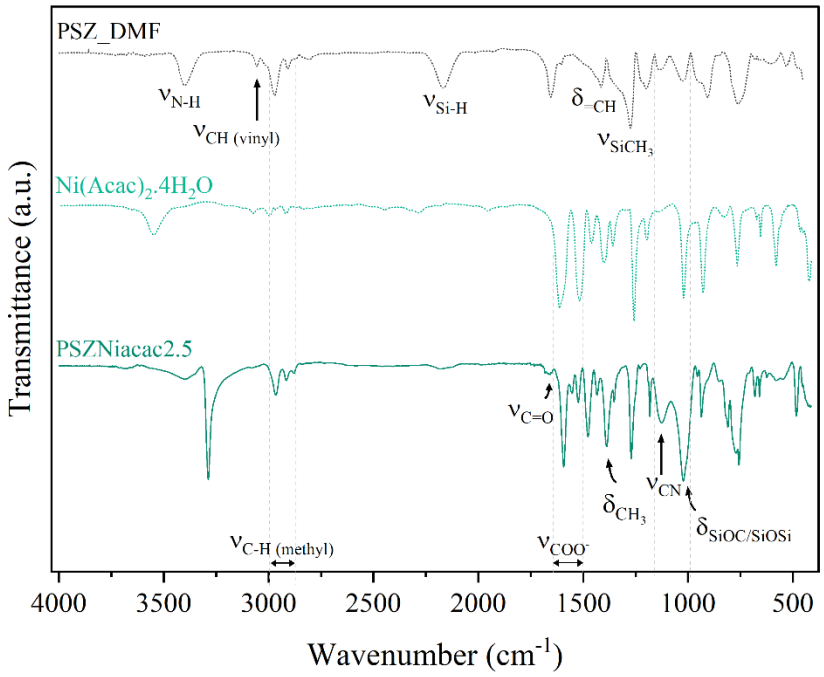

Figure 4.12. FT-IR spectra of pure Niacac and PSZNiacac2.5 sample in comparison to PSZ_DMF sample.

The thermal behavior of metal acetate- and metal acetylacetonate-modified PSZ in DMF was evaluated to compare and verify the effects of their chemical structures on the whole system and the results are discussed in the next subsection.

4.2.1. Thermal behavior investigation of metal acetate- and metal acetylacetonate-modified PSZ

PSZCoac2.5 (Figure 4.13) exhibits a significant weight loss of almost 30% until 300 °C, which is not in line with those reported in the literature [120]. This disparity is mainly associated with DMF and low-weight molecules' volatilization, as observed by the release of carbon (C, m/z = 12 and 13), methane (CH_3 m/z = 15), Oxygen (O, m/z= 16), CN or C_2H_2 (m/z = 26), ethene (C_2H_3, m/z = 27), carbon monoxide (CO or C_2H_4, m/z= 28), ethane or formyl radical (C_2H_5, CHO m/z = 29), methylamine (CH_2NH_2, m/z = 30) and carbon dioxide (CO_2, m/z = 44) (Figure 4.14). The second variation from 250 to ~650 °C, presents a crescent evolution of H_2 (m/z = 2), oxygen (m/z= 16), hydroxyl or ammonia (m/z= 17), and water or ammonium (m/z = 18), corroborating with the hypothesis that hydrosilylation reactions led to carbosilane bonds. Moreover, H_2 and NH_3 release can also be attributed to concomitant PSZ's dehydrocoupling, thermal crosslinking, and transamination reactions. The last variation is solely related to H_2 and ends at around 900 °C leading to a final ceramic yield of 62.27%.

As for PSZCoacac2.5 (Figure 4.15), the first weight loss is around 15%, most probably because the sample is more crosslinked than PSZCoac2.5, which is also reflected by the greater ceramic yield. In this case, DMF and low-weight molecules' volatilization start slightly shifted (~150 to 300 °C) (Figure 4.16), being more pronounced above 200 °C. The second variation, in the region from 400 to 800 °C, is mostly associated with H_2 (m/z = 2), carbon (m/z = 13), methane (CH_3 m/z = 15), Oxygen (O, m/z= 16), CN or C_2H_2 (m/z = 26), ethene (C_2H_3, m/z = 27), (C_2H_4 or CO, m/z= 28) and methylamine (CH_2NH_2, m/z = 30). Even though acetylacetonate evolution was not observed, the release of these species might have enabled the condensation of Si and Metal.

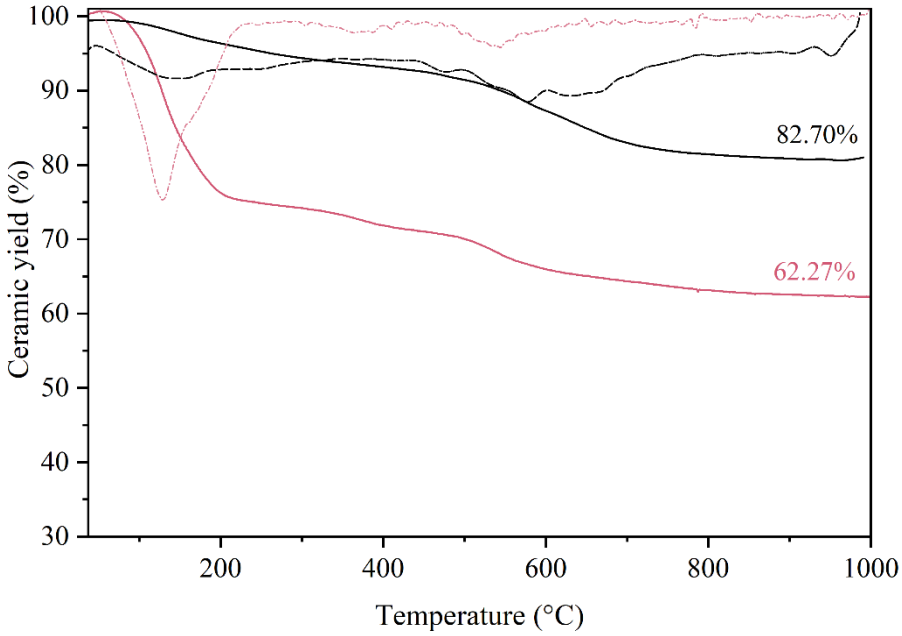

Figure 4.13. TG and DTG analysis of PSZCoac2.5 in comparison to PSZ_DMF sample (under argon atmosphere).

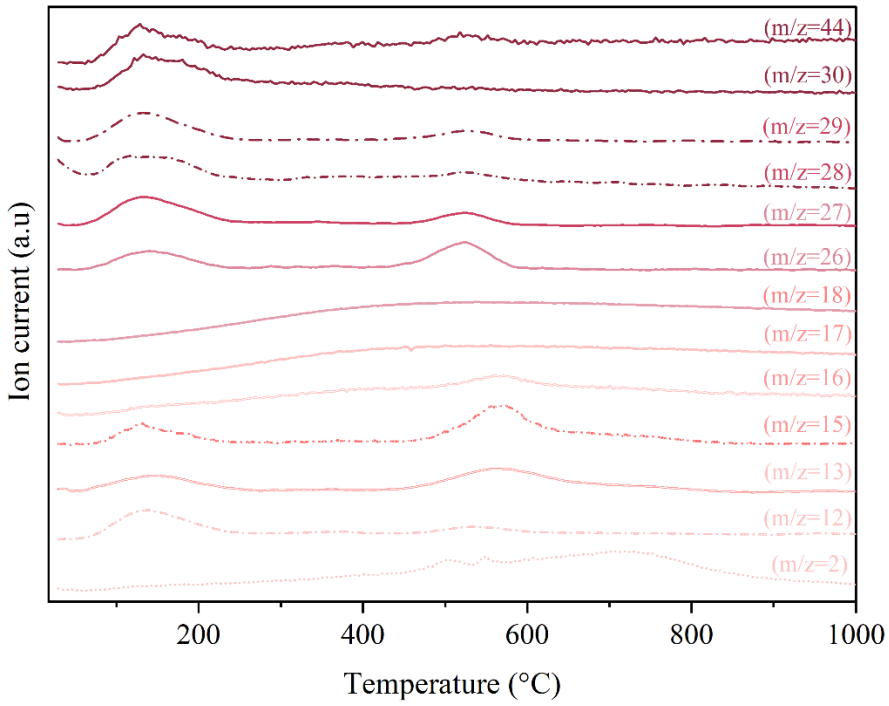

Figure 4.14. Mass spectrum of PSZCoac2.5 treated under argon atmosphere.

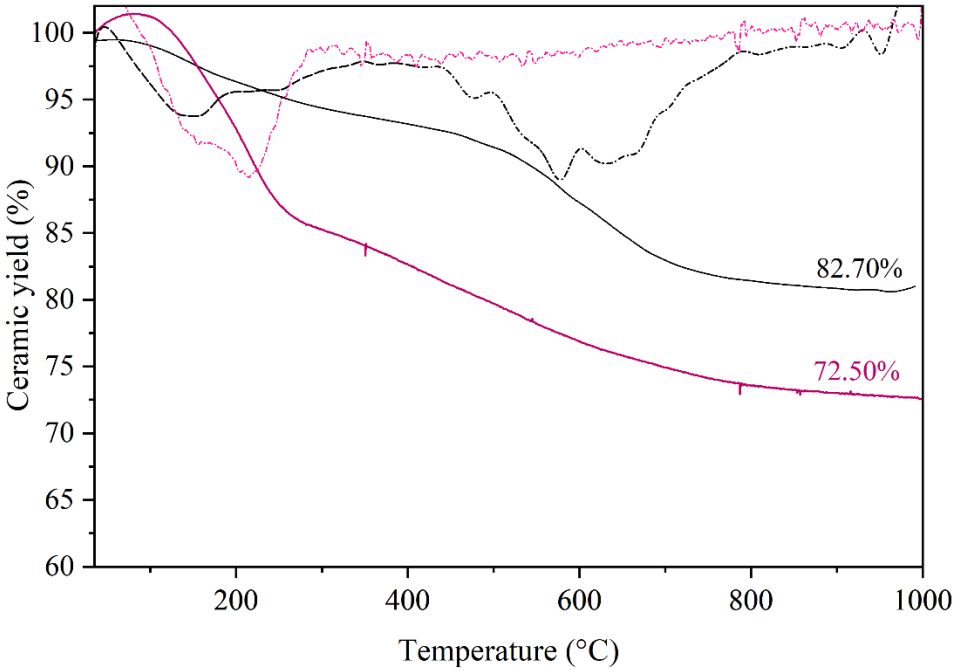

Figure 4.15. TG and DTG analysis of PSZCoacac2.5 in comparison to PSZ_DMF sample (under argon atmosphere).

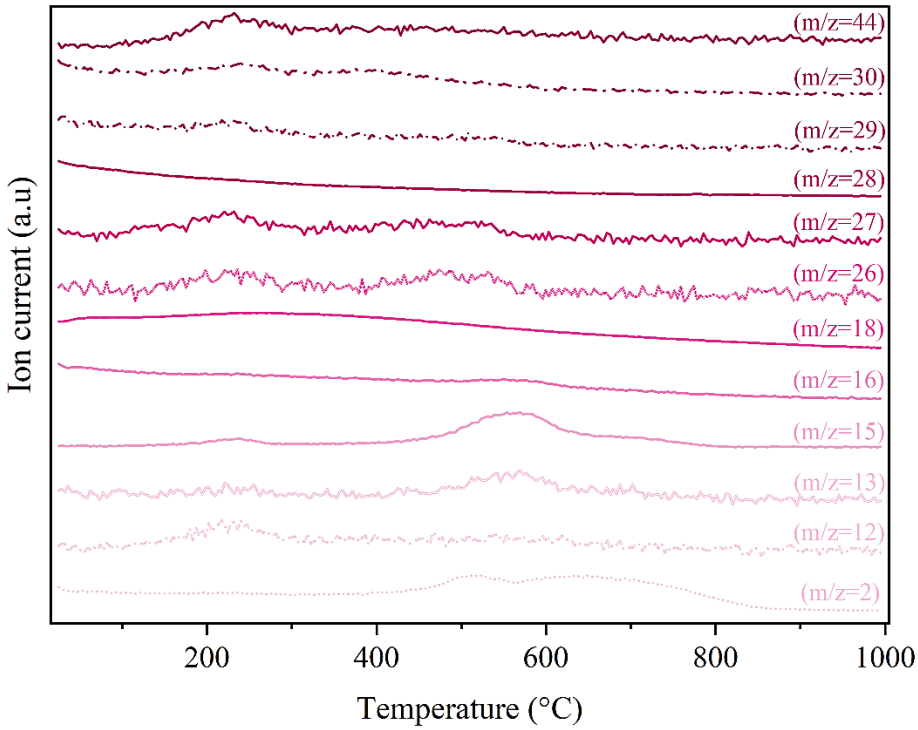

Figure 4.16. Mass spectrum of PSZCoacac2.5 treated under argon atmosphere.

Interestingly, the PSZNiac2.5 sample exhibits a distinct thermal behavior in comparison to PSZCoac2.5, which is firstly visible by the three weight losses below ~550 °C shown in TG and DTG curves in Figure 4.17.

For instance, the release of CO or C_2H_4 (m/z= 28) is reduced (Figure 4.18). Carbon dioxide (CO_2, m/z = 44) seems to become to be released only around 300 °C. Furthermore, dihydrogen (H_2, m/z = 2), carbon (C, m/z = 12 and 13), methane (CH_3 m/z = 15), oxygen (O, m/z= 16), CN or C_2H_2, (m/z = 26), ethene (C_2H_3, m/z = 27), carbon monoxide (CO or C_2H_4, m/z= 28), ethane or formyl radical (C_2H_5, CHO m/z = 29) and methylamine (CH_2NH_2, m/z = 30) release has happened at higher temperatures. Likewise, the PSZNiacac2.5 sample (Figure 4.19) did not follow PSZCoacac2.5's trend, exhibiting a first weight loss of ~30% until 150 °C, a second one from ~150 to 250 °C not that evident to visualize in the mass spectrum and the third one from 250 °C to 800 °C which is majorly associated with dihydrogen and methane release (Figure 4.20).

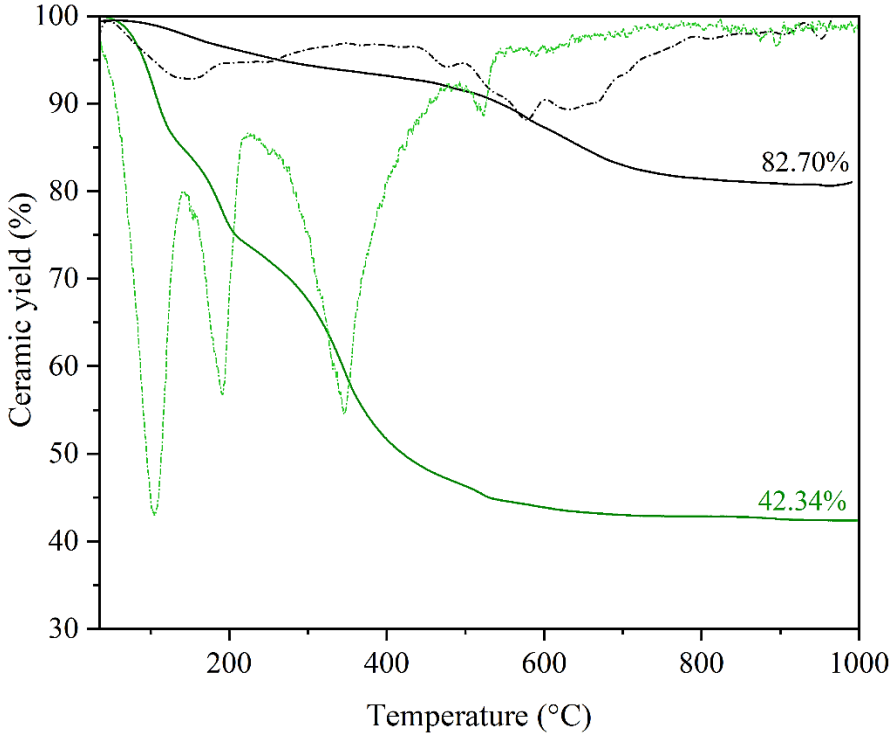

Figure 4.17. TG and DTG analysis of PSZNiac2.5 in comparison to PSZ_DMF sample (under argon atmosphere).

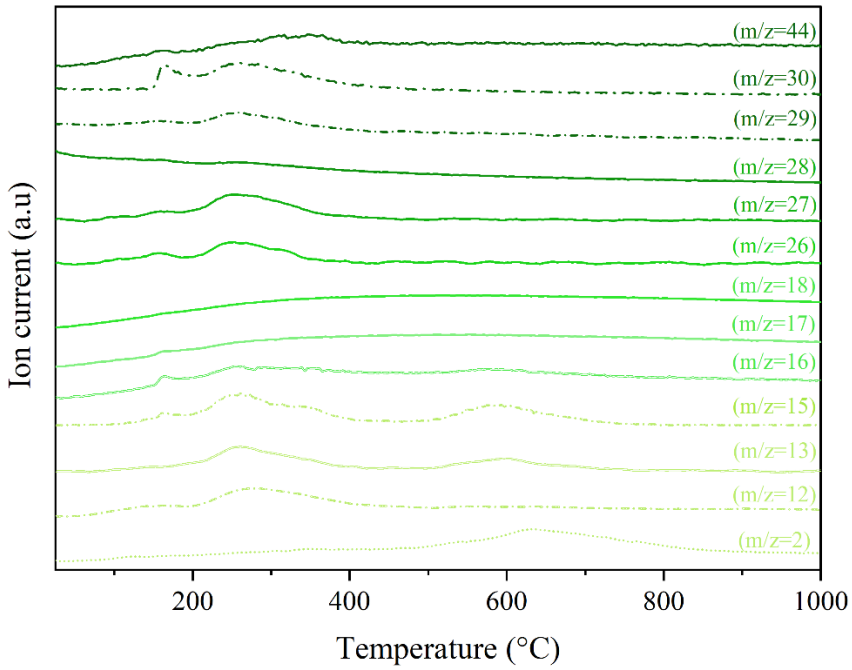

Figure 4.18. Mass spectrum of PSZNiac2.5 treated under argon atmosphere.

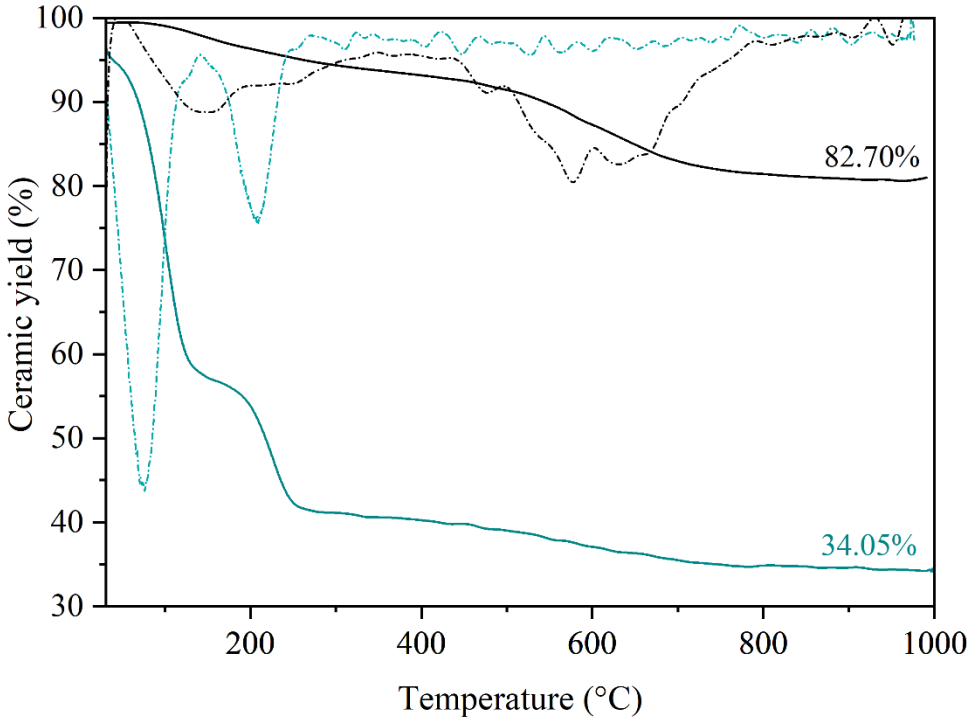

Figure 4.19. TG and DTG analysis of PSZNiacac2.5 in comparison to PSZ_DMF sample (under argon atmosphere).

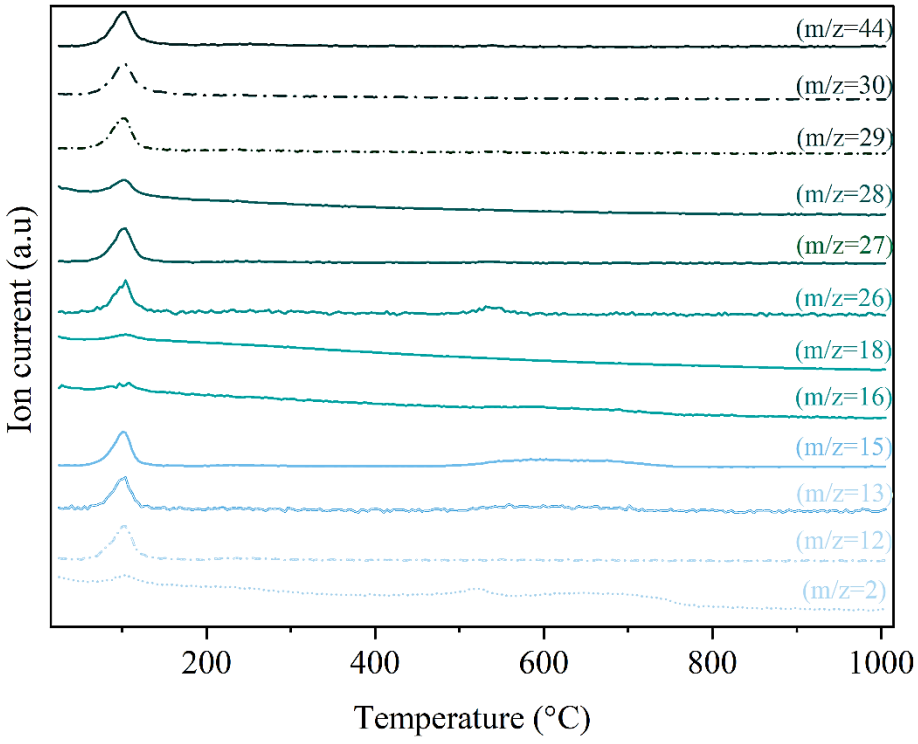

Figure 4.20. Mass spectrum of PSZNiacac2.5 treated under argon atmosphere.

In both cases, it can be noted that the presence of metal precursor has altered the thermal behavior in comparison to the observed for PSZ_DMF. Additionally, the type of metal precursor demonstrated to strongly change the thermal conversion into ceramic.

As-obtained polymers were pyrolyzed at 700, 800 and 1000 °C under an argon atmosphere and further characterized by XRD to observe their crystallization patterns which are discussed below.

4.2.2. Ceramics characterization from 700 to 1000 °C

This subsection has the focus of attention directed to changes in metal precursor, pyrolysis temperature and their effects on obtained ceramics. XRD patterns of PSZ modified by cobalt acetate at 700, 800 and 1000 °C are given in Figure 4.21.

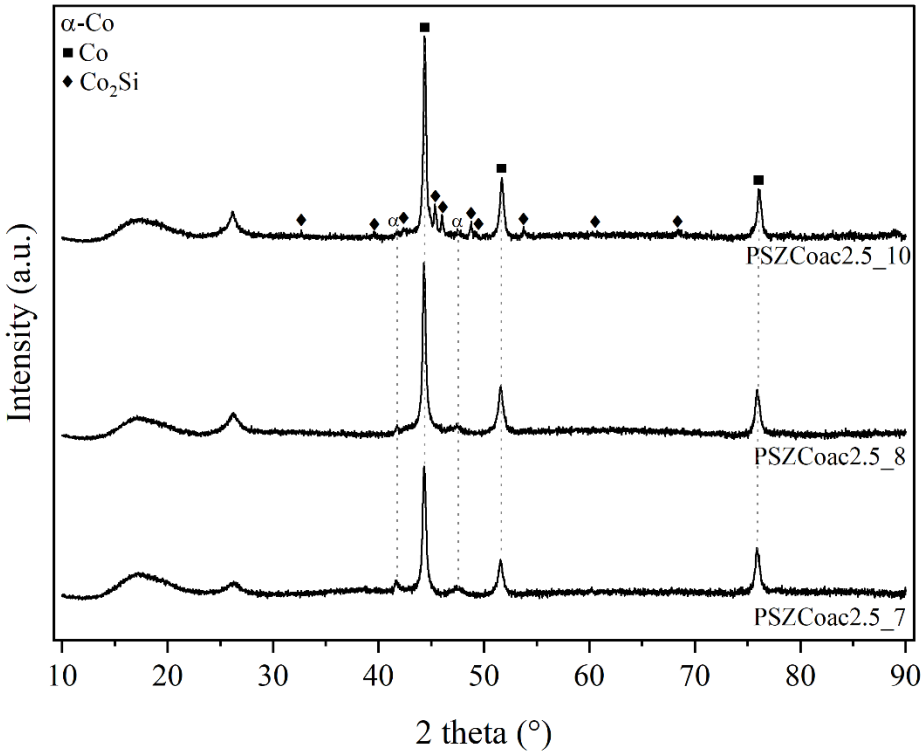

Figure 4.21. XRD pattern of PSZCoac2.5 pyrolyzed at 700ºC (PSZCoac2.5_7), 800ºC (PSZCoac2.5_8) and 1000ºC (PSZCoac2.5_10) under argon atmosphere.

The addition of Co in PSZ to form PSZCoac2.5 leads, after pyrolysis at 700 °C in flowing argon, to the main identification of a β (fcc)-Co phase (space group Fm-3m, lattice constant a = 0.35447 nm, ICDD No. 00-015-0806) in the XRD pattern, as confirmed by the indexation of the peaks at 2θ = 44.37°, 51.59° and 76.08° to (111), (200) and (220) planes, respectively [121].

In addition, it can be observed the emergence of two poorly intense XRD peaks at 2θ = 41.9° (100) and 47.6° (101), which positions are related to the diffraction of the α (hcp)-Co phase (space group P63/mmc, lattice constants a = 0.25071 nm, c = 0.408686 nm, ICDD 04-001-3273) [121]. It is well known that at normal conditions, bulk cobalt crystallizes in two phases: hexagonal closed packing (hcp, α) and face-centered cubic (fcc, β) [122]. The striking difference between these two phases is due to atoms' stacking, i.e., in β-Co, it is ABCABC while in α-Co, it is ABABAB [123].

After pyrolysis at 800 °C, the phase composition and crystallinity of the samples remained quite stable, whilst when the temperature rose to 1000 °C a growth of a Co_2Si phase (ICDD 04-003-2126) was induced and the peaks related to α-Co disappeared. The identification of the Co_2Si phase (peaks at 45.2°, 45.9°, 48.7° and 53.7°) indicates that the Si center reacted further with a CoSi phase, possibly identified through the weak and diffuse peak at 2θ = 25.4 (even though it could correspond to free carbon (002)) and 46.9° after pyrolysis to 700 and 800 °C. Moreover, it should be pointed out that CoSi is a metastable phase tending to further react with Si to form the $CoSi_2$ phase [124].

The effect of nickel on the structure of samples derived from PSZNiac2.5 was also investigated by a thermal treatment under the same conditions applied for PSZCoac2.5 and its XRD patterns are presented in Figure 4.22. It can be seen that XRD diffractograms obtained for the three temperatures evaluated show quite similar structures.

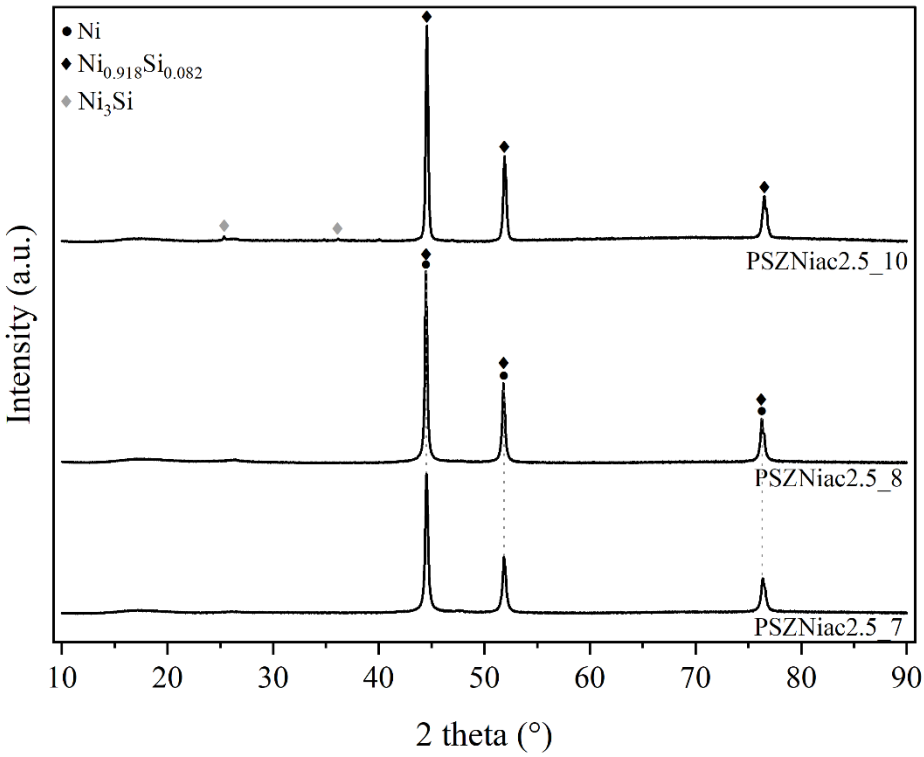

Figure 4.22. XRD pattern of PSZNiac2.5 pyrolyzed at 700ºC (PSZNiac2.5_7), 800ºC (PSZNiac2.5_8) and 1000ºC (PSZNiac2.5_10) under argon atmosphere.

The heat treatment of PSZNiac2.5 at 700 °C resulted in the formation of nickel crystals (ICDD 00-004-0850) based on the identification of three characteristic diffraction peaks for pure nickel at 2θ = 44.48, 51.83 and 76.35°. These peaks correspond to the indexed (111), (200), and (220) lattice planes of the stable face-centered cubic (fcc) structure of Ni, respectively. This phase composition was characteristic of the evolving system from 700 to 1000 °C. This means that samples prepared from PSZNiac2.5 represent Ni nanoparticles distributed in an amorphous Si-C-O-N matrix. However, at the highest temperature (1000 °C), new weak peaks could be identified. It can be suggested that they correspond to nickel silicide (Ni_3Si, file No. 01-089-5155) in the cubic crystal form at 2θ = 25.35° (100) and 36.17° (110). Prior reports have also obtained similar results by pyrolyzing $Ni(ac)_2$-modified PSZ under argon atmosphere at 700, 900 and 1100 °C [105,119].

According to the results provided by the authors, the metallic nickel phase is formed even at 700 °C when $Ni(ac)_2.4H_2O$ was reacted with PSZ, whereas, by employing PHPS, the resulting material exhibits an amorphous structure. In addition, Ni_2Si, SiC and C phases were observed in the temperature range investigated. Based on these and other results, it was concluded that Niac initially reacts with PSZ by SiH groups, resulting in acetosilyl groups

(CH_3COO-Si-) and H_2 gas release as well as an *in situ* formation of Ni nanoparticles, which is ascribed to the electron transfer from negatively charged hydrogen in -Si-H to Ni^{2+} of Niac. Due to that, the reduction of Ni^{2+} gives rise to metallic nickel nanoparticles along with H_2 evolution and formation of acetic acid. Therefrom, the latter reacts with SiH and Si-NH-Si groups evolving H_2 and NH_3 gases. Such reaction path is in good agreement with their similar study employing trans-[bis(2-aminoetanol-N,O)diacetato-nickel(II)] as the metal precursor to react with PSZ, which formed a nanoporous Ni/SiCN(O) system also having nickel nanoparticles *in situ* generated.

Similar to what was observed in PSZCoac2.5 treated at 700 and 800 °C (Figure 4.23), both β (fcc)-Co phase (ICDD No. 00-015-0806) and α (hcp)-Co phase (ICDD 04-001-3273) [121] are seen in PSZCoacac2.5 [121]. As for PSZNiacac2.5 (Figure 4.24), the XRD diffractograms obtained only exhibit the stable face-centered cubic (fcc) structure of nickel crystals (ICDD 00-004-0850) at 2θ = 44.48, 51.83 and 76.35° and in the lowest temperature (700 °C).

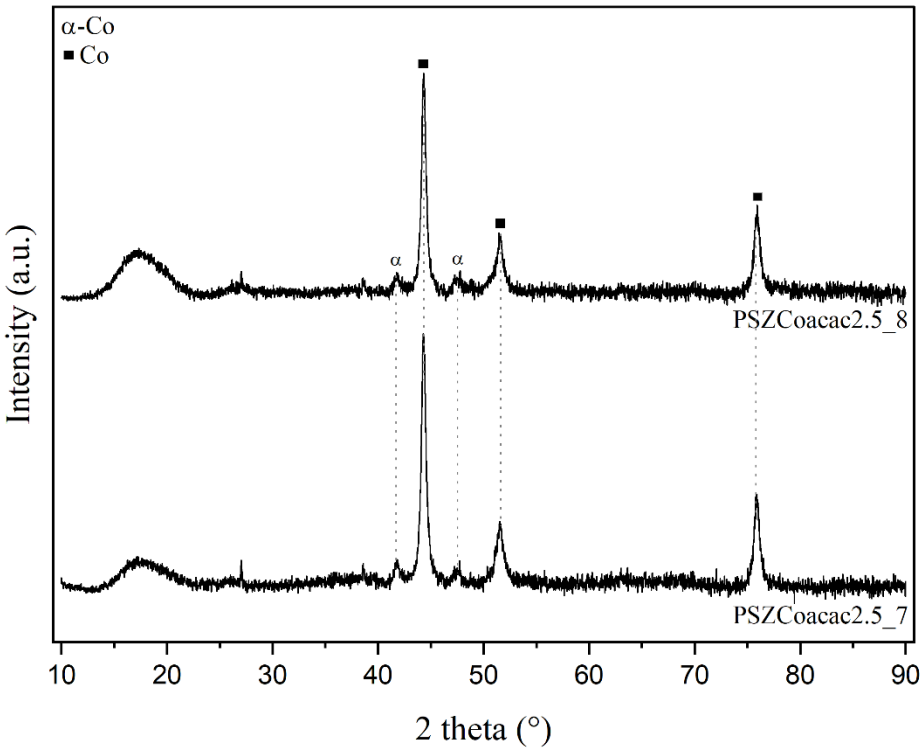

Figure 4.23. XRD pattern of PSZCoacac2.5 pyrolyzed at 700 °C (PSZCoacac2.5_7) and 800 °C (PSZCoacac2.5_8) under argon atmosphere.

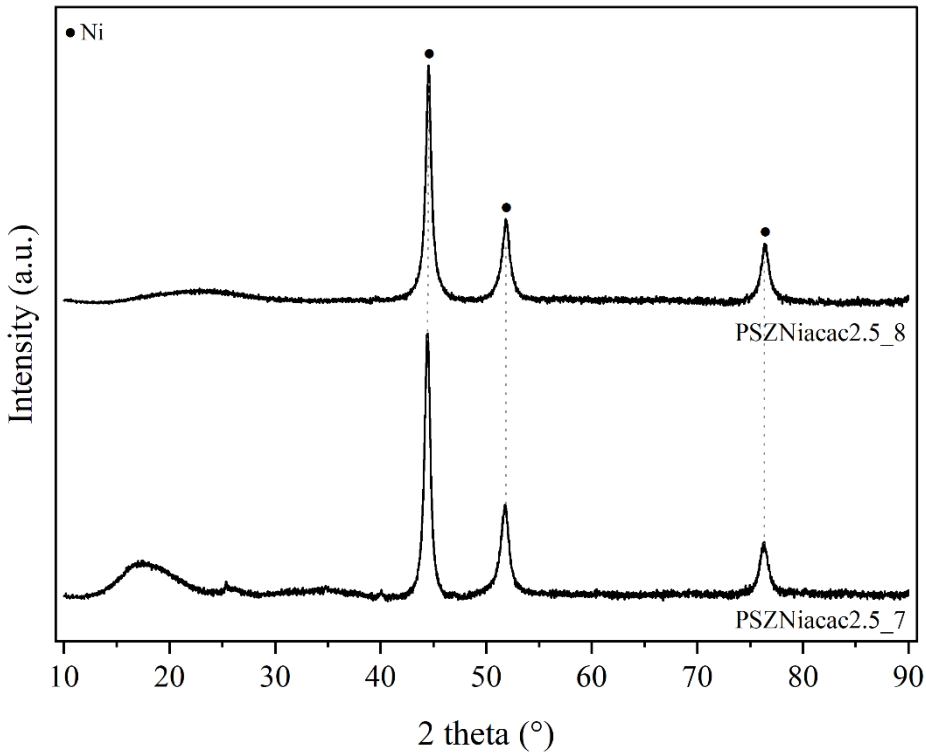

Figure 4.24. XRD pattern of PSZNiaacc2.5 pyrolyzed at 700ºC (PSZNiacac2.5_7) and 800ºC (PSZNiacac2.5_8) under argon atmosphere.

Because the modification of PSZ with metal acetate or acetylacetonate has the complication of releasing several species that are not of interest for an in-depth investigation of the chemical reactions occurring, this study was directed to the investigation of PSZ's modification employing metal chloride precursors. This approach is detailed in the following section.

4.3. Modification of PSZ with metal chlorides and their amino complexes

This section is devoted to the description of the *in situ* formation of metallic Ni nanocrystallites within the PDC matrix monitored by using a complete set of characterization techniques including infrared spectroscopy, thermogravimetric analysis (TGA), elemental analysis, powder X-ray diffraction (XRD), and transmission electron microscopy (TEM) observation. This approach was focused on the use of nickel and cobalt chlorides aiming to restrict chemical interactions between the precursors as much as possible, which could not be achieved with the previous metals utilized.

4.3.1. Modification of polysilazane with Co and Ni chlorides

Precursor preparation occurred also in DMF, which was used for mixing PSZ containing highly reactive Si-H and N-H bonds with TM chloride (TM = Co, Ni) while promoting PSZ crosslinking to form a solid compound. The synthesis has been carried out with predetermined atomic Si:TM ratio from 1 to 10 to achieve various TM content in the final compound for the targeted reaction. The mixing of both metal precursors reacting with this polysilazane was also investigated to verify if the conductivity would increase generating a bimetallic-containing ceramic with features comparable to those of products generated by utilizing only one metal precursor. However, we will mainly consider Ni-containing precursors with a ratio Si:Ni of 2.5; it is labeled PSZNi2.5DMF, to keep the investigation using the same Si:TM ratio discussed in the previous section. Figure 4.27 illustrates the different reaction steps for this sample based on the evolution of solution color which changed from orange to dark green in a few minutes after adding PSZ to $NiCl_2$, ending owing a general blackish tone with some blue highlights after DMF extraction.

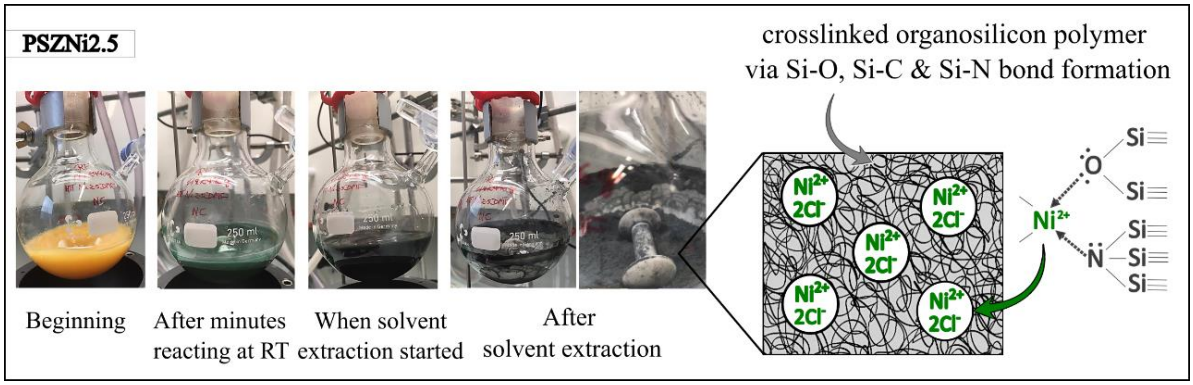

Figure 4.25. PSZNi2.5 evolution and proposed reaction mechanism.

To precise the contents of elements present in as-synthesized PSZNi2.5 and thermolyzed PSZNi2.5_5 powders, elemental analysis was conducted (Table 4.1), allowing the determination of the respective following empirical formulas: $Si_{1.0}C_{3.6}N_{1.5}O_{1.2}H_{9.3}Ni_{0.4}Cl_{0.8}$ and $Si_{1.0}C_{2.5}N_{0.4}O_{1.4}H_{4.4}Ni_{1.1}$ in comparison to that of PSZ ($Si_{1.0}C_{1.5}N_{1.1}O_{0.0}H_{5.6}$). From these empirical formulas, it can be seen that the atomic ratio between Cl:Ni calculated (0.8:0.4) for the polymer PSZNi2.5 is identical to that of $NiCl_2$. This equality together with the Si:Ni ratio (2.5) erroneously suggests that no significant release of chlorine- and silicon-containing species occurred during reactive blending when, indeed, relatively high incorporation of oxygen atoms into PSZNi2.5 backbone has happened, as can be seen by comparison with PSZ. Once both precursor synthesis and thermolysis were carried out under an argon atmosphere, this oxygen incorporation can be correlated to the use of DMF.

Table 4.1. Elemental composition (wt%) of PSZNi2.5 and PSZNi2.5_5 in comparison to PSZ.

Sample	C	H	N	O	Ni	Si	Cl*
PSZ	27.3	8.3	22.7	0.4	-	41.3	-
PSZNi2.5	24.1	5.3	11.8	10.8	14.8	15.8	17.4
PSZNi2.5_5	19.3	2.9	3.6	14.7	41.3	18.2	-

*Omitted in pyrolyzed sample (PSZNi2.5_5 due to its very low content of 0.5 wt%.

To explain the incorporation of oxygen in the system, it is suggested that $NiCl_2$ catalyzes the reduction of DMF's amido group by the Si-H group from PSZ, allowing the bonding of oxygen from the carbonyl group as well as providing amines and Si-O units to the resulting sample. This assumption is in good corroboration with the thermal reduction of amides to amines by hydrosilanes with transition metals acting as catalysts previously reported by Arias-Ugarte *et al.*, (2012). In addition, the greater content of nitrogen, carbon, oxygen and hydrogen

observed in the empirical formula of PSZNi2.5 compared to that of PSZ indicates the presence of trapped residual DMF ($C_3H_7O_2N$).

To have more information regarding the precursor interaction, the sample were characterized by FTIR. Noticeably, the spectrum of PSZNi2.5 (Figure 4.26) exhibits one intense band attributed to $NiCl_2$ at 1612 cm^{-1} along with the presence of three characteristic bands assigned to DMF signature at 1658 cm^{-1} - which appears as a shoulder on the left of the $NiCl_2$ band, 1385, and 1122 cm^{-1}, assigned to C=O stretching, $–CH_3$ bending, and C–N stretching, respectively. Bands related to DMF identified in the spectrum of PSZNi2.5 also appear in the spectrum of the PSZ solubilized in DMF - labeled PSZ_DMF - that underwent the same synthesis procedure as PSZNi2.5, however, without $NiCl_2$.

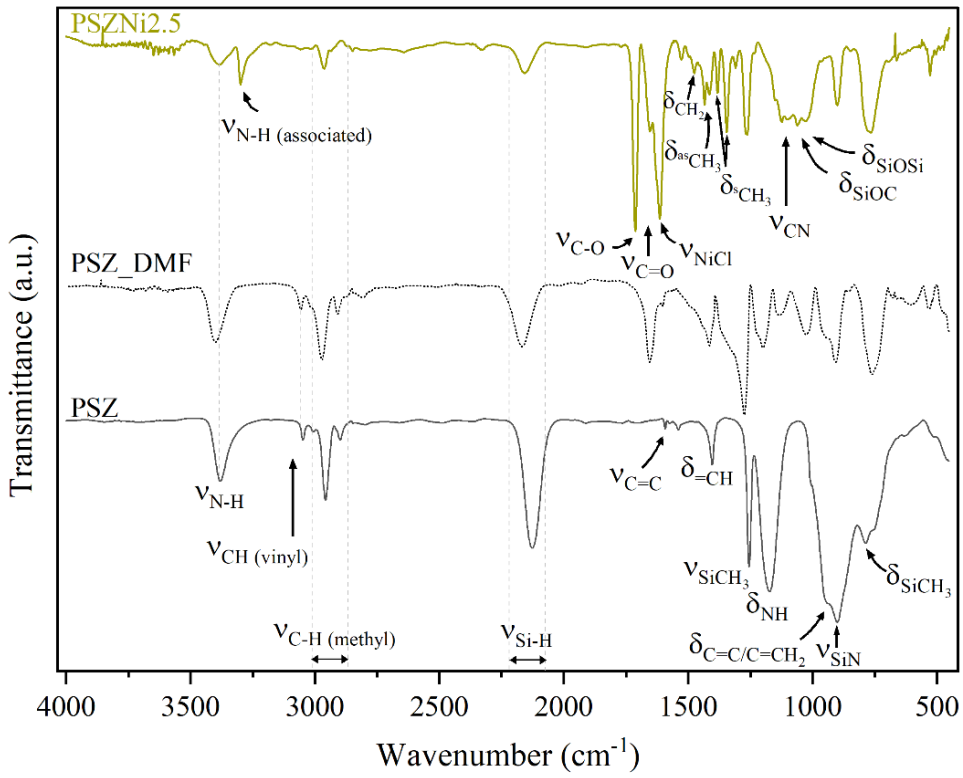

Figure 4.26. FTIR spectra of PSZ, PSZ_DMF and PSZNi2.5_5 samples.

The single N-H band (1169 cm^{-1}) present in PSZ spectrum also turns a quadruplet from 1168 to 980 cm^{-1}, indicating that NH groups from PSZ associate with C=O groups from DMF via N-H···O=C hydrogen bonding, hence, reinforcing that crosslinking reactions occur via Si-O linkage formation, turning the PSZ into an N- and O-donor organosilicon polymer.

In comparison to PSZ and PSZ_DMF, the bands related to Si-N stretching in Si-N-Si units at 904 cm^{-1} as well as Si-C bonds at 779 cm^{-1} sharpen. Absorption bands related to νNH, νCH of vinyl and methyl groups, νSiH, νC=C and δNH in Si-N-Si units significantly decrease or almost vanish, whilst those of CH_2 and CH_3 from 1530 to 1340 cm^{-1} appear, pointing out dehydrocoupling reactions of NH and SiH, and hydrosilylation reactions of SiH across -C=C-.

Wan *et al.*, (2019) have reported alike effects concerning the use of TM compounds as catalysts promoting a remarkable increase in hydrosilylation rate and decreasing the temperature at which such reaction happens. Moreover, since the discovery of homonuclear B-B bonds published by Corcoran and Sneddon (1984), the use of TM to catalyze dehydrocoupling reactions forming bonds between main groups such as groups 14 and 15 - like the element-element bonding of Si-N coming from dehydrocoupling in the temperature range of 20-90 °C - has been investigated as a convenient alternative to traditional routes [128].

Considering the above-discussed results, the synthesis condition (DMF reflux) and the fact that a fast color evolution happens during precursor preparations, especially the ones containing $NiCl_2$, as shown for PSZNi2.5 in Figure 4.25, some important reaction aspects can be anticipated: firstly, the metal salt is most probably incorporated in the PSZ network via silylamino and/or siloxane ligands, as shown by the coordination of Ni^{2+} to these favorable ligands in the side groups of PSZNi2.5. In addition to that, the polymer represents a Ni:organosilicon polymer coordination complex in which the metal catalyzes crosslinking linkages through Si-O-Si, Si-C-C-Si and Si-N-Si units formation that arises from DMF's reduction by Si-H, hydrosilylation and dehydrocoupling reactions, respectively, hence, generating a highly crosslinked compound.

After a better understanding of the interactions between nickel chloride and preceramic precursor in the ratio of 2 .5, the ratios 10, 5, and 1 were tested, leading to dark yellowish/brownish and grey/bluish powders. Besides the change in Si:Metal molar ratio, reactions with cobalt chloride were also evaluated (see Table 3.4 (page 53)). Figure 4.27 shows the final aspect of as-obtained polymers.

Figure 4.27. As-obtained TM Chloride modified-PSZ polymers according to the Si:Metal ratio.

The effect of mixing both metal chlorides was investigated in the molar ratio of PSZ to metal fixed at 5, that is, PSZ:Co = 5 and PSZ:Ni = 5, and in the ratio of 1.3 with regards to cobalt and 0.7 for nickel, to compare the impact of such differences in the final product. For these syntheses, both $CoCl_2$ and $NiCl_2$ were simultaneously added to the flask inside the glovebox taking into account that they possess distinct reactivities as well as to avoid further opening of the system. These samples were named PSZNi5Co5 and PSZCo1.3Ni0.7, respectively.

Similar effects observed in the as-discussed PSZNi2.5 are seen for other PSZMx. Figure 4.28 and Figure 4.29 show the IR spectra of Co- and Ni-containing PSZ. It is observable that both cases show an intense band of MCl_2 at 1612 cm^{-1}. Similarly to PSZ_DMF, bands assigned to DMF signature are detected at 1658 cm^{-1} (νC=O), 1385 cm^{-1} (δCH_3) and 1122 cm^{-1} (νC-N), whilst bands not observed at 3301 cm^{-1} and 1715 cm^{-1} in pure PSZ and PSZ_DMF are seen for both metal-containing polymers.

The single N-H band (1169 cm^{-1}) also turns a quadruplet from 1168 to 980 cm^{-1}, and NH groups from PSZ associate with C=O groups from DMF via N-H···O=C hydrogen bonding. Bands related to Si-N stretching in Si-N-Si units at 904 cm^{-1}, as well as Si-C bonds at 779 cm^{-1}, sharpen and a decrease or almost disappearance of νNH, νCH of vinyl and methyl groups, νSiH, νC=C and δNH in Si-N-Si units in these other metal-containing polymers is observed as in PSZNi2.5. Compatible, absorption bands of CH_2 and CH_3 from 1530 to 1340 cm^{-1} appearance points out dehydrocoupling reactions of NH and SiH, and hydrosilylation reactions of SiH across -C=C-.

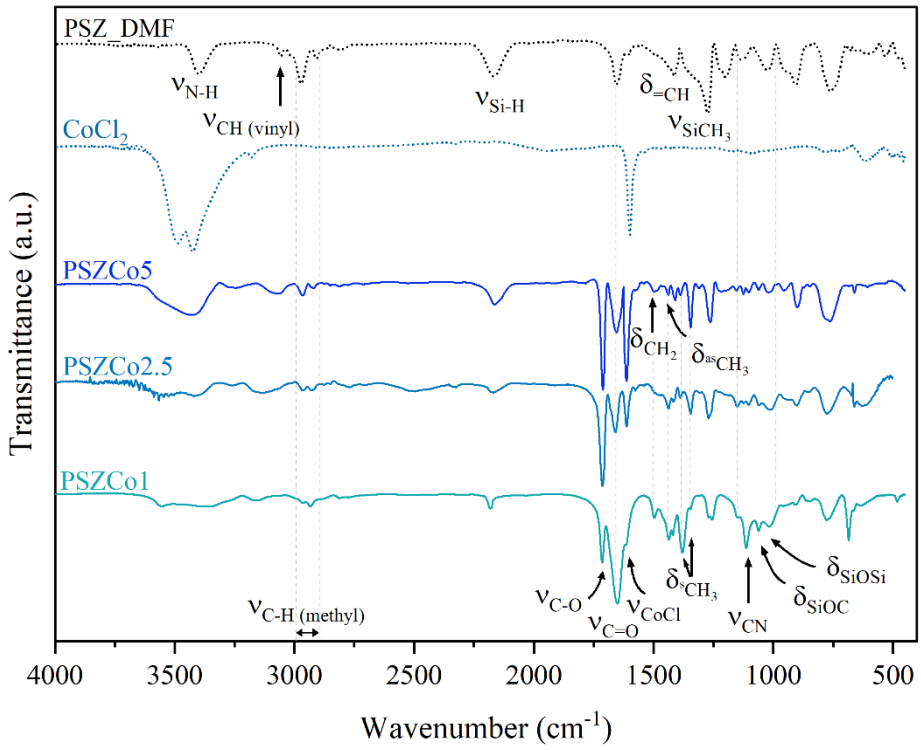

Figure 4.28. FT-IR spectra of pure $CoCl_2$ and Co-modified PSZ polymers in the ratios of 5, 2.5, and 1 compared to PSZ_DMF sample.

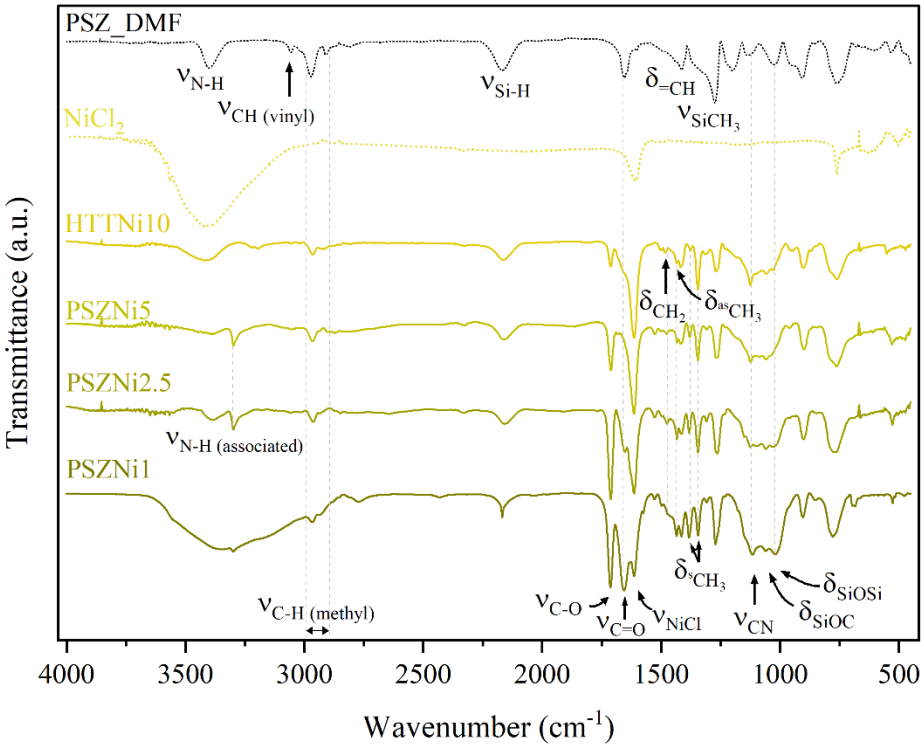

Figure 4.29. FT-IR spectra of pure $NiCl_2$ and Ni-modified PSZ polymers in the ratios of 10, 5, 2.5, and 1 compared to PSZ_DMF sample.

These phenomena can also be discussed in terms of the Si:Metal molar ratio. For instance, in the smaller content of nickel precursor (PSZNi10), a broader intensity of N-H group is observed. By increasing its content, that is, reducing the silicon-to-metal molar ratio, the intensity of N-H bond significantly reduces as observed for both PSZNi5 and PSZNi2.5 polymers. PSZNi1 is the only sample that did not follow this trend, instead, it exhibits a broader band comparable to the observed in pure $NiCl_2$. Probably, the higher metal content catalyzes the association of NH groups from PSZ with C=O groups from DMF via N-H···O=C hydrogen bonding and favors dehydrocoupling reactions as seen by a more prominent stretching of Si-O-C and the narrower band of Si-H in comparison to the other samples. On the other hand, the greater metal content likely originates more byprodutcs such as H_2O, explaining the broadband from 3000 to 3600 cm^{-1}. From these conclusions, the molar ratio of 2.5 is the one providing the higher metal content without compromising the occurrence of important chemical reactions.

With regards to the mixing of metals (Figure 4.30) whether the molar ratio between Si and each metal is the same, it seems that complete crosslinking of PSZ is reached, as evidenced by the disappearance of δSiCH=CH_2, νCH, and νSiH. Along with that, Si-O-C and Si-O-Si bonds are barely observed, whereas a broad intensity of νC=C and δCH deformations (1590 cm^{-1} and 1400 cm^{-1}) is seen. By changing the molar ratio between silicon and both metal precursors (PSZCo1.3Ni0.7), the content of $NiCl_2$ is greater than that of $CoCl_2$ due to the smaller molar ratio of 0.7. This sample shows a small band of νCH, a sharp band of νSiH, and more expressive stretching of νSi-O-C/Si-O-Si bonds than PSZNi5Co5.

Recently, Yang and Lu (2021) evaluated the catalytic effect of Fe, Co, and $NiCl_2$ and demonstrated that the difference in the electronic configuration of Ni ($[Ar]3d^84s^2$) and Co ($[Ar]3d^74s^2$), which gives a d shell occupancy of 8 and 7 electrons, concomitantly, has an important influence on which metal will be more catalytically active. Taking that into account, and the reactivity order of Fe>Co>Ni, these contrasting results of mixing TM with PSZ might happen because when metals are available in the same ratio, cobalt could have a major impact than nickel, whereas when there is a greater content of the later, the system could rather catalyze interactions between PSZ and DMF, corroborating with the effects of TM on the evolution of polymer-derived SiOC evaluated in the reference study [129].

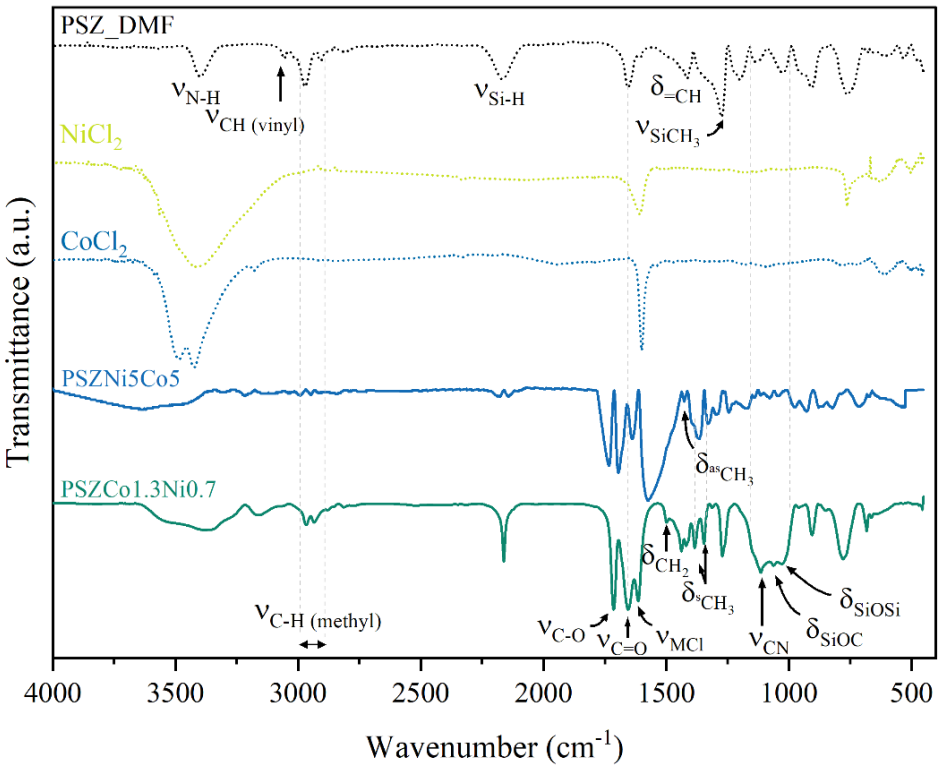

Figure 4.30. FT-IR spectra of the mixed metals precursors with PSZ in the total ratios of 5 and 2.

Although FTIR characterization has brought interesting evidence about the reactions involved in the system in question, further analysis must be done to confirm it. In view of that, the thermal behavior was investigated for more precise information and is discussed in the following subsection.

4.3.1.1. Thermal behavior investigation of metal chloride-modified PSZ

The thermal behavior of the precursors previously analyzed has been monitored using TG analyses occurring under flowing argon. Figure 4.31 shows the thermal behavior of polymers generated with $CoCl_2$ in the three Si:Co ratios investigated, whereas Figure 4.32 is dedicated to samples generated utilizing $NiCl_2$ as the metal precursor.

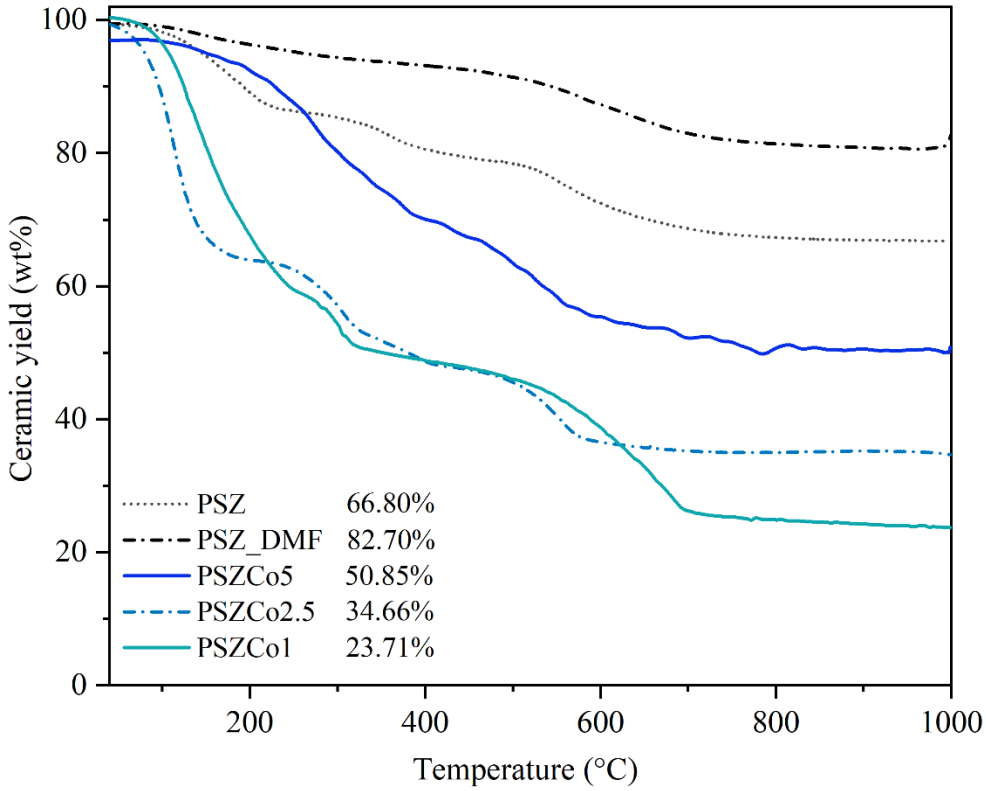

Figure 4.31. TG analysis of pure PSZ, PSZ_DMF and Co-modified PSZ polymers in different Si:Co molar ratios under Argon atmosphere.

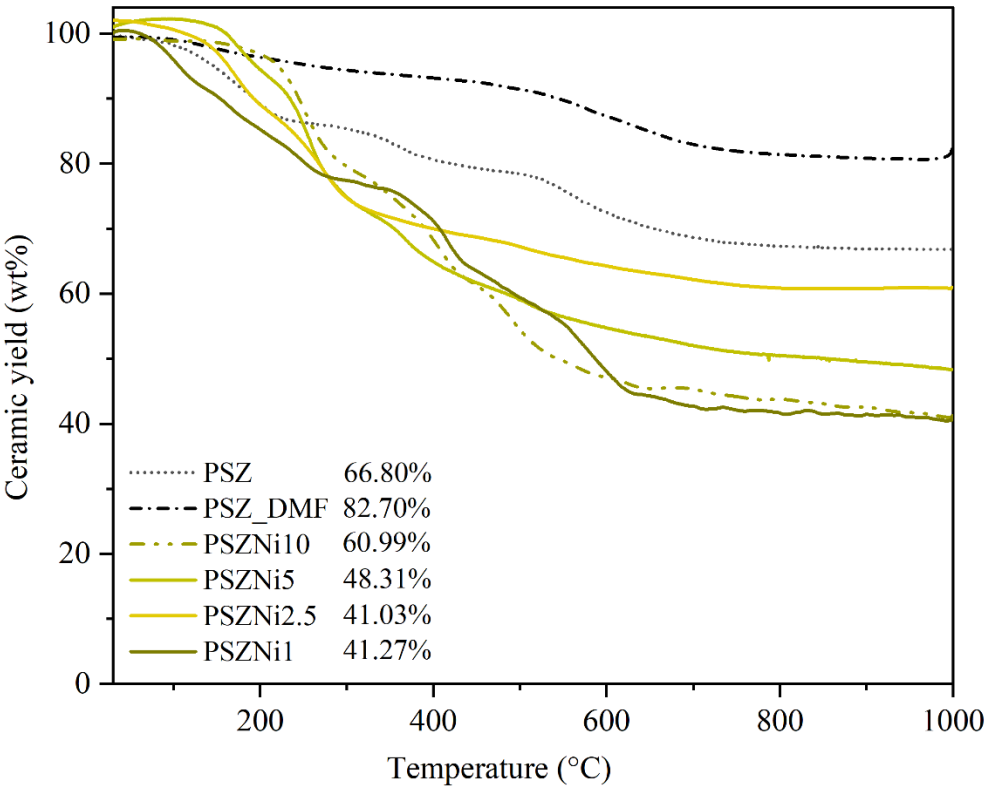

Figure 4.32. TG analysis of pure PSZ, PSZ_DMF and Ni-modified PSZ polymers in different Si:Ni molar ratios under Argon atmosphere.

Firstly, it is possible to observe that metal-containing PSZ products exhibited a similar thermodegradation pattern according to the Si:Metal ratio. By increasing the metal content, a reduction in ceramic yield was observed for both Co and Ni precursors. Likewise, a previous study from this research group reported a similar trend concerning ceramic yield reductions when polymers obtained by reacting PSZ with Ni- and $CoCl_2$ in toluene were submitted to thermogravimetric analysis under argon atmosphere [130].

With a mass spectrometer coupled to TGA, it was possible to detect the gaseous species released during PSZCox and PSZNix samples' thermogravimetric essay. Apart from ammonia (NH_3, m/z = 17), all species detected in Ni-containing PSZ are seen for PSZCox samples: dihydrogen (H_2, m/z = 2), carbon (C, m/z = 12 and 13), methane (CH_3 m/z = 15), ammonia or hydroxyl (NH_3 OH, m/z= 17), ammonium or water (NH_4 or H_2O, m/z = 18), CN or C_2H_2 (m/z = 26), ethene (C_2H_3, m/z = 27), ethane or CHO (C_2H_5, CHO m/z = 29), methylamine (CH_3NH_2, m/z = 30), C_2H_3N (m/z = 41), C_2H_4N (m/z = 42), C_2H_5N (m/z = 43), carbon dioxide (CO_2, m/z = 44), and ethylamine ($C_2H_5NH_2$, m/z = 45).

As mentioned earlier, dihydrogen is a product of dehydrogenation reactions, whilst ammonia and ammonium could be generated by thermal crosslinking and transamination reactions. Both cleavage of C=C bonds and $SiCH_3$ decomposition are responsible for CH_4 release. Once the solvent is the only possible source of oxygen in the system, carbon dioxide is highly like to be released from DMF's volatilization, which happens from 100 to 300 °C. Finally, hydrocarbon release may indicate chain cleavage by the elimination of side groups and also polyaddition reactions at the Si-Vi site and methyl/vinyl radical reactions (from 200 to 300 °C), which are chemically demonstrated by Equations (4.10) and (4.11), respectively. These byproducts could be further bonded to nitrogen and/or amine groups, forming CN, CH_3NH_2, C_2H_3N, C_2H_4N, C_2H_5N, and $C_2H_5NH_2$. Since no chlorine compound was detected in MS analyses, it might be another sign of Cl_2 incorporation into PSZ network.

$$n(\equiv SiCH = CH_2) \rightarrow \equiv Si(CHCH_2)_n \quad (4.10)$$

$$\equiv SiCHCH_2 + \equiv SiCH_3 \rightarrow \equiv SiCH_2CH_2CH_2Si \equiv \ or \ \equiv SiCH(CH_3)CH_2Si \equiv \quad (4.11)$$

In addition to these results, it is worth pointing out that in the molar ratio of 1, PSZNi1's ceramic yield was 41.27% whereas the sample PSZCo1 reached only 23.71%. As for the mixing

of metals, PSZNi5Co5, the ceramic yield is found to be 35.45%, whilst for PSZCo1.3Ni0.7, it is reduced by almost 3% (Figure 4.33).

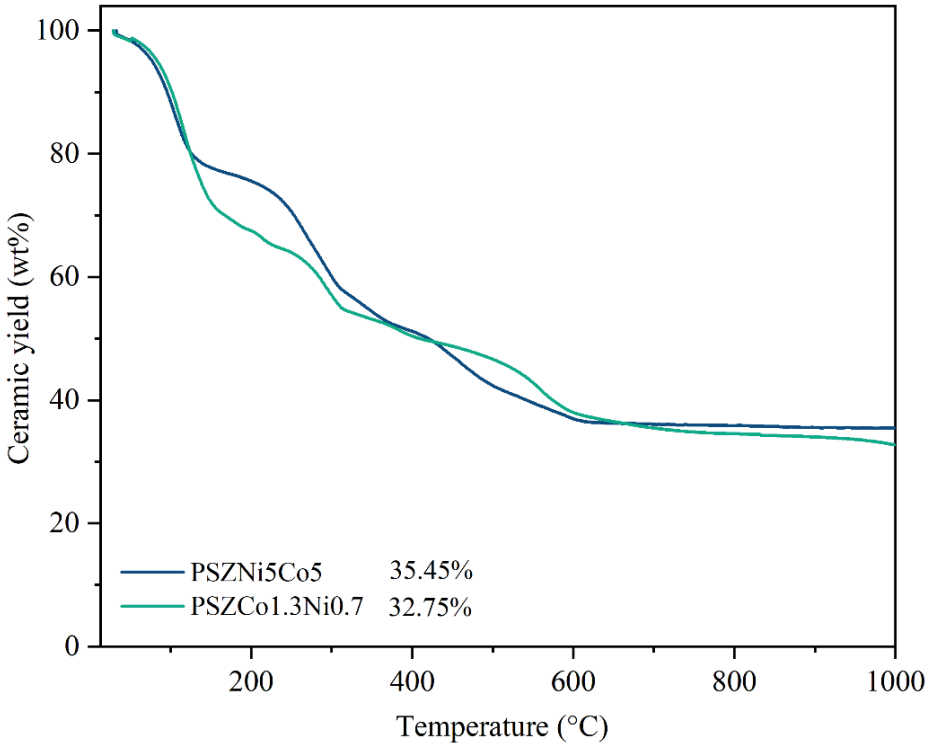

Figure 4.33. TG analysis of the Bimetallic-containing PSZ in different Si:Metal molar ratios under Argon atmosphere.

Taking into account that the ratio of 2.5 is the one that provides the greater metal content without compromising the material's properties, PSZCo2.5 and PSZNi2.5 were chosen to be investigated in more detail and heat treated under argon atmosphere at 500 °C. This temperature was defined based on previous thermal investigations performed from 300 to 1000 °C to determine the best condition to reach high SSA. Furthermore, in recent studies, the face-centered cubic crystal (fcc) structure transformation to hexagonal-centered cubic (hcc) one has been reported to occur at around 450 °C, being then, another reason to perform pyrolysis at this relatively low temperature, once these metastable Ni phases magnetic properties are of great interest for industrial use as catalyst [131]. Having said this, and as can be concluded from the TG curve of **PSZNi2.5**, 500 °C is considered the minimum temperature at which the weight loss rate is strongly reduced meaning that an inorganic sample is mainly delivered. Hence, the evolution of PSZNi2.5 properties was analyzed in the temperature range 500 - 1000 °C and will be discussed in section 4.3.1.2 (page 94).

4.3.1.2. Characterization of PSZNi2.5 after heat-treat at 500 °C

The thermolysis at 500 °C led to a compound, hereafter labeled PSZNi2.5_5, with an empirical formula of $Si_{1.0}C_{2.5}N_{0.4}O_{1.4}H_{4.4}Ni_{1.1}$ (*referenced to* $Si_{1.0}$, see

Table 4.1), a great decrease in Si:Ni ratio (0.9) has happened in comparison to the ratio of 2.5 defined for precursor synthesis. This reduction is associated with chlorosilane release during pyrolysis, causing a full elimination of chlorines as confirmed by the measured Cl content as low as 0.5 wt%. Furthermore, compared with Si and N contents, the high content of carbon indicates the presence of free carbon, as frequently reported in polysilazane-derived ceramics [132].

This sample was also submitted to Brunauer-Emmett-Teller (BET) analysis to evaluate if the pyrolysis at this relatively low temperature yielded a high specific surface area. As can be seen in the N_2 adsorption presented in Figure 4.34, the sample PSZNi2.5_5 displays a well-defined type II isotherm, which exhibits a shape characteristic of unrestricted monolayer-multilayer adsorption at high p/p^0, as proposed by IUPAC [133]. In a relative pressure range of 0.2 to 1.0, there is a distinct H_3 hysteresis loop implying that aggregates of plate-like particles are formed originating slit-shaped pores [134].

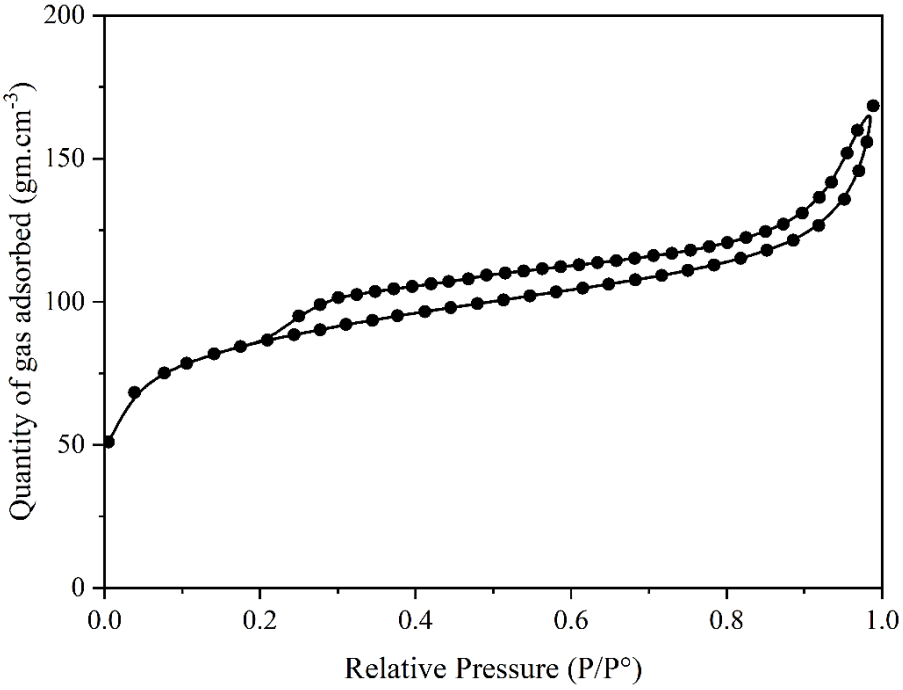

Figure 4.34. N2 sorption isotherms of PSZNi2.5_5 thermolyzed under argon environment.

A surface area of 311 $m^2.g^{-1}$ was measured and a t-plot analysis was performed to determine the volume of pores. The results indicate the presence of several micropores with an area of 201 $m^2.g^{-1}$. This high intrinsic microporosity is a result of residual DMF and gaseous species evolution that happens in the low-temperature regime of pyrolysis [135]. These characteristics strongly suggest that PSZNi2.5_5 is suitable to be applied in OER as it could allow easy access to the active Ni sites.

From the XRD patterns of PSZNi2.5 pyrolyzed at 500 °C depicted in Figure 4.35, it was possible to identify the crystalline phases providing the active sites for OER application. Note that the dominant diffraction peaks are at 2θ = 44.5°, 51.8° and 76.4° assigned to the (111), (200) and (220) lattice planes of the structure of stable face-centered cubic (fcc) Ni, with cell parameter α= 0.352 nm (file JCPDS no. 04-0850). The other peaks of lower intensities observed at 41.9° (100), 47.6° (101), 62.5° (102) and 84.1° (103) correspond to the interstitial-atom-free (IAF) hexagonal close-packed (hcp)-Ni phase, as also observed by Bolokang and Phasha (2011).

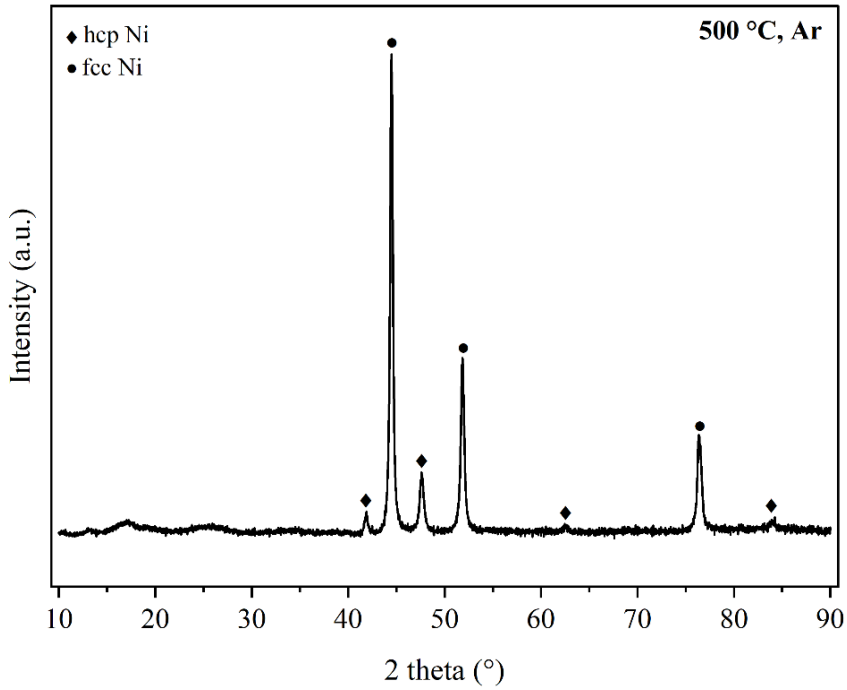

Figure 4.35. XRD pattern of PSZNi2.5_5 pyrolyzed under argon atmosphere.

Chiang, Chiang and Shieu (2014) have identified such a metastable phase as a possible intermediate phase throughout the transformation of Ni_3C into fcc-Ni. Supporting these findings, it could be concluded that the results obtained for PSZNi2.5_5 in the present work, are consistent with the crystalline behavior expected for nickel when treated in such a low-temperature regime of pyrolysis.

Even though the above-mentioned results are consistent with published studies, this conclusion cannot be drawn only by phase analysis once peaks overlapping is a common drawback of this qualitative investigation. This issue is grounded on the fact that the phase analysis alone does not discriminate overlapped individual Bragg reflections. Instead, it solely enables the determination of the crystal system and lattice parameters by peak fitting and indexing [137]. Therefore, a quantitative analysis is paramount to distinguish which phase was truly formed as well as to quantify their fractions in case two or more phases coexist.

For that goal, the Rietveld refinement is a mathematical method developed in the late 1960s to refine powder structures by minimizing differences between intensities of observed data and a known model over the whole diffraction pattern [138]. It is usually carried out by the least-squares refinements until the best fit between the experimental and calculated results is achieved. This calculated pattern comprises models of the crystal structure(s), diffraction

optic effects, instrumental factors and lattice parameters, which are simultaneously refined [139].

Given the requirement of detailed information on the crystalline structure, in this work, Fullprof was used to perform the refinement and certify which phases were formed. This analysis was performed using the existing database of reference diffractograms and the refinement patterns obtained for sample HTTNi2.5_5, which is exposed in Figure 4.36. The phase analysis had an acceptable peak fitting in terms of crystal structures formed, as confirmed by the Rietveld refinement of XRD patterns. The refined cell parameters for the fcc-Ni phase are α = 0.3523 nm, and α = 0.2491 nm and c = 0.4083 nm for the hcp-Ni phase. Such cell parameters are distinguishable from those of other phases such as hcp Ni_3N (α = 0.2667 nm and c = 0.4312 nm) and Ni_3C (α =0.2628 nm and c = 0.4306 nm), also identified for Ni-modified PSZ [140,141]. Moreover, they are closer to the cell parameters theoretically predicted for IAF hcp-Ni (α = 0.2500 ± 0.001 nm and c = 0.3980 ± 0.006 nm) and comparable to those of hexagonal close-packed Ni phase from Ni(II) glycinate [142,143]. In addition, this result is also consistent with the cell constants of the hcp Co analog (JCPDS 89-7373;), commonly referenced to justify the IAF hcp-Ni phase formation [144].

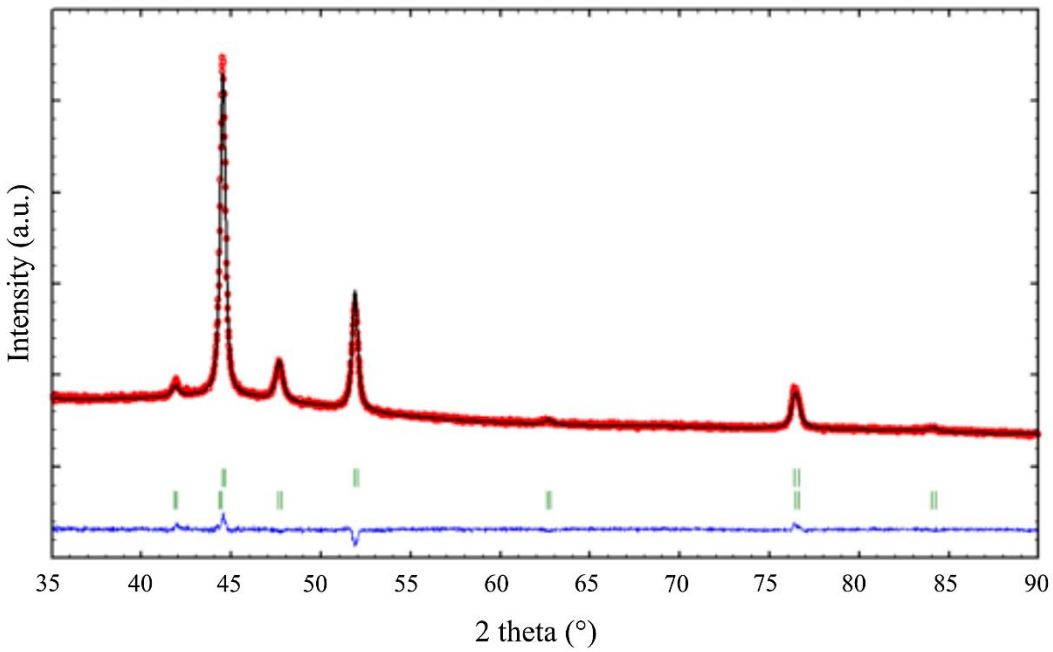

Figure 4.36. XRD pattern (red circles) and Rietveld refinement (black line) of PSZNi2.5_5 sample, with green vertical tick marks corresponding to fcc-Ni (upper) and hcp-Ni (lower).

The Rietveld refined relative weight fraction obtained for fcc-Ni was the most prominent, corresponding to 85% whereas hcp-Ni phase was solely 15%. Refined microstructural parameters led to apparent crystallite sizes of about 42 nm in the case of fcc-Ni (and apparent microstrains of 0.17%), and 16 nm for hcp-Ni, thus, elucidating that nickel was obtained in the nanometric scale without oxidizing. Besides, differently from what is commonly reported for the mixing of Ni complexes with organosilicon polymers, silicide phases are not detected here [100,108].

It is worth highlighting that studies related to metal-stable Ni phases have been done due to magnetic properties that are of great interest for industrial use. According to the literature, its crystallization starts with the face-centered cubic crystal structure up to its melting point under ambient pressure conditions and undergoes to a second-order phase transition from ferromagnetic to paramagnetic at around 356 °C. Besides that, other studies focus on the metastable hcp Ni as its magnetism is different from its fcc phase, being reported to occur in a range of a few nanometers crystalline size [131,136].

For a thorough investigation of the formation of fcc-hcp polymorphic Ni observed in the XRD pattern, the PSZNi2.5_5 sample was subjected to a thorough FEG-SEM and high-resolution TEM (HRTEM) analysis, and the results are depicted in Figure 4.37 and Figure 4.38, respectively. First, it can be pointed out from elemental mapping results shown in Figure 4.37 that PSZNi2.5_5 possesses five major elements in both micrometer and nanometer ranges. Furthermore, as highlighted by the arrows, Ni-rich domains are not observed in the mapping of Si, C, N and O, so that, it is possible to consider that Ni is a single-phase anchored upon the Si-N-C-O(H) matrix. Likewise, the Si- and O-rich domains (white squares) are not seen in the mapping of Ni, as can be seen by the dark space inside the white circles. This behavior not only confirms that the metal is not linked to these atoms but also that Si and O are linked to each other.

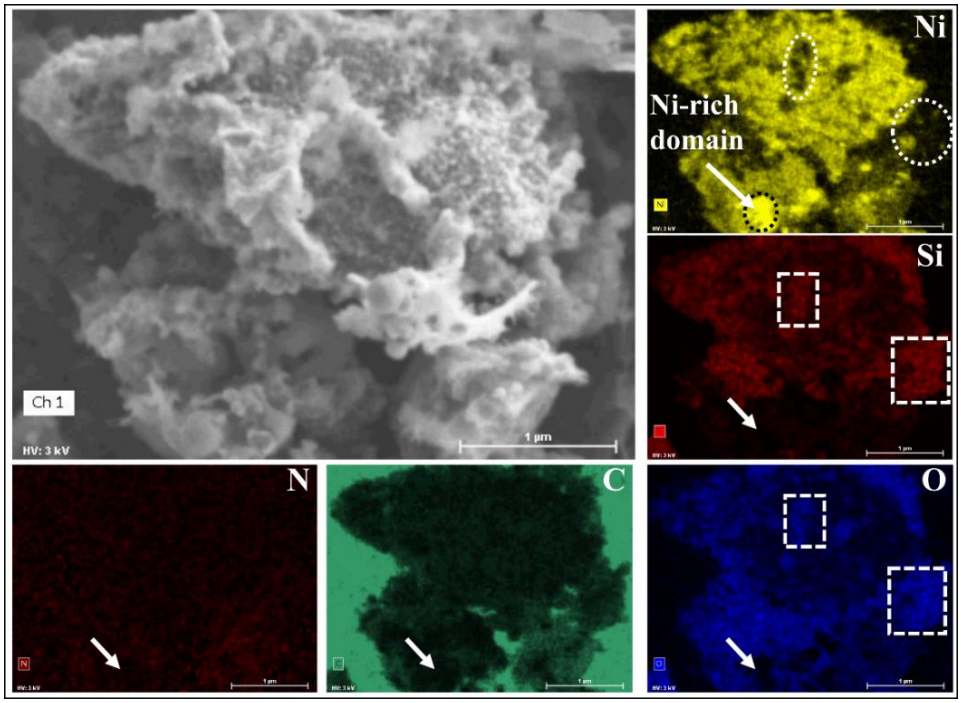

Figure 4.37. Figure 4.21. FEG-SEM micrograph of PSZNi2.5_5 and corresponding elemental mapping images.

As for TEM images, Figure 4.38 (a) and related insert, shows that the sample is an amorphous matrix composed of homogeneously dispersed small nuclei that appear as embedded dark dots. Its associated SAED pattern (Figure 4.38 (b)) exhibits spots, indicating that the analyzed phase is highly crystalline. This pattern related to the sample's structure is in good agreement with XRD results, as the calculus of d-spacing from SAED provides values correspondent to lattice parameters of fcc-Ni phase, i.e., (111), (200), (220) and (311), along with those of the proposed IAF hcp-Ni. Moreover, it is observable in Figure 4.38 (c) that Ni size is relatively heterogeneous locally once there are two Ni nanoparticles populations co-existing in this system: one comprising relatively big particles owing a size ranging from ~40 to 70 nm, which was isolated and its corresponding HRTEM image is exposed in Figure 4.38 (d). From this investigation, a lattice distance of 0.202 nm has been measured, which is related to reflections of (111) planes of fcc-Ni. Furthermore, it can be seen that these particles are coated by carbon layers, once there is an interlayer distance of 0.34 nm, thereby, originating core-shell nanostructures. Besides that, the smallest particles identified in Figure 4.38 (c) have also been isolated and exhibit an average particle size as low as 5.9 ±1.2 nm, which can be further seen in the histogram presented in Figure 4.39.

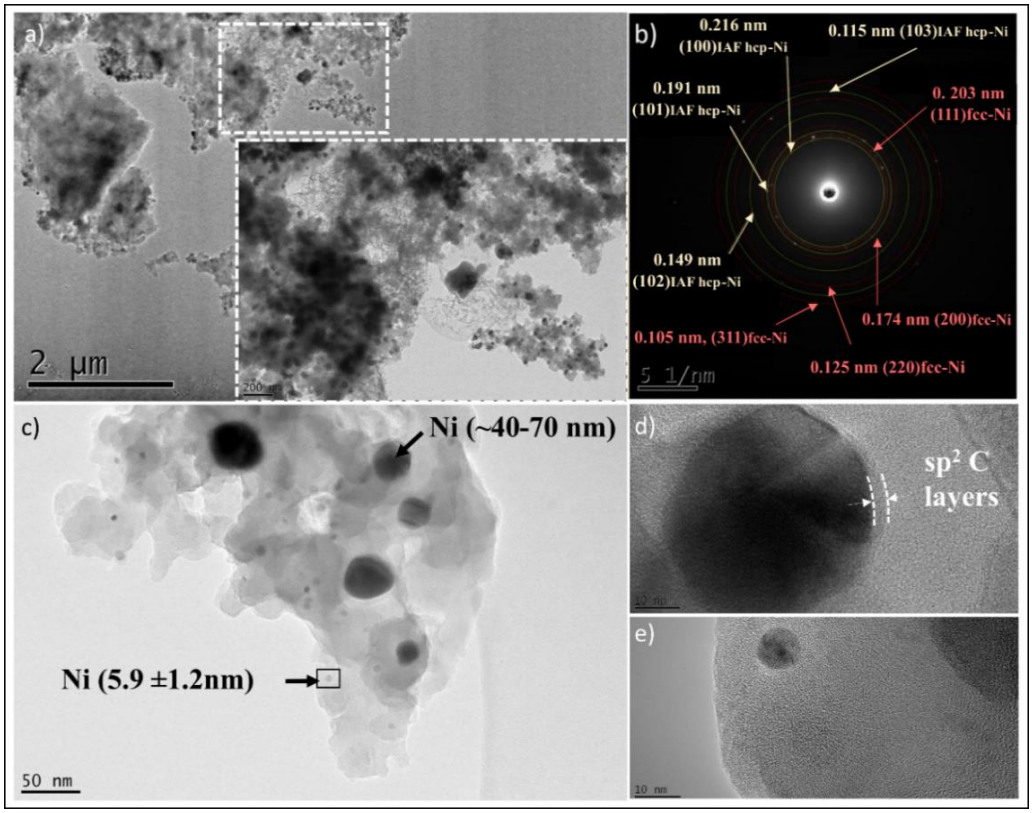

Figure 4.38. (a-c) Low magnification TEM images of PSZNi2.5_5, (b) SAED pattern correspondent of image a, (d,e) high magnification images of big and small nanoparticles isolated in PSZNi2-5_5.

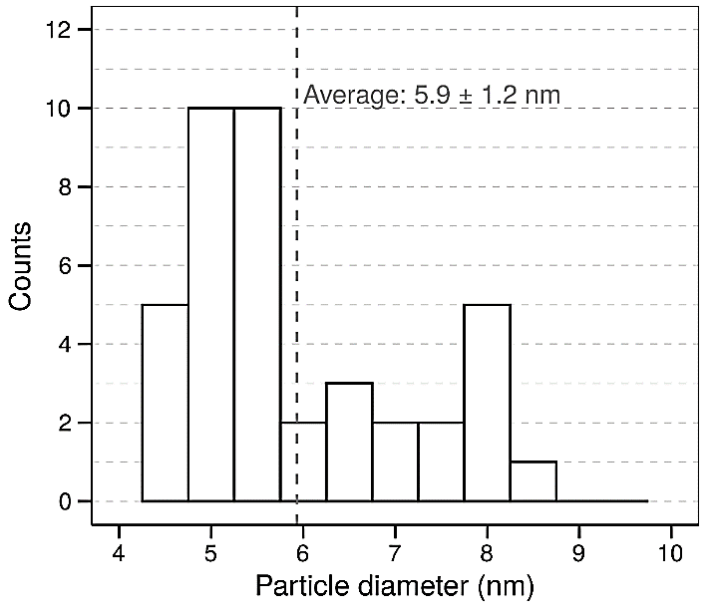

Figure 4.39. Size distribution histogram of the smallest particles present in HTTNi2.5_5.

By analyzing the HRTEM image shown in Figure 4.38 (e), it was detected that the fringes own a reduced spacing of 0.19 nm, corresponding to reflections of (101) planes of IAF hcp Ni. More than that, the carbon layers surrounding the biggest nanoparticles are not observed as a shell covering the smallest ones. These distinct observations agree with XRD results, as they allowed the conclusion that such smallest population of Ni particles corresponds to a metastable hcp-Ni phase.

To confirm that, the SAED pattern of an area containing relatively large particles ranging from 100 to 200 nm was evaluated and it was detected that they are composed of fcc phase solely. To explore the area of particles with reduced size, a TEM image was recorded and from this, the hcp Ni phase could be indexed along with the fcc phase in the associated SAED pattern. These specific investigations of big (upper) and small (bottom) particles are shown in Figure 4.40.

From all these characteristics, it seems logical to assume that the passivating effect of the PSZ matrix caused the confinement of Ni particles in a covalently-bonded Si-N-C-O matrix. This behavior is presumably what restrains the close-packed layers' slippage, hence, prompting the formation of the IAF hcp Ni phase. Similarly, in the last few years, Chiang, Chiang and Shieu (2014) have suggested alike behavior for carbon layers surrounding Ni particles. The authors reported the formation of HCP Ni phase during Ni_3C thermal decomposition at 500 °C, as an intermediate phase of fcc-Ni and carbon, due to a graphite-like shell adhesion on Ni nanoparticles constraining hcp layers slip and hence hindering its transformation to fcc Ni.

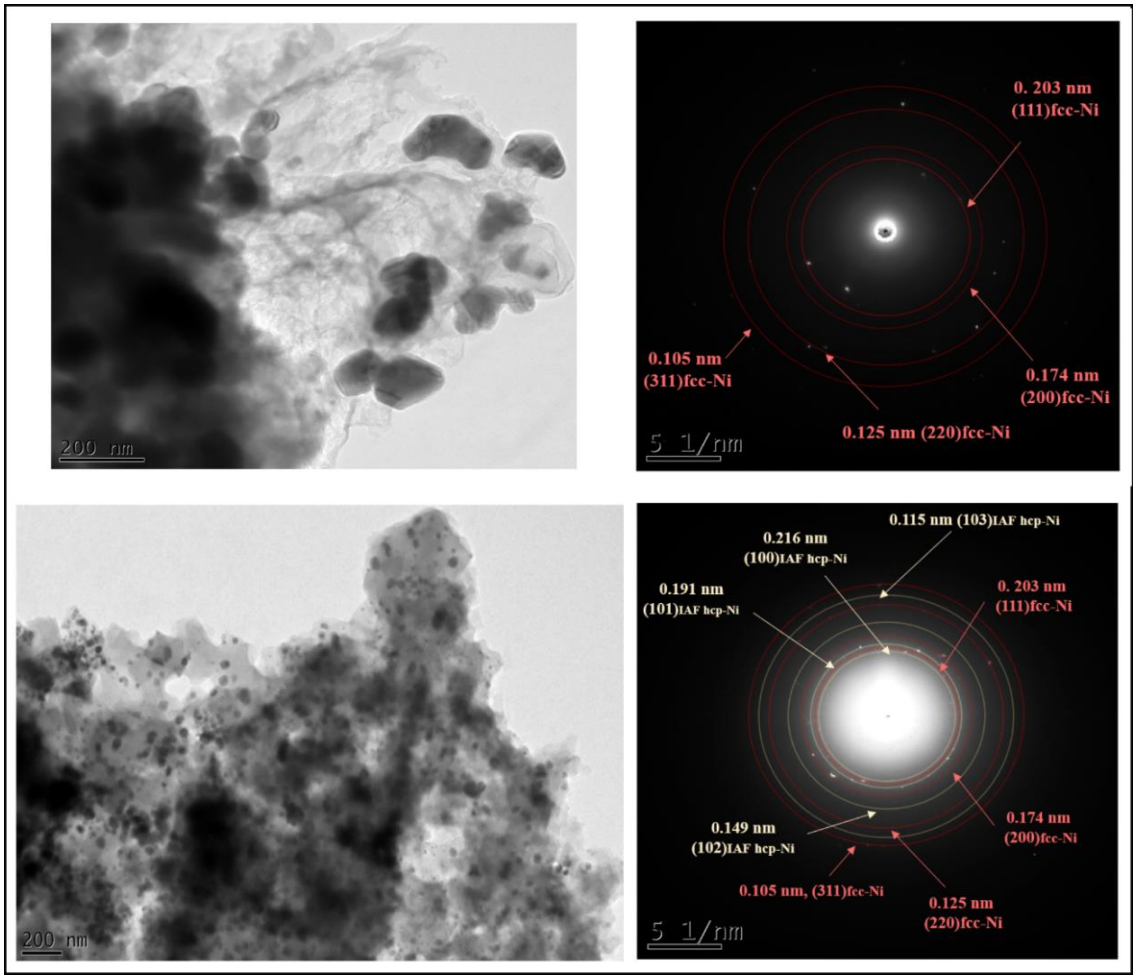

Figure 4.40. TEM micrograph of a population composed of the biggest (upper) and with the introduction of the smallest population particles (bottom) isolated in PSZNi2.5_5 and their corresponding SAED patterns, respectively.

After this full investigation of the **PSZNi2.5_5** samples, the evolution of phases composing such material through its heat treatment at 700, 800 and 1000 °C in flowing argon was followed.

4.4. Characterization of final ceramics from 700 to 1000 °C

Because the pyrolysis temperature is a crucial parameter for the formation of nanocomposites with improved performances, as it has a direct effect on features like the nanopore network, an in-depth investigation of produced samples was performed in this study not only for PSZNi2.5_5 but also for other important materials and from 700 to 1000 °C. For that, the samples were pyrolyzed under argon atmosphere at different temperatures to

investigate their ceramic transformation according to the Si:Metal molar ratio and pyrolysis conditions. The ceramics obtained after pyrolysis were stored inside the glovebox and crushed for further analysis. Therefore, the crystalline structure and the microstructure of as-obtained ceramics were evaluated by XRD and TEM analysis.

4.4.1. Characterization of ceramics based on cobalt and nickel chlorides

The diffractograms obtained for PSZNi2.5 pyrolyzed at 700, 800, 900 and 1000 °C are provided in Figure 4.41. In all temperatures evaluated, it is visible that the three main peaks at 2θ = 44.5°, 51.8° and 76.4° are assigned to the fcc-Ni (file 00-004-0850) and the ones seen at 41.9° (100), 47.6° (101) corresponds to the interstitial-atom-free (IAF) hexagonal close-packed (hcp)-Ni phase, as observed for PSZNi2.5_5. The hcp-Ni phase appears in much less intensity when pyrolysis temperatures are higher than 500 °C though.

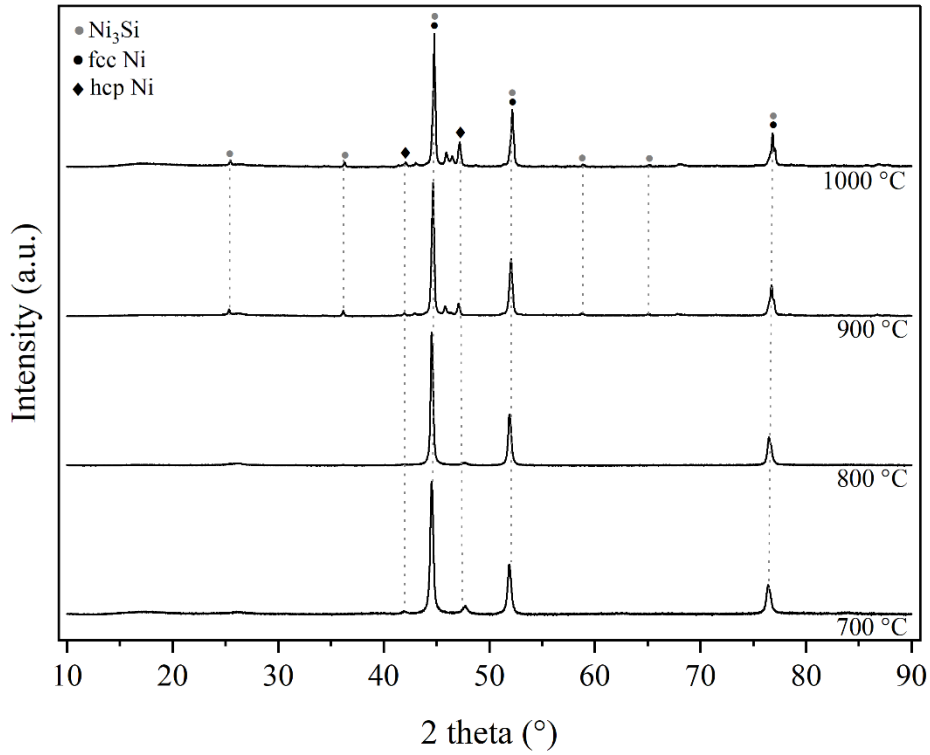

Figure 4.41. XRD pattern of PSZNi2.5 pyrolyzed at 700ºC (PSZNi2.5_7), 800ºC (PSZNi2.5_8) and 1000ºC (PSZNi2.5_10) under argon atmosphere.

Additionally, the three main peaks are also associated with Ni_3Si (04-001-3346), most probably because the temperature increase along with the higher degree of dehydrocoupling reactions facilitates such a bonding, which is reinforced by new small peaks rising at 900 and 1000 °C.

Table 4.2 indicates that the C, H, and N contents of PSZNi2.5 pyrolyzed at 800 and 1000 °C are much lower than that of PSZ, whereas the O content is higher in both cases, highly likely due to the incorporation of oxygen atoms into the SiCN matrix. Moreover, the very low amount of hydrogen and nitrogen confirms the occurrence of dehydrocoupling and transamination reactions and the establishment of a ceramic network. In addition to that, the low nitrogen content might also be a consequence of oxygen contamination, once polysilazane acts as an N-donor and possibly reacts with oxygens atoms from DMF molecules.

Table 4.2. Elemental composition (wt%) of PSZNi2.5 obtained after pyrolysis at 800 °C and 1000 °C under Ar atmosphere in comparison to PSZ.

Sample	**C (wt%)**	**H (wt%)**	**N (wt%)**	**O (wt%)**
PSZ	27.3	8.3	22.7	0.4
PSZNi2.5_8_Ar	16.8	0.5	3.1	14.6
PSZNi2.5_10_Ar	15.2	0.1	2.0	16.1

Regarding samples containing lower contents of metal precursor, Figure 4.42 provides XRD diffractograms of Ni-modified PSZ in the Si:Metal molar ratios of 10 and 5 (samples labeled **PSZNi10** and **PSZNi5**), treated at 1000 °C under argon atmosphere, whereas the same investigation at 800 °C is given in Figure 4.43.

It is known that the PDC-SiCN structure strongly depends on both the chemistry of the precursor and processing conditions. According to the literature, SiCN ceramics have an area of Si-containing species that are amorphous and comprises SiN_4 and SiC_4 tetrahedracores embedded in mix-bonded SiC_xN_{4-x} (x= 1-3) units, as well as free carbon generated by an assembly of relatively ordered carbon nanoclusters, respectively [145]. Taking that into account, the first fact that can be highlighted concerning these samples when treated at 1000 °C, is that the samples exhibit behavior more directed to the Si-containing species reported to exist in SiCN structures. Moreover, at this temperature, the samples presented crystallization of nickel silicon phases (Ni_2Si (04-010-3516); $Ni_{0.82}Si0.18$ (04-004-4506); Ni_3Si (04-001-

3346); and $Ni_{31}Si_{12}$ (04-007-1390)), agreeing that PSZ and metal precursor might associate, as discussed in section 4.3.1 (page 83).

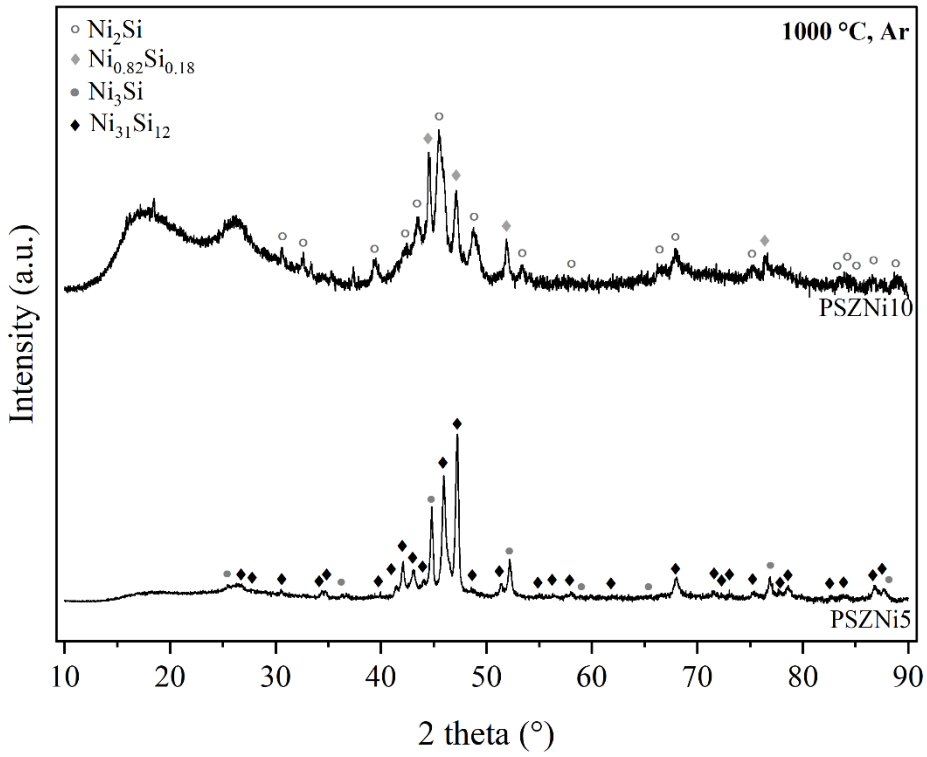

Figure 4.42. XRD pattern of PSZNi5 (PSZNi5_10) and PSZNi10 (PSZNi10_10) pyrolyzed at 1000ºC under argon atmosphere.

Contrarily, when pyrolysis was carried out at 800 °C, a clear change in crystallized phases can be noticed. For instance, in the lowest metal content (PSZNi10) several small peaks ascribed to γ-Si_5C_3 (ICDD No. 01-077-1084) are observed, whereas an increase in metal content led preferentially to the fcc-Ni phase crystallization (file JCPDS no. 04-0850), as observed by the main peaks at 2θ = 44.5°, 51.8° and 76.4°. It is seen therefrom that the Si:Me molar ratio has a great influence on the phases being formed under the same thermal treatment conditions.

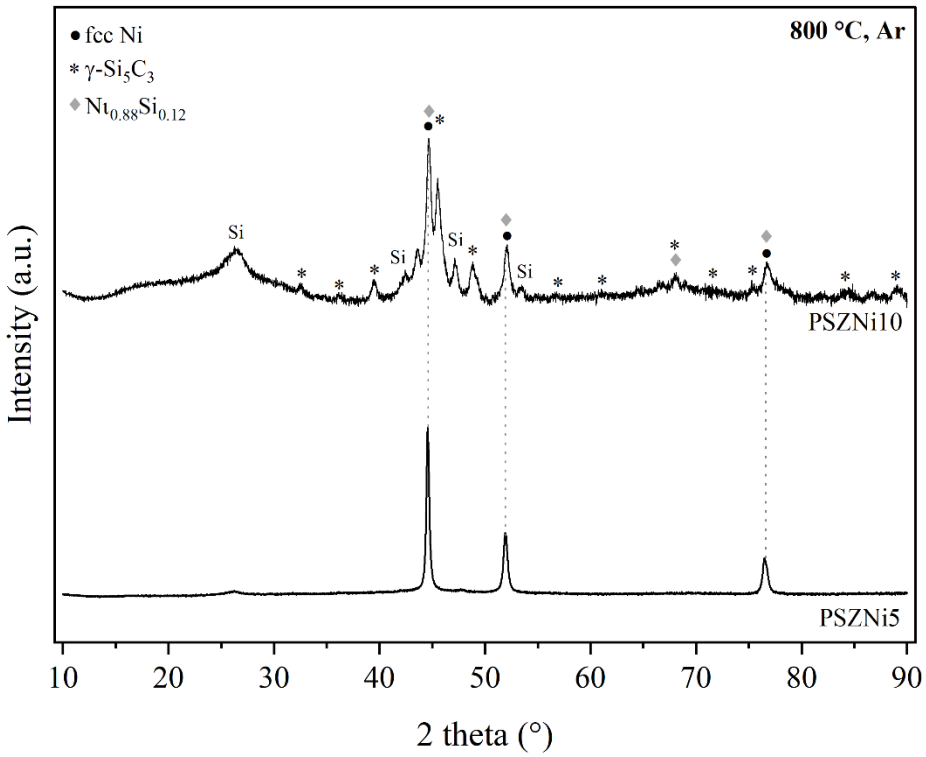

Figure 4.43. XRD pattern of PSZNi5 (PSZNi5_8) and PSZNi10 (PSZNi10_8) pyrolyzed at 800ºC under argon atmosphere.

Finally, diffractograms of PSZCo2.5 treated at 700, 800 and 1000 °C are depicted in Figure 4.44. In all temperatures evaluated, signals of cobalt silicon ($Co_{0.89}Si_{0.11}$, file 04-023-7058) at 2θ = 41.64° (100) and 47.52° (101), as well as cubic cobalt (file 00-015-0806) at 2θ = 44.22° (111), 51.52° (200) and 75.85° (220) are detected. Along with that, at 1000 °C, several peaks attributed to cobalt disilicide (Co_2Si, file 04-010-3523) are identified. From these patterns, it is clear that the nature of metal precursor also possesses a great influence on the final ceramics.

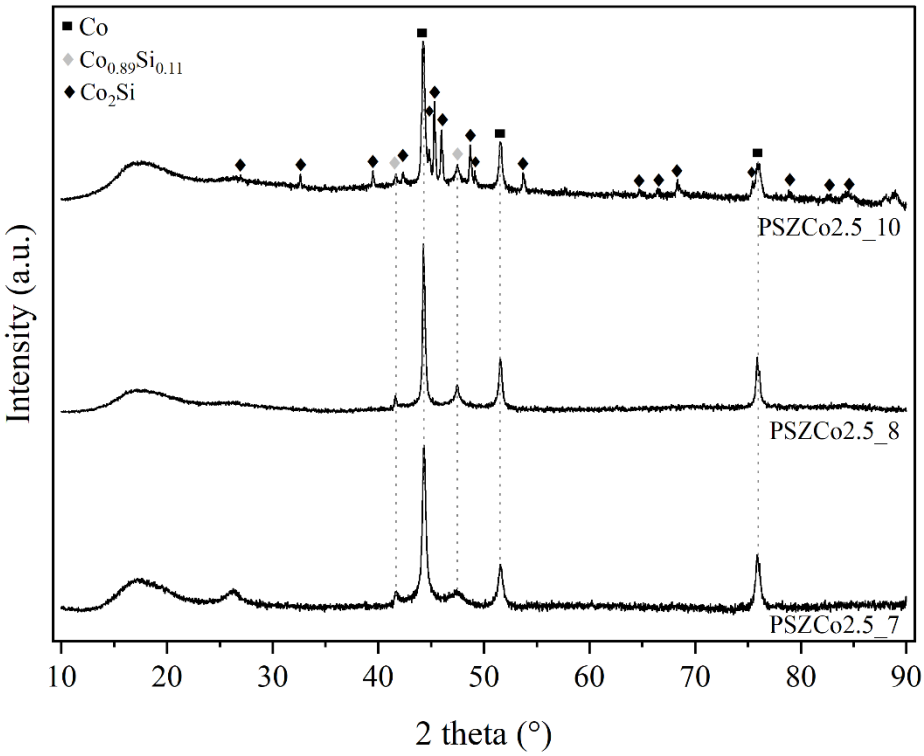

Figure 4.44. XRD pattern of PSZCo2.5 pyrolyzed at 700ºC (PSZCo2.5_7), 800ºC (PSZCo2.5_8) and 1000ºC (PSZCo2.5_10) under argon atmosphere.

Comparing the effect of metal precursor employed during reactions, it can be seen that the elemental composition is the same in both cases (see Table 4.2 and Table 4.3).

Table 4.3. Elemental composition (wt%) of PSZCo2.5 obtained after pyrolysis at 800 °C under Ar atmosphere in comparison to PSZ.

Sample	C	H	N	O
PSZ	27.3	8.3	22.7	0.4
PSZCo2.5_8_Ar	16.2	0.6	2.0	17.5

4.5. Oxygen Evolution Reaction (OER) investigation

Among all samples produced in this study, PSZNi2.5_5 was chosen to generate a catalyst active towards OER. The reason for this choice relied firstly on the fact that this molar ratio provided the higher metal content without delivering negative effects from a reaction standpoint. Along with that, the decision was based on prior scientific knowledge regarding PDCs features and electrolysis requirements. For example, it is widely known that preceramic polymers possess the inherent ability to form micropores when submitted to low-temperature

thermolysis regimes. During the polymer-to-ceramic transformation, preceramic polymers are capable of developing a high specific surface area (SSA) [146].

Moreover, during the hybrid state between preceramic polymer and final ceramic, which is referred to as ceramer state, transient micropore networks are formed mainly because of the evolution and decomposition of gaseous species [132]. However, a strong dependence on the preceramic system composition, structure and the processing conditions applied is observed when a critical process temperature is reached. In this condition, the microporosity disappears and the specific surface area passes through a significant decrease. The collapse of microporosity is probably a consequence of the viscous flow process within the material, which is thermodynamically driven by surface energy diminishment [147].

In the case of PDCs, a maximum of the specific surface area is reported for the pyrolysis temperature range of 400 to 600 °C. Interestingly, this temperature range is coincident with the maximum loss of mass that happens during the polymer-to-ceramic conversion. The discovery of micropore evolution in PDCs afforded several fundamental studies related to polysiloxanes, polysilazanes and polycarbosilanes.[99,135]. Therefore, pyrolyzing PSZNi2.5 at 500 °C was a promising approach to obtaining high specific surface area as well as microporosity.

For a thorough investigation and comparison, the electrocatalytic properties for OER of PSZNi2.5_5, PSZNi2.5_8, PSZNi2.5_10 and PSZCo2.5_10 samples were assessed. Their electroactivity was investigated using a rotating disk electrode set at 1600 rpm. Here, only results for PSZNi2.5_5 are presented, once according to all that has been discussed in the previous sections, this sample exhibited outstanding characteristics to be employed in alkaline water electrolysis, more precisely, as an OER electrocatalyst. Its high specific surface area, the immobilization of well-dispersed Ni nanoparticles, the presence of hcp-Ni phase (more active than fcc-Ni towards OER [30]), and sp^2 carbon along with the development of core-shell nanostructures are a combination of promising properties for the intended application and, therefore, motivated the investigation of its OER electrocatalytic features.

For that, a basic electrolyte (1 M KOH) was used and the electroactivity of the sample was analyzed in a rotating disk electrode set at 1600 rpm. Voltammetric cycles were performed between 0.8 and 1.55 V vs. RHE before recording the polarization curses exhibited in Figure 4.45. Upon electrochemical cycling, the catalytic surface was activated and the coulometry associated with the Ni^{2+}/Ni^{3+} oxidation wave increased (shown inset Figure 4.45) [148], indicating an increase in high valence electrochemically active Ni atoms. For this reason, it can

be postulated that the surface of Ni particles is reconstructed upon electrochemical cycling via the formation of lamellar oxy(hydr-)oxide. Regularly, it is accepted that a slight shift in the position of Ni^{2+}/Ni^{3+} redox transition towards higher electrode potentials happens due to the incorporation of iron from the 1 M KOH electrolyte [45]. Even though the specific effect of iron on the enhancement of OER activity is still a matter of debate [149], its concentration verified from ICP measurements is as low as 8 ppb, and hence, limits a possible boost of OER performance by Fe.

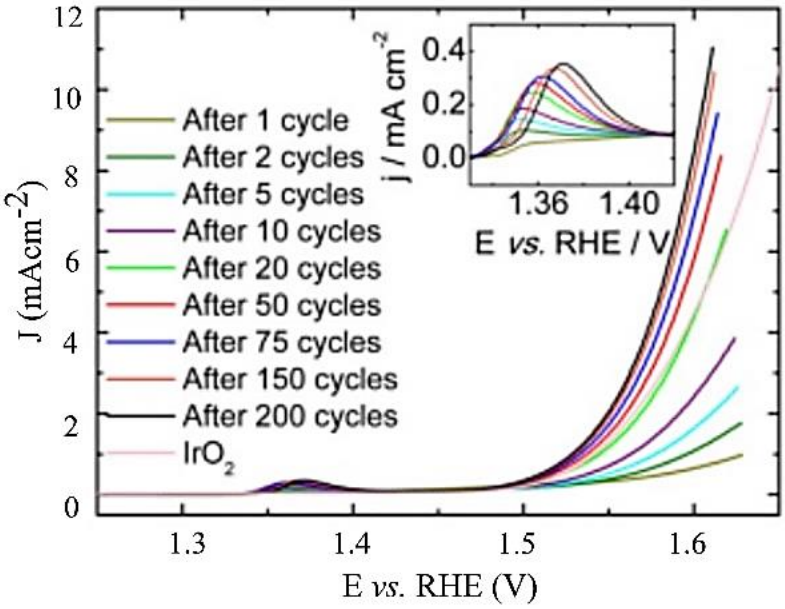

Figure 4.45. Polarization curves recorded at 5 mVs^{-1} after performing several voltammetric cycles in nitrogen saturated 1 M KOH electrolyte.

The OER activity increases during the activation phase and the catalytic surface stabilized after 200 voltammetric cycles, demanding a low electrode potential of 1.59 V vs. RHE to drive the standard current density (10 $mA.cm^{-2}$). Thus, from this polarization curve recorded after 200 voltammetric cycles, in the 1.5-1.56 V vs. RHE potential range, it was possible to calculate the Tafel slope, which corresponds to 66 mV dec^{-1}. Therefore, this value agrees that the rate-determining step corresponds to the second step of the OER process, considering that there was no surface blocking as well as fast electron transfer [150]. It is worth highlighting that the activity of PSZNi2.5_5 surpassed that of Ni/SiOC and Co/SiOC nanocomposites (1.62 V and 1.67 V vs. RHE, respectively [111]) with a commercial IrO2 catalyst (1.64 V vs. RHE).

Furthermore, as a comparison, PSZNi2.5_8 and PSZNi2.5_10 samples exhibited E_{j10} (V vs. RHE) values of 1.70 and 1.67 V, respectively. The performances of PSZNi2.5_8 and

PSZNi2.5_10 samples are rather low compared to that one of PSZNi2.5_5. That being said, this is an indication that the active surface area of the former is lower, most probably because of their lower BET SSA. By changing Ni by Co, the performance was even worse for the PSZCo2.5_10 sample (E_{j10} (V vs. RHE) = 1.78). Within this context, PSZNi2.5_5 was further investigated.

Because the particles crystallizing into hcp-Ni phase are much smaller than the fcc Ni particles, it can be inferred that the electroactive surface area is ascribed to the presence of the former, which is a phase reported for being more active towards OER than the latter [151]. That being said, it could be proposed that the surface reconstruction of Ni particles previously discussed happens at the surface of hcp-Ni nanoparticles, whereas the lamellar oxy(hydr-)oxide phase formation occurs with redistribution of carbon surrounding fcc-Ni particles, as depicted in Figure 4.46.

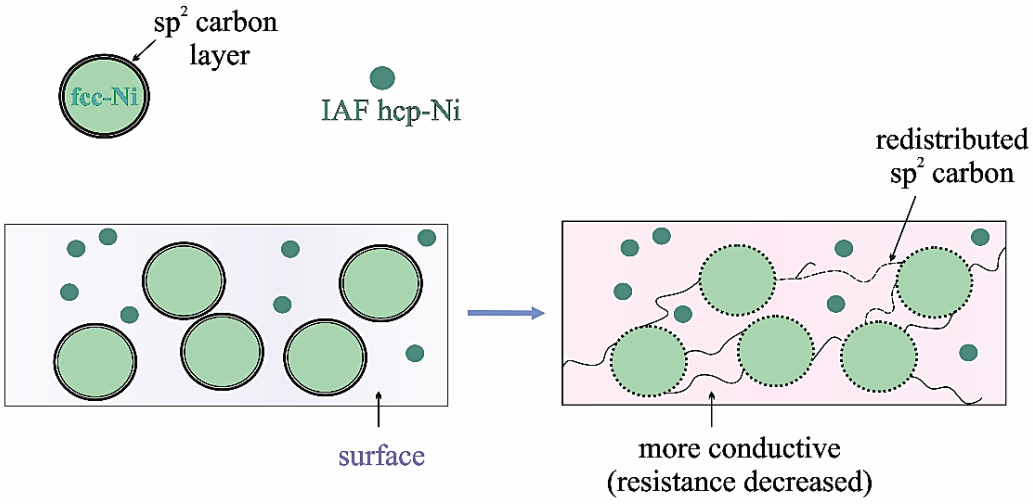

Figure 4.46. Schematic representation of removal of the carbon shell surrounding fcc-Ni particles to be redistributed within the Si-N-C-O(H) matrix under working conditions in a 1 M KOH electrolyte.

It can be therefore suggested that the carbon shell is gradually removed allowing the oxidation of fcc-Ni particle surfaces, as well as their redistribution within the Si-N-C-O(H) matrix, increasing the conductivity, which reflects in a resistance decrease. These effects together strongly demonstrate the promising 'pre-catalytic' behavior for OER of the PSZNi2.5_5 material under working conditions in alkaline electrolyte, especially because such

a result was reached with a mass loading solely composed of nickel and as low as 0.15 mg·cm^{-2}.

To shed more light on interfacial processes such as charge transfer and adsorption of reaction intermediates that take place during OER, electrochemical impedance spectra were recorded after voltammetric cycles and are shown in Figure 4.47 (a). The equivalent circuit model proposed by Armstrong-Henderson and presented in Figure 4.47 (b) was used to fit all spectra [152]. In this model, Rs corresponds to the cell resistance and comprises electrical connections, the electrolyte and catalytic load. The double-layer capacitance (C_{dl}) was modeled by CPE_{dl}. Both catalyst surface roughness and nonuniform distribution of active sites were taken into account replacing the classical capacitance by a constant phase element [153].

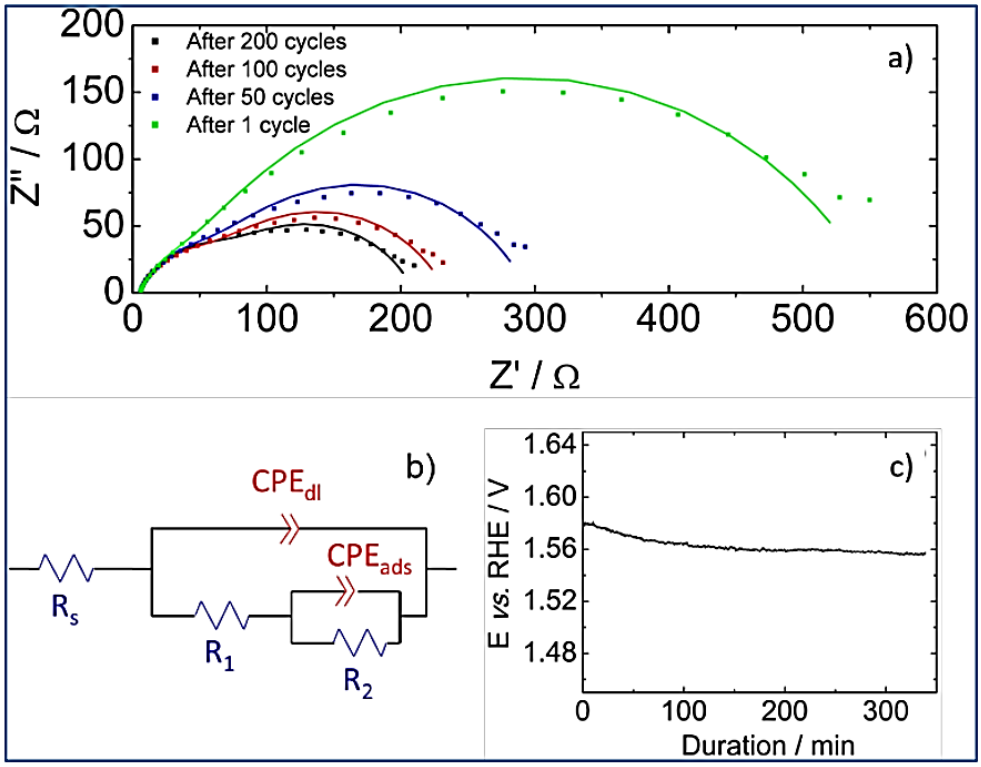

Figure 4.47. Impedance spectra obtained after voltammetric cycles in a 1 M KOH electrolyte at 1.7 V vs. RHE and their simulated curves (solid lines) (a), equivalent circuit model used to fit experimental electrochemical impedance spectra (b), and chronopotentiometric curve recorded for PSZNi2.5_5 catalyst immobilized onto a Ni foam in nitrogen saturated 1 M KOH electrolyte at benchmark current density (10 mA cm^{-2}) (c).

R_1 and R_2 allowed the simulation of the kinetics of charge transfer reaction. The sum of these two values provides the total faradaic resistance (R_{far}) [154], which must be considered

for the OER kinetics description. In addition, in parallel with R_2, CPE_{ads} values allowed mimicking the charge of reversible adsorption of OER intermediates [149]. From the best fit of spectra recorded at 1.7 V vs. RHE after 1, 50, 100 and 200 cycles, it was possible to obtain the values of R_s, R_{far} and C_{dl}, all of which, are presented in Table 4.4. With regards to the equivalent double-layer capacitance, it was obtained employing Brug's equation [155,156].

Table 4.4 . Values of the parameters Rs, R_{far} and C_{dl} obtained by the simulation of electrochemical impedance spectroscopy data.

Number of cycles	R_s/Ω	R_{far}/Ω	$C_{dl}/\mu Fcm^{-1}$
1	5.9	567	104
50	5.7	335	265
100	5.8	277	318
200	5.9	270	351

It can be noticed that the cell resistance (Rs) barely changes, indicating that the potential cycling has not significantly affected the system. Contrarily, by increasing the number of voltammetric cycles the value of Cdl also rose, which confirms that the active surface area increases upon cycling. Not only that, it reinforces the assumption of the surface reconstruction as well as agrees with the formation of a high surface area lamellar structure. Furthermore, the values of Rfar decreased as the number of cycles rose. One can be justified by the drop of R_2 values, once Rfar is a sum of R_1 and R_2, and R_1 values kept nearly constant. Such an effect is strongly associated with the great increase in the rate of intermediates formation/desorption at the reconstructed surface.

Lastly, to assess PSZNi2.5_5 stability, chronopotentiometric measurement was carried out at 10 $mA.cm^{-2}$ in nitrogen saturated 1 M KOH electrolyte. For that, the catalyst was immobilized onto a Ni foam instead of a glassy carbon substrate, because Ni foam is known for enhancing electrocatalytic activity [157]. As can be seen in Figure 4.47 (c), there are two stages of significant importance. The potential drop within the first 100 minutes and its constancy until 250 minutes. In the first case, the drop must likely happen due to the surface reconstruction phenomenon and thus, leads to improved catalytic performance. Thereafter, it remains a constant value of ca. 1.56 V vs. RHE confirming the promising stability of PSZNi2.5_5 during OER process.

5. CONCLUSION AND FUTURE PROSPECTS

The main emphasis of this thesis was the development of a TM-containing PDC possessing high conductivity and thermal and chemical stabilities to be evaluated as a substitute for noble-metal catalysts for the water-splitting process in alkaline media, as it is a promising alternative for clean hydrogen generation. In conclusion to this goal, the PSZNi2.5_5 sample demonstrated promising OER activity. The high reactivity of Durazane ® 1800 toward DMF in the presence of $NiCl_2$ to prepare a Ni:organosilicon polymer coordination complex was exploited. Via a single-step process at a temperature as low as 500 °C under flowing argon a nanocomposite made of fcc and hcp polymorphic nanoscale Ni particles immobilized in a high SSA PDC matrix was obtained.

FTIR and elemental analyses demonstrated that the precursor represents an organosilicon polymer in which Ni-catalyzed crosslinking linkage formation occurs via Si-O-Si (DMF's reduction by Si-H), Si-C-C-Si (hydrosilylation) and Si-N-Si (dehydrocoupling) unit formation; Ni^{2+} coordinating silylamino and/or siloxane ligands. N_2 adsorption-desorption isotherms highlighted the large specific surface area of the pyrolyzed compound and its high micropore content. XRD coupled with FEB-SEM and HRTEM observations revealed the formation of pure Nickel with a structure corresponding to both FCC Ni and Interstitial-atom free (IAF) HCP Ni; the former being surrounded by carbon layers and the latter being preferentially formed in low-size particles.

Electrochemical measurements revealed an outstanding OER activity with an overpotential as low as 360 mV at 10 $mA.cm^{-2}$ and a Tafel slope of 66 mv dec^{-1}, especially considering that the sample contains only Ni without doping with a low Ni mass loading (0.15 mg cm^{-2}). It is, therefore, strongly suggested herein that OER performance is ascribed to the large specific surface area of the sample, allowing easier access to the active sites and the potential induced surface reconstruction of the Ni particles. It occurs via i) the direct formation of a lamellar oxyhydroxide phase at the surface of hcp-Ni nanoparticles and ii) the removal of the carbon shell surrounding fcc-Ni particles to be redistributed within the Si-N-C-O(H) matrix increasing its conductivity (resistance decrease). Although the OER activity of the studied catalyst is not currently the highest reported in literature in an alkaline electrolyte, it is among the best performances reported with Ni active phases. It is imperative to highlight that this study did not aim to find the most efficient material for OER but leaves the door open to the

development of future very active catalysts synthesized using a simple method as well as cheap precursors.

It can also be very useful and enriching for the continuity of this research to perform DSC and GPC analyzes of the most promising materials for a more detailed investigation of the thermal behavior of final products and to understand the precursors behavior before the cure, respectively. There is still room for further studies on optimizing the OER properties and extending them toward HER by considering specific process parameters that can affect the structure of Ni, chemical composition of the ceramic matrix, and the specific surface area of the final compound. It can also be easily considered the use of other low-cost transition metals such as Fe or Mn, or a mixture of them, as they are known to be active catalysts - employing the PDC design strategy, allowing to modify drastically and improving the catalytic properties towards the targeted reactions. Considering the process's simple and flexible chemistry as well as the readily available and low-cost precursors, these polymer-derived high specific surface area Si-N-C-O(H) immobilized transition metal nanocatalysts are expected to have a significant impact on electrocatalytic processes for clean energy applications.

References:

[1] Z.W. Seh, J. Kibsgaard, C.F. Dickens, I. Chorkendorff, J.K. Nørskov, T.F. Jaramillo, Combining theory and experiment in electroccatalysis: insights into materials design, Science (80-.). 355 (2017). https://doi.org/10.1126/science.aad4998.

[2] World Health Organization, Climate change, (2022). https://www.who.int/health-topics/climate-change#tab=tab_1 (acessado 21 de agosto de 2022).

[3] Eurostat, Eurostat News Release, (2018).

[4] OECD, Governments need to honour their climate pledges as risks grow, (2018). http://www.oecd.org/newsroom/governments-need-to-honour-their-climate-pledges-as-risks-grow.htm (acessado 20 de agosto de 2022).

[5] IPCC, 48th session of the IPCC on climate change, 2018.

[6] OECD, OECD secretary general to call for stronger action on climate change., (2019). https://www.oecd.org/newsroom/oecd-secretary-general-to-call-for-stronger -action-on-climate-change-on-wednesday-3-july-2019-at-the-graduate-institute-geneva.htm (acessado 20 de agosto de 2022).

[7] UNFCC, The Paris Agreement. What is the Paris Agreement?, (2021). https://unfccc.int/process/the-paris-agreement/what-is-the-paris-agreement.

[8] S. Wang, A. Lu, C.J. Zhong, Hydrogen production from water electrolysis: role of catalysts, Nano Converg. 8 (2021). https://doi.org/10.1186/s40580-021-00254-x.

[9] F.M. Sapountzi, J.M. Gracia, C.J.K. Weststrate, H.O.A. Fredriksson, J.W.H. Niemantsverdriet, Electrocatalysts for the generation of hydrogen, oxygen and synthesis gas, Prog. Energy Combust. Sci. 58 (2017) 1–35. https://doi.org/10.1016/j.pecs.2016.09.001.

[10] A.K. Kumar, I. Abidat, C. Canaff, A. Habrioux, C. Morais, T. Napporn, B. Kokoh, Metal Loading Effect on The Activity of Co3O4/NRGO Nanocomposites as Oxygen Bifunctional Catalyst, ChemElectroChem. 5 (2018) 483–493. https://doi.org/10.1002/celc.201701168.

[11] A. Vazhayil, L. Vazhayal, J. Thomas, S.A. C, N. Thomas, A comprehensive review on the recent developments in transition metal-based electrocatalysts for oxygen evolution reaction, Appl. Surf. Sci. Adv. 10 (2017) 862–875. https://doi.org/10.1016/j.apsadv.2021.100184.

[12] R. Zhao, X. Liu, K. Deng, W. Tian, K. Ma, S. Tan, H. Yue, J. Ji, Trimetallic Mo- /Ni-/Fe-Based Hybrids Anchored on Hierarchical N - CNTs Arrays with Abundant Defects and Interfaces for Alkaline Water Splitting, Ind. Eng. Chem. Res. 60 (2021) 12559–12569. https://doi.org/10.1021/acs.iecr.1c01806.

[13] S. Li, E. Li, X. An, X. Hao, Z. Jiang, G. Guo, Transition metal-based catalysts for electrochemical water splitting at high current density: current status and perspectives, Nanoscale. 13 (2021) 12788–12817.

[14] K.O. Yoro, M.O. Daramola, CO2 emission sources, greenhouse gases, and the global warming effect, in: Adv. Carbon Capture, Elsevier Inc., 2020: p. 3–28.

https://doi.org/10.1016/b978-0-12-819657-1.00001-3.

[15] I. Gunderson, S. Goyette, A. Gago-Silva, L. Quiquerez, A. Lehmann, Climate and land-use change impacts on potential solar photovoltaic power generation in the Black Sea region, Environ. Sci. Policy. 46 (2015) 70–81. https://doi.org/10.1016/j.envsci.2014.04.013.

[16] F.Y. Fu, M. Alharthi, Z. Bhatti, L. Sun, F. Rasul, I. Hanif, W. Iqbal, The dynamic role of energy security, energy equity and environmental sustainability in the dilemma of emission reduction and economic growth, J. Environ. Manage. 280 (2021) 111828. https://doi.org/10.1016/j.jenvman.2020.111828.

[17] B.R. Sutherland, Burden of Energy Inefficiency, Joule. 3 (2019) 2279–2281. https://doi.org/10.1016/j.joule.2019.09.018.

[18] S.I. Zandalinas, F.B. Fritschi, R. Mittler, Global Warming, Climate Change, and Environmental Pollution: Recipe for a Multifactorial Stress Combination Disaster, Trends Plant Sci. 26 (2021) 588–599. https://doi.org/10.1016/j.tplants.2021.02.011.

[19] C. Bonneuil, P. Choquet, B. Franta, Early warnings and emerging accountability: Total's responses to global warming , 1971 – 2021, Glob. Environ. Chang. 71 (2021) 102386. https://doi.org/10.1016/j.gloenvcha.2021.102386.

[20] V. Masson-Delmotte, P. Zhai, A. Pirani, S.L. Connors, C. Péan, S. Berger, N. Caud, Y. Chen, L. Goldfarb, M.I. Gomis, M. Huang, K. Leitzell, E. Lonnoy, J.B.R. Matthews, T.K. Maycock, T. Waterfield, O. Yelekçi, R. Yu, B. Zhou, Climate Change 2021: The Physical Science Basis. Contribution of Working Group I to the Sixth Assessment Report of the Intergovernmental Panel on Climate Change., New York, 2021. https://doi.org/https://dx.doi.org/10.1017/9781009157896.

[21] C. Breyer, O. Koskinen, P. Blechinger, Profitable climate change mitigation: The case of greenhouse gas emission reduction benefits enabled by solar photovoltaic systems, Renew. Sustain. Energy Rev. 49 (2015) 610–628. https://doi.org/10.1016/j.rser.2015.04.061.

[22] B. Bayulken, D. Huisingh, P.M.J. Fisher, How are nature based solutions helping in the greening of cities in the context of crises such as climate change and pandemics? A comprehensive review, J. Clean. Prod. 288 (2021) 125569. https://doi.org/10.1016/j.jclepro.2020.125569.

[23] H. Fekete, T. Kuramochi, M. Roelfsema, M. den Elzen, N. Forsell, N. Höhne, L. Luna, F. Hans, S. Sterl, J. Olivier, H. van Soest, S. Frank, M. Gusti, A review of successful climate change mitigation policies in major emitting economies and the potential of global replication, Renew. Sustain. Energy Rev. 137 (2021). https://doi.org/10.1016/j.rser.2020.110602.

[24] D.P. Van Vuuren, E. Stehfest, D.E.H.J. Gernaat, M. Van Den Berg, D.L. Bijl, H.S. De Boer, V. Daioglou, J.C. Doelman, O.Y. Edelenbosch, M. Harmsen, A.F. Hof, M.A.E. Van Sluisveld, Alternative pathways to the 1.5 °c target reduce the need for negative emission technologies, Nat. Clim. Chang. 8 (2018) 391–397. https://doi.org/10.1038/s41558-018-0119-8.

[25] H. Ritchie, Our world in data. Global primary energy: How has the mix changed over centuries?, Publ. online OurWorldInData.org. (2019).

https://ourworldindata.org/energy-mix (acessado 15 de janeiro de 2022).

[26] F.M. Sapountzi, J.M. Gracia, C.J. (Kee. J. Weststrate, H.O.A. Fredriksson, J.W. (Hans. Niemantsverdriet, Electrocatalysts for the generation of hydrogen, oxygen and synthesis gas, Prog. Energy Combust. Sci. 58 (2017) 1–35. https://doi.org/10.1016/j.pecs.2016.09.001.

[27] J.D. Jenkins, M. Luke, S. Thernstrom, Getting to Zero Carbon Emissions in the Electric Power Sector, Joule. 2 (2018) 2498–2510. https://doi.org/10.1016/j.joule.2018.11.013.

[28] L. Zou, L. Wang, J. Li, Y. Lu, W. Gong, Y. Niu, Global surface solar radiation and photovoltaic power from Coupled Model Intercomparison Project Phase 5 climate models, J. Clean. Prod. 224 (2019) 304–324. https://doi.org/10.1016/j.jclepro.2019.03.268.

[29] J. Tao, S. Yu, Review on feasible recycling pathways and technologies of solar photovoltaic modules, Sol. Energy Mater. Sol. Cells. 141 (2015) 108–124. https://doi.org/10.1016/j.solmat.2015.05.005.

[30] R. Prăvălie, C. Patriche, G. Bandoc, Spatial assessment of solar energy potential at global scale. A geographical approach, J. Clean. Prod. 209 (2019) 692–721. https://doi.org/10.1016/j.jclepro.2018.10.239.

[31] P. Pal, V. Mukherjee, P. Kumar, M.E. Makhatha, Pre-feasibility analysis and performance assessment of solar photovoltaic (PV) modules for the application of renewable power generation, Mater. Today Proc. 39 (2020) 1813–1819. https://doi.org/10.1016/j.matpr.2020.10.557.

[32] P. Veers, L. Sethuraman, J. Keller, Wind-Power Generator Technology Research Aims to Meet Global-Wind Power Ambitions, Joule. 4 (2020) 1861–1863. https://doi.org/10.1016/j.joule.2020.08.019.

[33] Y. Zhang, D. Manaig, D.J. Freschi, J. Liu, Materials design and fundamental understanding of tellurium-based electrochemistry for rechargeable batteries, Energy Storage Mater. 40 (2021) 166–188. https://doi.org/10.1016/j.ensm.2021.05.011.

[34] J. Song, C. Wei, Z. Huang, C. Liu, L. Zeng, X. Wang, Z.J. Xu, A review on fundamentals for designing oxygen evolution electrocatalysts, Chem. Soc. Rev. 49 (2020) 2196. https://doi.org/10.1039/c9cs00607a.

[35] X. Zou, Y. Zhang, Noble metal-free hydrogen evolution catalysis for water splitting, Chem. Soc. Rev. (2015). https://doi.org/10.1039/C4CS00448E.

[36] D. Chodvadiya, N.N. Som, P.K. Jha, B. Chakraborty, Enhancement in the catalytic activity of two-dimensional α-CN by B, Si and P doping for hydrogen evolution and oxygen evolution reactions, Int. J. Hydrogen Energy. 46 (2021) 22478–22498. https://doi.org/10.1016/j.ijhydene.2021.04.080.

[37] S.Z. Baykara, Hydrogen: A brief overview on its sources, production and environmental impact, Int. J. Hydrogen Energy. 43 (2018) 10605–10614. https://doi.org/10.1016/j.ijhydene.2018.02.022.

[38] M. Hermesmann, T.E. Müller, Green, Turquoise, Blue, or Grey? Environmentally friendly Hydrogen Production in Transforming Energy Systems ☆, Prog. Energy Combust. Sci. 90 (2022) 100996. https://doi.org/10.1016/j.pecs.2022.100996.

[39] S.G. Nnabuife, J. Ugbeh-johnson, N.E. Okeke, C. Ogbonnaya, Present and Projected Developments in Hydrogen Production: A Technological Review, Carbon Capture Sci. Technol. (2022). https://doi.org/10.1016/j.ccst.2022.100042.

[40] X. Li, L. Zhao, J. Yu, X. Liu, X. Zhang, H. Liu, W. Zhou, Water Splitting: From Electrode to Green Energy System, Nano-Micro Lett. 12 (2020) 131. https://doi.org/10.1007/s40820-020-00469-3.

[41] M. Ji, J. Wang, Review and comparison of various hydrogen production methods based on costs and life cycle impact assessment indicators, Int. J. Hydrogen Energy. 46 (2021) 38612–38635. https://doi.org/10.1016/j.ijhydene.2021.09.142.

[42] S.G. Nnabuife, J. Ugbeh-johnson, S.G. Nnabuife, Present and Projected Developments in Hydrogen Production : A Technological Review, Carbon Capture Sci. Technol. (2022) 100042. https://doi.org/10.1016/j.ccst.2022.100042.

[43] W.T. Hong, M. Risch, K.A. Stoerzinger, A. Grimaud, J. Suntivich, Y. Shao-Horn, Toward the rational design of non-precious transition metal oxides for oxygen electrocatalysis, Energy Environ. Sci. 8 (2015) 1404–1427. https://doi.org/10.1039/C4EE03869J.

[44] K. Zeng, D. Zhang, Recent progress in alkaline water electrolysis for hydrogen production and applications, Prog. Energy Combust. Sci. 36 (2010) 307–326. https://doi.org/10.1016/j.pecs.2009.11.002.

[45] S. Anantharaj, K. Karthick, S.S. Sankar, K. Sangeetha, P.E. Karthik, S. Kundu, Precision and Correctness in the Evaluation of Electrocatalytic Water Splitting: Revisiting Activity Parameters with a Critical Assessment, Energy Environ. Sci. 11 (2018) 744–771. https://doi.org/10.1039/C7EE03457A.

[46] V. V. Kharton, Handbook of solid state electrochemistry. Fundamentals, materials and their applications, 2009.

[47] R.S. El-emam, H. Ozcan, Comprehensive review on the techno-economics of sustainable large-scale clean hydrogen production, J. Clean. Prod. 220 (2019) 593–609. https://doi.org/10.1016/j.jclepro.2019.01.309.

[48] S.S. Kumar, V. Himabindu, Hydrogen production by PEM water electrolysis – A review, Mater. Sci. Energy Technol. 2 (2019) 442–454. https://doi.org/10.1016/j.mset.2019.03.002.

[49] S. Anwar, F. Khan, Y. Zhang, A. Djire, Recent development in electrocatalysts for hydrogen production through water electrolysis, Int. J. Hydrogen Energy. 46 (2021) 32284–32317. https://doi.org/10.1016/j.ijhydene.2021.06.191.

[50] M. Carmo, D.L. Fritz, J. Mergel, D. Stolen, A comprehensive review on PEM water electrolysis, Int. J. Hydrogen Energy. 38 (2013) 4901–4934. https://doi.org/10.1016/j.ijhydene.2013.01.151.

[51] K. Chau, A. Djire, F. Khan, Review and analysis of the hydrogen production technologies from a safety perspective, Int. J. Hydrogen Energy. 47 (2022) 13990–14007. https://doi.org/10.1016/j.ijhydene.2022.02.127.

[52] J. Brauns, T. Turek, Alkaline Water Electrolysis Powered by Renewable Energy: A Review, Processes. 8 (2020) 248. https://doi.org/10.3390/pr8020248.

[53] J. Koponen, Review of water electrolysis technologies and design of renewable hydrogen production systems, 2015.

[54] K. Zeng, Improvements and Optimisation of Water Electrolysis for Hydrogen Production, The University of Western Australia, 2012.

[55] D. Jang, H. Cho, S. Kang, Numerical modeling and analysis of the effect of pressure on the performance of an alkaline water electrolysis system, Appl. Energy. 287 (2021) 116554. https://doi.org/10.1016/j.apenergy.2021.116554.

[56] S. Sebbahi, N. Nabil, A. Alaoui-belghiti, S. Laasri, S. Rachidi, A. Hajjaji, Assessment of the three most developed water electrolysis technologies: Alkaline Water Electrolysis, Proton Exchange Membrane and Solid-Oxide Electrolysis, Mater. Today Proc. (2022). https://doi.org/10.1016/j.matpr.2022.04.264.

[57] F. Allebrod, High Temperature and Pressure Alkaline Electrolysis, Technical University of Denmark, 2013.

[58] Y. Naimi, A. Antar, Hydrogen Generation by Water Electrolysis, in: Adv. Hydrog. Gener. Technol., 2018: p. 1–18. https://doi.org/10.5772/intechopen.76814.

[59] M. Yu, E. Budiyanto, H. Tüysüz, Principles of Water Electrolysis and Recent Progress in Cobalt-, Nickel-, and Iron-Based Oxides for the Oxygen Evolution Reaction, Angew. Chemie - Int. Ed. 61 (2022). https://doi.org/10.1002/anie.202103824.

[60] M. Wang, Z. Wang, Z. Gong, Z. Guo, The intensification technologies to water electrolysis for hydrogen production – A review, Renew. Sustain. Energy Rev. 29 (2014) 573–588. https://doi.org/10.1016/j.rser.2013.08.090.

[61] L. Lv, Z. Yang, K. Chen, C. Wang, Y. Xiong, Electrocatalysts: 2D Layered Double Hydroxides for Oxygen Evolution Reaction: From Fundamental Design to Application., Adv. Energy Mater. 17 (2019).

[62] Y.X. Chen, A. Lavacchi, H.A. Miller, M. Bevilacqua, J. Filippi, M. Innocenti, A. Marchionni, W. Oberhauser, L. Wang, F. Vizza, Nanotechnology makes biomass electrolysis more energy efficient than water electrolysis, Nat. Commun. 4036 (2014) 1–6. https://doi.org/10.1038/ncomms5036.

[63] C. Wei, S. Sun, D. Mandler, X. Wang, S.Z. Qiao, Z.J. Xu, Approaches for measuring the surface areas of metal oxide electrocatalysts for determining their intrinsic electrocatalytic activity, Chem. Soc. Rev. 48 (2019) 2518–2534. https://doi.org/10.1039/c8cs00848e.

[64] X. Liu, X. Lv, P. Wang, Q. Zhang, B. Huang, Z. Wang, Y. Liu, Z. Zheng, Y. Dai, Improving the HER activity of Ni3FeN to convert the superior OER electrocatalyst to an efficient bifunctional electrocatalyst for overall water splitting by doping with molybdenum, Electrochim. Acta. 333 (2020) 135488. https://doi.org/10.1016/j.electacta.2019.135488.

[65] R. Boppella, J. Tan, J. Yun, S. V Manorama, J. Moon, Anion-mediated transition metal electrocatalysts for efficient water electrolysis: Recent advances and future perspectives, Coord. Chem. Rev. 427 (2021) 213552. https://doi.org/10.1016/j.ccr.2020.213552.

[66] S. Zhang, X. Zhang, Y. Rui, R. Wang, X. Li, Recent advances in non-precious metal electrocatalysts for pH-universal hydrogen evolution reaction, Green Energy Environ. 6

(2021) 458–478. https://doi.org/10.1016/j.gee.2020.10.013.

[67] C. Hu, L. Zhang, J. Gong, Recent progress of mechanism comprehension and design of electrocatalysts for alkaline water splitting, Energy Environ. Sci. 12 (2019) 2620. https://doi.org/10.1039/C9EE01202H.

[68] M.A. Khan, H. Zhao, W. Zou, Z. Chen, W. Cao, J. Fang, J. Xu, L. Zhang, J. Zhang, Recent Progresses in Electrocatalysts for Water Electrolysis, Springer Singapore, 2018. https://doi.org/10.1007/s41918-018-0014-z.

[69] L. Han, S. Dong, E. Wang, Transition-Metal (Co, Ni, and Fe) -Based Electrocatalysts for the Water Oxidation Reaction, Adv. Mater. (2016) 1–26. https://doi.org/10.1002/adma.201602270.

[70] K. Zhu, F. Shi, X. Zhu, W. Yang, The roles of oxygen vacancies in electrocatalytic oxygen evolution reaction, Nano Energy. 73 (2020) 104761. https://doi.org/10.1016/j.nanoen.2020.104761.

[71] P. Rüetschi, P. Delahay, Influence of Electrode Material on Oxygen Overvoltage: A Theoretical Analysis, J. Chem. Phys. 23 (1955) 556–560. https://doi.org/10.1063/1.1742029.

[72] S. Sui, X. Wang, X. Zhou, Y. Su, S. Riffat, C.-J. Liu, A comprehensive review of Pt electrocatalysts for oxygen reduction reaction: nanostructure, activity, mechanism and carbon support in PEM fuel cells, J. Mater. Chem. A. 5 (2017) 1808–1825. https://doi.org/10.1039/C6TA08580F.

[73] J. Zhang, Z. Xia, L. Dai, Carbon-based electrocatalysts for advanced energy conversion and storage, (2015).

[74] E. Antolini, Iridium As Catalyst and Cocatalyst for Oxygen Evolution/Reduction in Acidic Polymer Electrolyte Membrane Electrolyzers and Fuel Cells, ACS Catal. 4 (2014) 1426–1440.

[75] T. Jiang, Development of Alkaline Electrolyzer Electrodes and Their Characterization in Overall Water Splitting, Université de Technologie Belfort-Montbéliard, 2020.

[76] H. Wan, X. Liu, H. Wang, R. Ma, T. Sasaki, Recent advances in developing high-performance nanostructured electrocatalysts based on 3d transition metal elements, Nanoscale Horizons. 4 (2019) 789–808. https://doi.org/10.1039/c8nh00461g.

[77] H. Park, A. Encinas, J.P. Scheifers, Y. Zhang, B.P.T. Fokwa, Boron-Dependency of Molybdenum Boride Electrocatalysts for the Hydrogen Evolution Reaction, Angew. Chemie Int. 56 (2017) 5575–5579. https://doi.org/10.1002/anie.201611756.

[78] J. Masa, I. Sinev, H. Mistry, E. Ventosa, M. De Mata, J. Arbiol, M. Muhler, B.R. Cuenya, W. Schuhmann, Ultrathin High Surface Area Nickel Boride (NixB) Nanosheets as Highly Efficient Electrocatalyst for Oxygen Evolution, Adv. Energy Mater. 7 (2017) 1700381. https://doi.org/10.1002/aenm.201700381.

[79] G. Qin, Q. Cui, A. Du, Q. Sun, Transition metal diborides: a new type of high-performance electrocatalysts for nitrogen reduction, ChemCatChem. 11 (2019) 2624. https://doi.org/10.1002/cctc.201900538.

[80] I. González-jiménez, A. Torres-pardo, S. Rano, C. Laberty-Robert, J.C. Hernández-

garrido, M. Lopez-haro, J. Calvino, A. Varela, C. Sanchez, M. Parras, Multicationic Sr4Mn3O10 mesostructures: molten salt synthesis, analytical electron microscopy study and reactivity, Mater. Horizons. 5 (2018) 480.

[81] S. Ananthaneni, Z. Smith, R.B. Rankin, Graphene Supported Tungsten Carbide as Catalyst for Electrochemical Reduction of CO2, Catalysts. 9 (2019) 604.

[82] J. Theerthagiri, S.J. Lee, A.P. Murthy, J. Madhavan, M.Y. Choi, Fundamental aspects and recent advances in transition metal nitrides as electrocatalysts for hydrogen evolution reaction: A review, Curr. Opin. Solid State Mater. Sci. 24 (2020) 100805. https://doi.org/10.1016/j.cossms.2020.100805.

[83] S. Yunqi, L. Jiaming, L. Guoming, X. Kui, Growth of porous single-crystalline molybdenum nitrides microcubes with enhanced electrocatalysis performance, Int. J. Hydrogen Energy. (2021). https://doi.org/10.1016/j.ijhydene.2021.04.041.

[84] J.F. Callejas, C.G. Read, C.W. Roske, N.S. Lewis, R.E. Schaak, Synthesis , Characterization, and Properties of Metal Phosphide Catalysts for the Hydrogen-Evolution Reaction, Chem. Mater. 28 (2016) 6017. https://doi.org/10.1021/acs.chemmater.6b02148.

[85] Y. Li, Z. Dong, L. Jiao, Multifunctional Transition Metal-Based Phosphides in Energy-Related Electrocatalysis, 1902104 (2019) 1–36. https://doi.org/10.1002/aenm.201902104.

[86] J. Béjar, L. Álvarez-Contreras, M. Guerra-Balcázar, J. Ledesma-García, L.G. Arriaga, N. Arjona, Synthesis of a small-size metal oxide mixture based on MoOx and NiO with oxygen vacancies as bifunctional electrocatalyst for oxygen reactions, Appl. Surf. Sci. 509 (2020) 144898. https://doi.org/10.1016/j.apsusc.2019.144898.

[87] X. Xiao, X. Li, J. Wang, G. Yan, Z. Wang, H. Guo, W. Peng, Three-dimensionally mesoporous dual (Co, Fe) metal oxide/CNTs composite as electrocatalysts for air cathodes in Li-O2 batteries, Ceram. Int. 44 (2018) 21942–21949. https://doi.org/10.1016/j.ceramint.2018.08.307.

[88] Q. Wen, Z. Yu, R. Riedel, The fate and role of in situ formed carbon in polymer-derived ceramics, Prog. Mater. Sci. 109 (2020) 100623. https://doi.org/10.1016/j.pmatsci.2019.100623.

[89] W. Verbeek, Production of shape articles of homogeneous mixture of silicon caribe and nitride, 1974.

[90] S. Yajima, J. Hayashi, M. Omori, Continuous silicon carbide fiber of high tensile strength, 1975.

[91] S. Yajima, M. Omori, J. Hayashi, K. Okamura, Simple synthesis of the continuous SiC fiber with high tensile strength, 1976.

[92] P. Colombo, G. Mera, R. Riedel, G.D. Sorarù, Polymer-derived ceramics: 40 Years of research and innovation in advanced ceramics, J. Am. Ceram. Soc. 93 (2010) 1805–1837. https://doi.org/10.1111/j.1551-2916.2010.03876.x.

[93] H.P. de Macedo, Ni-Containing Hybrid Ceramics Derived from Polysiloxanes for Production of CH 4 via Hydrogenation of CO2, Federal University of Rio Grande do Norte, 2018.

[94] E. Bernardo, L. Fiocco, G. Parcianello, E. Storti, P. Colombo, Advanced ceramics from preceramic polymers modified at the nano-scale: A review, Materials (Basel). 7 (2014) 1927–1956. https://doi.org/10.3390/ma7031927.

[95] C. Vakifahmetoglu, D. Zeydanli, P. Colombo, Porous polymer derived ceramics, Mater. Sci. Eng. R Reports. 106 (2016) 1–30. https://doi.org/10.1016/j.mser.2016.05.001.

[96] E. Ionescu, S. Bernard, R. Lucas, P. Kroll, S. Ushakov, A. Navrotsky, R. Riedel, Polymer-Derived Ultra-High Temperature Ceramics (UHTCs) and Related Materials, Adv. Eng. Mater. 1900269 (2019) 1–24. https://doi.org/10.1002/adem.201900269.

[97] A. Lale, Synthèse et caractérisation de nanocomposites à base de nitrure de silicium et de bore comme support catalytique mesoporeux pour applications énergétiques, (2017).

[98] P. Colombo, E. Bernardo, G. Parcianello, Multifunctional advanced ceramics from preceramic polymers and nano-sized active fillers, J. Eur. Ceram. Soc. 33 (2013) 453–469. https://doi.org/10.1016/j.jeurceramsoc.2012.10.006.

[99] A.R. Maddocks, D.J. Cassidy, A.S. Jones, A.T. Harris, Synthesis of nanoporous silicon carbide via the preceramic polymer route, Mater. Chem. Phys. 113 (2009) 861–867. https://doi.org/10.1016/j.matchemphys.2008.08.064.

[100] T. Schwob, R. Kempe, A Reusable Co Catalyst for the Selective Hydrogenation of Functionalized Nitroarenes and the Direct Synthesis of Imines and Benzimidazoles from Nitroarenes and Aldehydes, Angew. Chemie - Int. Ed. 55 (2016) 15175–15179. https://doi.org/10.1002/anie.201608321.

[101] M. Eckardt, M. Zaheer, R. Kempe, Nitrogen-doped mesoporous SiC materials with catalytically active cobalt nanoparticles for the efficient and selective hydrogenation of nitroarenes, Sci. Rep. 8 (2018) 1–6. https://doi.org/10.1038/s41598-018-20976-z.

[102] S. Tada, M.D. Mallmann, H. Takagi, J. Iihama, N. Asakuma, T. Asaka, Y. Daiko, S. Honda, R.K. Nishihora, R.A.F. Machado, S. Bernard, Y. Iwamoto, Low temperaturein situformation of cobalt in silicon nitride toward functional nitride nanocomposites, Chem. Commun. 57 (2021) 2057–2060. https://doi.org/10.1039/d0cc07366k.

[103] M. Zaheer, J. Hermannsdörfer, W.P. Kretschmer, G. Motz, R. Kempe, Robust heterogeneous nickel catalysts with tailored porosity for the selective hydrogenolysis of aryl ethers, ChemCatChem. 6 (2014) 91–95. https://doi.org/10.1002/cctc.201300763.

[104] D. Schumacher, M. Wilhelm, K. Rezwan, Porous SiOC monoliths with catalytic activity by in situ formation of Ni nanoparticles in solution-based freeze casting, J. Am. Ceram. Soc. 103 (2020) 2991–3001. https://doi.org/10.1111/jace.16988.

[105] M. Seifollahi Bazarjani, H.J. Kleebe, M.M. Müller, C. Fasel, M. Baghaie Yazdi, A. Gurlo, R. Riedel, Nanoporous silicon oxycarbonitride ceramics derived from polysilazanes in situ modified with nickel nanoparticles, Chem. Mater. 23 (2011) 4112–4123. https://doi.org/10.1021/cm200589n.

[106] M. Zaheer, C.D. Keenan, J. Hermannsdörfer, E. Roessler, G. Motz, J. Senker, R. Kempe, Robust microporous monoliths with integrated catalytically active metal sites investigated by hyperpolarized 129Xe NMR, Chem. Mater. 24 (2012) 3952–3963. https://doi.org/10.1021/cm302379b.

[107] M. Zaheer, T. Schmalz, G. Motz, R. Kempe, Polymer derived non-oxide ceramics

modified with late transition metals, Chem. Soc. Rev. 41 (2012) 5102–5116. https://doi.org/10.1039/c2cs15326b.

[108] C. Bäumler, R. Kempe, The Direct Synthesis of Imines, Benzimidazoles and Quinoxalines from Nitroarenes and Carbonyl Compounds by Selective Nitroarene Hydrogenation Employing a Reusable Iron Catalyst, Chem. - A Eur. J. 24 (2018) 8989–8993. https://doi.org/10.1002/chem.201801525.

[109] M. Zaheer, G. Motz, R. Kempe, The generation of palladium silicide nanoalloy particles in a SiCN matrix and their catalytic applications, J. Mater. Chem. 21 (2011) 18825–18831. https://doi.org/10.1039/c1jm13665h.

[110] M. Balestrat, A. Lale, A.V.A. Bezerra, V. Proust, E.W. Awin, R.A.F. Machado, P. Carles, R. Kumar, C. Gervais, S. Bernard, In-Situ Synthesis and Characterization of Nanocomposites in the Si-Ti-N and Si-Ti-C Systems, Molecules. 25 (2020) 5236. https://doi.org/10.3390/molecules25225236.

[111] A. S., P. Moni, P. Velayutham, S.A. Kumar, M. Kumar, Metal silicide nanosphere decorated carbon-rich polymer derived ceramics as bi-functional electro-catalyst towards oxygen and its application in anion exchange membrane fuel cell, ChemElectroChem. (2019). https://doi.org/10.1002/celc.201900475.

[112] Y. Feng, Z. Yu, R. Ralf, Enhanced hydrogen evolution reaction catalyzed by carbon-rich Mo4.8Si3C0.6/C/SiC nanocomposites via a PDC approach, J. Am. Ceram. Soc. 103 (2020) 1385–1395.

[113] Y. Feng, Z. Yu, J. Schuch, S. Tao, L. Wiehl, C. Fasel, W. Jaegermann, R. Riedel, Ternary nowotny phase Mo3+2xSi3C0.6 dispersed in a porous SiC/C matrix: A novel catalyst for Hydrogen Evolution Reaction, J. Am. Ceram. Soc. 103 (2020) 508–519. https://doi.org/10.1111/jace.16731.

[114] J. Rodríguez-Carvajal, Recent advances in magnetic structure determination by neutron powder diffraction, Phys. B Phys. Condens. Matter. 192 (1993) 55–69. https://doi.org/10.1016/0921-4526(93)90108-I.

[115] M. Wojdyr, Fityk: a general-purpose peak fitting program, J. Appl. Crystallogr. 43 (2010) 1126–1128. https://doi.org/10.1107/S0021889810030499.

[116] D. Fonblanc, D. Lopez-Ferber, M. Wynn, A. Lale, A. Soleilhavoup, A. Leriche, Y. Iwamoto, F. Rossignol, C. Gervais, S. Bernard, Crosslinking chemistry of poly(vinylmethyl-co-methyl)silazanes toward low-temperature formable preceramic polymers as precursors of functional aluminium-modified Si-C-N ceramics, Dalt. Trans. 47 (2018) 14580–14593. https://doi.org/10.1039/c8dt03076f.

[117] G. Parcianello, Advanced ceramics from preceramic polymers and fillers, (2012) 186.

[118] J. Wang, V. Schölch, O. Görke, G. Schuck, X. Wang, G. Shao, S. Schorr, M.F. Bekheet, A. Gurlo, Metal-containing ceramic nanocomposites synthesized from metal acetates and polysilazane, Open Ceram. 1 (2020). https://doi.org/10.1016/j.oceram.2020.100001.

[119] J. Wang, A. Gili, M. Grünbacher, S. Praetz, J.D. Epping, O. Görke, G. Schuck, S. Penner, C. Schlesiger, R. Schomäcker, A. Gurlo, M.F. Bekheet, Silicon oxycarbonitride ceramic containing nickel nanoparticles: from design to catalytic application, Mater. Adv. 2 (2021) 1715–1730. https://doi.org/10.1039/d0ma00917b.

[120] C. Zhou, L. Yang, H. Geng, Q. Zheng, H. Min, Z. Yu, H. Xia, Preparation of Si–C–N–Fe magnetic ceramic derived from iron-modified polysilazane, Ceram. Int. 38 (2012) 6815–6822. https://doi.org/10.1016/j.ceramint.2012.05.080.

[121] M. Manjunatha, G.S. Reddy, K.J. Mallikarjunaiah, R. Damle, K.P. Ramesh, Determination of Phase Composition of Cobalt Nanoparticles Using 59Co Internal Field Nuclear Magnetic Resonance, J. Supercond. Nov. Magn. 32 (2019) 3201–3209.

[122] Y.T. Jeon, J.Y. Moon, G.H. Lee, Comparison of the Magnetic Properties of Metastable Hexagonal Close-Packed Ni Nanoparticles with Those of the Stable Face-Centered Cubic Ni Nanoparticles, J. Phys. Chem. B. 110 (2006) 1187–1191.

[123] S. Kajiwara, S. Ohno, K. Honma, M. Uda, A new crystal structure of pure cobalt formed in ultrafine particles, Philos. Mag. Lett. 55 (1987) 215–219.

[124] L. Zhang, X. Chen, S. Jin, J. Guan, C.T. Williams, Z. Peng, C. Liang, Rapid microwaves synthesis of CoSix/CNTs as novel catalytic materials for hydrogenation of phthalic anhydride, J. Solid State Chem. 217 (2014) 105–112. https://doi.org/10.1016/j.jssc.2014.05.021.

[125] R. Arias-ugarte, H.K. Sharma, A.L.C. Morris, K.H. Pannell, Metal-Catalyzed Reduction of HCONR ′ 2 , R ′ = Me (DMF), Et (DEF), by Silanes to Produce R ′ 2 NMe and Disiloxanes: A Mechanism Unraveled, J. Am. Ceram. Soc. 134 (2012) 848–851.

[126] H. Wan, X. Liu, H. Wang, R. Ma, T. Sasaki, Recent advances in developing high-performance nanostructured electrocatalysts based on 3d transition metal elements, Nanoscale Horizons. 4 (2019) 789–808. https://doi.org/10.1039/c8nh00461g.

[127] E.W. Corcoran, L.G. Sneddon, Dehydrodimerization Reactions: A New Synthetic Route to Boron-Boron Linked Multicage Boranes and Carboranes, J. Am. Chem. Soc. 106 (1984) 7793–7800.

[128] T.J. Clark, K. Lee, I. Manners, Transition-Metal-Catalyzed Dehydrocoupling: A Convenient Route to Bonds between Main-Group Elements, Chem. - A Eur. J. 12 (2006) 8634–8648. https://doi.org/10.1002/chem.200600981.

[129] N. Yang, K. Lu, Effects of transition metals on the evolution of polymer-derived SiOC ceramics, Carbon N. Y. 171 (2021) 88–95. https://doi.org/10.1016/j.carbon.2020.08.072.

[130] N.R. Natter, Synthesis and characterization of novel carbon-based nanoporous materials for energy storage applications, 2020.

[131] A.S. Bolokang, M.J. Phasha, Novel synthesis of metastable HCP nickel by water quenching, Mater. Lett. 65 (2011) 59–60. https://doi.org/10.1016/j.matlet.2010.09.045.

[132] M. Wilhelm, C. Soltmann, D. Koch, G. Grathwohl, Ceramers — functional materials for adsorption techniques, J. Eur. Ceram. Soc. 25 (2005) 271–276. https://doi.org/10.1016/j.jeurceramsoc.2004.08.008.

[133] M. Thommes, K. Kaneko, A. V Neimark, J.P. Olivier, F. Rodriguez-reinoso, J. Rouquerol, K.S.W. Sing, Physisorption of gases, with special reference to the evaluation of surface area and pore size distribution (IUPAC Technical Report), 87 (2015) 1051–1069. https://doi.org/10.1515/pac-2014-1117.

[134] G. Mason, The Effect of Pore Space Connectivity on the Hysteresis of Capillary Condensation in Adsorption-Desorption Isotherms, J. Colloid Interface Sci. 88 (1982) 36–46.

[135] J.P. Dismukes, J.W. Johnson, J.S. Bradley, J.M. Millar, Chemical Synthesis of Microporous Nonoxide Ceramics from Polysilazanes, Chem. Mater. 9 (1997) 699–706.

[136] R.-T. Chiang, R.-K. Chiang, F.-S. Shieu, Emergence of interstitial-atom-free HCP nickel phase during the thermal decomposition of Ni3C nanoparticles, RSC Adv. 4 (2014) 19488–19494. https://doi.org/10.1039/c4ra01874e.

[137] M.A.I. Nishanta, Powder diffraction methods, Ohio State University, 2008.

[138] S.R. Vallence, Microwave Synthesis and Mechanistic Examination of the Transition Metal Carbides, University of Nottingham, 2008.

[139] R.A. Young, The Rietveld method, Oxford University Press, 1993.

[140] K.H. Jack, Results of further X-ray structural investigations of the iron-carbon and iron-nitrogen systems and of related interstitial alloys, Acta Crystallogr. 3 (1950) 392–394. https://doi.org/10.1107/S0365110X50001075.

[141] S. Nagakura, Study of metallic carbides by electron diffraction part I. Formation and decomposition of nickel carbide, J. Phys. Soc. Japan. 12 (1957) 482–494.

[142] J.G. Wright, J. Goddard, The lattice constants and magnetic anisotropy constants of electrodeposited single crystal films of hexagonal close-packed nickel, Philos. Maganize A J. Theor. Exp. Appl. Phys. 11 (1965) 485–493. https://doi.org/10.1080/14786436508224236.

[143] V. Rodríguez-González, E. Marceau, P. Beaunier, M. Che, C. Train, Stabilization of hexagonal close-packed metallic nickel for alumina-supported systems prepared from Ni (II) glycinate, J. Solid State Chem. 180 (2007) 22–30. https://doi.org/10.1016/j.jssc.2006.09.015.

[144] S. Illy, O. Tillement, F. Machizaud, J.M. Dubois, F. Massicot, Y. Fort, J. Ghanbaja, First direct evidence of size-dependent structural transition in nanosized nickel particles, Philos. Mag. A. 79 (1999) 1021–1031.

[145] Y. Chen, X. Yang, Y. Cao, Z. Gan, L. An, Quantitative study on structural evolutions and associated energetics in polysilazane-derived amorphous silicon carbonitride ceramics, Acta Mater. 72 (2014) 22–31. https://doi.org/10.1016/j.actamat.2014.03.049.

[146] J. Lipowitz, J.A. Rabe, L.K. Frevel, R.L. Miller, Characterization of nanoporosity in polymer-derived ceramic fibres by X-ray scattering techniques, J. Mater. Sci. 25 (1990) 2118–2124.

[147] P.E. Sánchez-Jiménez, J.A. Downs, R. Raj, Transient Viscous Flow During the Evolution of a Ceramic (Silicon Carbonitride) from a Polymer (Polysilazane) ´, J. Am. Ceram. Soc. 2570 (2010) 2567–2570. https://doi.org/10.1111/j.1551-2916.2010.03897.x.

[148] L. Trotochaud, S.L. Young, J.K. Ranney, S.W. Boettcher, Nickel−Iron Oxyhydroxide Oxygen-Evolution Electrocatalysts: The Role of Intentional and Incidental Iron Incorporation, J. Am. Chem. Soc. 136 (2014) 6744–6753.

[149] I. Spanos, J. Masa, A. Zeradjanin, R. Schlögl, The Effect of Iron Impurities on Transition Metal Catalysts for the Oxygen Evolution Reaction in Alkaline Environment : Activity Mediators or Active Sites ?, Catal. Letters. 151 (2021) 1843–1856. https://doi.org/10.1007/s10562-020-03478-4.

[150] L. Köhler, E. Abrishami, V. Roddatis, J. Geppert, M. Risch, Mechanistic parameters of electrocatalytic water oxidation on LiMn2O4 in comparison to natural photosynthesis, ChemSusChem. 10 (2017) 4479–4490. https://doi.org/10.1002/cssc.201701582.

[151] C. Wang, Y. Wang, H. Yang, Y. Zhang, H. Zhao, Q. Wang, Revealing the Role of Electrocatalyst Crystal Structure on Oxygen Evolution Reaction with Nickel as an Example, Small. 14 (2018) 1802895. https://doi.org/10.1002/smll.201802895.

[152] R.D. Armstrong, M. Henderson, Impedance plane display of a reaction with an adsorbed intermediate, J. Electroanal. Chem. Interfacial Electrochem. 39 (1972) 81–90.

[153] J. Ruhl, L.M. Riegger, M. Ghidiu, W.G. Zeier, Impact of Solvent Treatment of the Superionic Argyrodite Li6PS5Cl on Solid-State Battery Performance, Adv. Energy Sustain. Res. 2 (2021) 200077–200086. https://doi.org/10.1002/aesr.202000077.

[154] R.L. Doyle, M.E.G. Lyons, An electrochemical impedance study of the oxygen evolution reaction at hydrous iron oxide in base, Phys. Chem. Chem. Phys. 15 (2013) 5224–5237. https://doi.org/10.1039/c3cp43464h.

[155] V.A. Alves, L.A. Silva, J.F.C. Boodts, Surface characterisation of IrO2/TiO2/CeO2 oxide electrodes and Faradaic impedance investigation of the oxygen evolution reaction from alkaline solution, Electrochim. Acta. 44 (1998) 1525–1534.

[156] L. Negahdar, F. Zeng, S. Palkovits, C. Broicher, R. Palkovits, Mechanistic aspects of the electrocatalytic oxygen evolution reaction over Ni-Co oxides, ChemElectroChem. 6 (2019) 5588–5595. https://doi.org/10.1002/celc.201901265.

[157] J.N. Hausmann, R. Beltrán-suito, S. Mebs, V. Hlukhyy, T.F. Fässler, H. Dau, M. Driess, P.W. Menezes, Evolving Highly Active Oxidic Iron (III) Phase from Corrosion of Intermetallic Iron Silicide to Master Efficient Electrocatalytic Water Oxidation and Selective Oxygenation of 5-Hydroxymethylfurfural, Adv. Mater. 33 (2021) 2008823. https://doi.org/10.1002/adma.202008823.